Volume 5 Issue 2

MERSIN PHOTOGRAMMETRY JOURNAL

Prof. Dr. İbrahim YILMAZ
Afyon Kocatepe University Engineering Faculty,
Turkey

Prof. Dr. Ömer MUTLUOĞLU
Konya Technical University
Faculty of Engineering and Natural Sciences,
Turkey

Assist. Prof. Dr. Sefa BİLGİLİOĞLU
Aksaray University, Engineering Faculty,
Turkey

Dr. Surendra Pal Singh,
Ethiopian Government University
Ethiopia

Dr. Dereje Sufa,
Wollega University
Ethiopia

The MERSİN PHOTOGRAMMETRY JOURNAL (MEPHOJ)

THE MERSİN PHOTOGRAMMETRY JOURNAL (MEPHOJ) publishes original and innovative contributions in photogrammetric applications ranging from the integration of instruments, methodologies, and technologies and their respective uses in the environmental sciences, engineering, and other natural sciences. Mersin Photogrammerty Journal is a branch of science that widely applied in many scientific disciplines. MEPHOJ aims to cover the entirety of Photogrammetry and Photogrammetric aplications about Geosciences, including their application domains. MEPHOJ strives to encourage scientists to publish experimental, theoretical, and computational results as detailed as possible so that results can be easily reproduced.

MEPHOJ is a double peer-reviewed (blind) OPEN ACCESS JOURNAL that publishes professional level research articles and subject reviews exclusively in English. It allows authors to submit articles online and track his or her progress via its web interface. All manuscripts will undergo a refereeing process; acceptance for publication is based on at least two positive reviews. The journal publishes research and review papers, professional communication, and technical notes. MEPHOJ does not charge for any article submissions or for processing.

CORRESPONDENCE ADDRESS
Journal Contact: myakar@mersin.edu.tr

CONTENTS

Volume 5 - Issue 2

RESEARCH ARTICLES

Mersin Photogrammetry Journal
https://dergipark.org.tr/en/pub/mephoj
e-ISSN 2687-654X

Detection of COVID-19 infection from CT images using the medical photogrammetry technique

Hatice Çatal Reis [*1], **Veysel Türk** [2], **Serhat Kaya** [3]

[1]*Gümüşhane University, Department of Geomatics Engineering, Türkiye*
[2]*Harran University, Department of Computer Engineering, Türkiye*
[3]*Dicle University, Department of Mining Engineering, Türkiye*

Keywords
SARS-CoV-2
Chest CT-scan images
Medical Photogrammetry
Machine Learning
Medical Image Processing

Research Article
DOI: 10.53093/mephoj.1301980

Received:24.05.2023
Revised: 18.06.2023
Accepted:27.06.2023
Published:17.10.2023

Abstract

Medical data such as computed tomography (CT), magnetic resonance imaging (MRI), and Ultrasound images are used in medical photogrammetry. CT images have been used frequently in recent years for the diagnosis of COVID-19 disease, which has contagious and fatal symptoms. CT is an effective method for early detection of lung anomalies due to COVID-19 infection. Machine learning (ML) techniques can be used to detect and diagnose medical diseases. In particular, classification methods are applied for disease diagnosis and diagnosis. This study proposes traditional machine learning algorithms Random Forest, Logistic Regression, K-Nearest Neighbor and Naive Bayes, and an ensemble learning model to detect COVID-19 anomalies using CT images. According to the experimental findings, the proposed ensemble learning model produced an accuracy of 96.71%. This study can help identify the fastest and most accurate algorithm that predicts CT images with Covid-19 during the epidemic process. In addition, machine learning-based approaches can support healthcare professionals and radiologists in the diagnostic phase.

1. Introduction

COVID-19 has become the disease with the highest number of cases and deaths in the world in recent years [1]. COVID-19 is a highly contagious virus. The virus has undergone multiple mutations (Alpha, Beta, Delta, and Omicron) during its active periods, and the transmission rate has increased as it mutated [2]. Although not sure, the Omicron variant is transmitted 2/3 times faster than the Delta variant [2]. The COVID-19 pandemic has devastated social life and many areas of states, especially health, education, and the economy [3]. As of March 21, 2022, it has been determined that the number of infected people has reached 400 million, and there have been more than 6 million deaths [1]. By March 27, 2020, approximately sixty million educators and nearly two billion students in more than 180 countries were adversely affected by school closures [3]. With the closure of schools, distance education applications have become widespread; because of this, teachers and students had to adapt to the new teaching methodology [4].

Problems such as technological infrastructure inadequacies and adaptation problems of teachers and students in this process caused a decrease in the quality of education, and the increase in inequalities at the point of access to technology created inequality of opportunity in education [4, 5]. Such factors have caused significant damage to the education system. Due to the COVID-19 pandemic worldwide, approximately 1.6 billion students have received distance education [6]. The COVID-19 pandemic has also created adverse effects on economic balances. Situations such as job losses, cessation of trade/tourism, and closure of businesses during the pandemic have adversely affected their economic activities [7]. During the epidemic, 255 million people lost their jobs [8]. The COVID-19 virus affects humans' respiratory, renal, neuronal, gastrointestinal, and cardiovascular systems and causes severe pathologies in many organs, such as the heart and kidney, especially the

* **Corresponding Author**

*(hatice.catal@yahoo.com.tr) ORCID ID 0000-0003-2696-2446
(veyselturk484@gmail.com) ORCID ID 0000-0003-1250-0590
(kserhat086@gmail.com) ORCID ID 0000-0002-8824-2340

Cite this article

Çatal Reis, H., Türk, V., & Kaya, S. (2023). Detection of COVID-19 infection from CT images using the medical photogrammetry technique. Mersin Photogrammetry Journal, 5(2), 42-54

lungs [9, 10]. The infection can cause serious complications in the elderly, in people with weakened immune systems, and in patients with chronic health problems such as cardiovascular diseases such as heart valve diseases/peripheral vascular diseases, diabetes, lung cancer, liver diseases, and hypertension. Therefore, it indicates that it is pathogenic [11]. Type I (hypoxemia, lack of oxygen in the blood) and type II (hypercapnia, increased carbon dioxide in the blood) respiratory failure, pulmonary edema, inflammation in the alveoli/bronchi, fibrosis (hardening of the lung tissue), thickening of the capillary wall in patients with COVID-19 infection Capillary occlusion, pericarditis (heart membrane inflammation), myocarditis (heart muscle inflammation), intravascular coagulation, heart attack, symptoms can be seen [12, 13, 14]. Puntmann et al. [15], conducted the study with patients with COVID-19 infection, myocarditis was observed in 60 of 100 patients, and cardiac involvement was observed in 78 patients. According to Douaud et al. [16], brain tissue damage, gray matter reduction, and brain volume reduction were detected in patients with COVID-19 infection. SARS-CoV-2 in the first stage of the disease stage; muscle pain, fatigue, and fever are common symptoms in the second stage; Ground-glass opacities (GGO) are seen in the majority of computed tomography (CT) images in the third stage; hypercoagulation in patients undergoing treatment, in the fourth and final stage; A picture of multi-organ failure occurs as a result of an excessive response of the immune system [17]. IgM-IgG antibody tests, reverse transcription polymerase chain reaction to diagnose and detect COVID-19 patients. (RT-PCR) test kits have been widely used. In addition, CT, and chest X-ray (CXR) techniques, which are among the medical photogrammetric techniques, are also among the essential methods used in the disease diagnosis process [18]. In some cases, IgM-IgG antibody tests and RT-PCR can give incorrect or inadequate information [19, 20]. Chest CT/CXR shows abnormalities in the lung [21, 22]. Therefore, a CT/CXR scan can play a crucial role in the early diagnosis of COVID-19 infection [23]. Chest CT has shown to be a useful complement to test kits, and it has been presented to have better accuracy in diagnosing COVID-19 [24-28].

Among the medical imaging techniques, CT and CXR are frequently used in disease diagnosis. Among the advantages and disadvantages of the CT imaging technique compared to the CXR imaging technique; (i) CT shows higher accuracy in diagnostic processes [29]. (ii) It is the gold standard in diagnosing pneumonia, especially in adult patients. (iii) CT imaging technique is more damaging than CXR because of the radiation it emits [29]. Moreover, (iv) the high cost of the devices is one of the obstacles to their widespread use in hospitals [29]. Among the advantages and disadvantages of the CXR imaging technique compared to the CT imaging technique; (i) CXR is non-invasive, and its radiation rate is lower than CT. (ii) It is widely used in emergency departments because of its cheapness [30]. (iii) CXR analysis process is more complex than CT [31]. (iv) It is sensitive to noisy areas. (v) It performs poorly detecting anomalies in relatively small areas [31, 32]. Here, medical images obtained with the CT imaging technique contain more detail than CXR; medical images obtained from the CT imaging technique were used in anomaly detection in this study due to factors such as its success in detecting anomalies.

The application of machine learning models is promising to increase the diagnostic accuracy in the disease detection process from radiological images [33]. ML methods include COVID-19, ex-ebola, cholera, H1N1 influenza, zika, oyster norovirus, etc., applied in pandemics [34-36]. Chen [37] used the Support Vector Machine (SVM) algorithm with 10-fold cross-validation (cv) approach for the detection of COVID-19 from 296 (148 COVID-19, 148 Non-COVID-19) chest CT images. In addition, the author used Histogram Equalization (HE) and Gray-Level Co-Occurrence Matrix (GLCM) techniques to increase the efficiency of the proposed method. In addition, for the detailed performance analysis of the proposed method with the SVM algorithm, an experimental comparison was made with the K-Nearest Neighbors (KNN) and Naive Bayes (NB) algorithms under the same conditions. As a result, while the HE-GLCM-SVM hybrid method produced 75.69% accuracy in the COVID-19 detection study, the HE-GLCM-KNN and HE-GLCM-NB methods produced 69.63% and 66.46% accuracy, respectively. However, the limitation of the study was that testing was carried out with limited samples. The methods proposed here can be tested with a large-scale dataset to validate their findings in the study. In addition, the data set used in the study is lossy data. For the disease detection process to be carried out with maximum efficiency, it is necessary to perform the classification process with raw data with a dicom extension. According to Hasoon et al. [38], KNN and SVM algorithms were used to detect COVID-19 from chest X-ray images. In the study using 5000 medical images, the proposed models were tested with the 5-fold CV approach. In the pre-processing steps in the study; image thresholding, image noise removal, morphological operation, and segmentation application; Region of Interest (ROI), Haralick texture features, Histogram of Gradient (HOG), Local binary pattern (LBP) methods were applied in feature extraction. In the proposed study, LBP-KNN was the most successful method, with an average accuracy of 98.66%. According to the results (i), the proposed method for classifying and early detecting COVID-19 disease presented successful data. (ii) CXR imaging technique is a successful method for detecting COVID-19 disease. The limitation of the study is that the proposed methods were tested with a relatively small dataset. A detailed analysis should be performed with a large-scale dataset to verify the model's performance. Barstugan et al. [39] used the SVM algorithm for the early-stage detection of COVID-19 disease, and the dataset used consists of 150 chest CT images. In classification, testing was carried out with the 2, 5, and 10-fold CV approach. The authors used the discrete wavelet transform (DWT), local directional Pattern (LDP), Gray Level Co-occurrence Matrix (GLCM), Gray-Level Size Zone Matrix (GLSZM), Gray Level Run Length Matrix (GRLLM) methods to improve the performance of classification. Extraction was performed. In the study performed with GLSZM feature extraction and SVM algorithm with 5-fold CV, an accuracy value of 98.71%

was obtained. The proposed method in this study was trained with a small-scale dataset, and performance analysis was performed. The number of test data used to validate the model may need to be increased. Accordingly, a different and large-scale dataset should be used for detailed performance analysis of the proposed method. Yang et al. [40] had 180 (90 COVID-19 patients, 90 other types of pneumonia patients) chest CT images used the SVM algorithm to detect COVID-19. In the study, feature extraction was performed with A Gray Level Co-occurrence Matrix (GLCM), The Gray Run Length Matrix (GRLLM), The Neighborhood Gray Level Difference Matrix (NGLDM), The Gray Level Zone Length Matrix (GLZLM), and Histogram methods. The obtained features were classified using the SVM algorithm. In the application performed with GLCM-SVM, an accuracy value of 85.95% was obtained. Among the limitations of this study is the use of a small data set in the training and testing process of machine learning algorithms. In addition, machine learning algorithms were applied within the scope of the study in the disease diagnosis process, as well as convolution neural network-based deep learning architectures, which have been able to produce successful results in the field of image processing in recent years, could also be used in the disease diagnosis process. Although there is previous research on the COVID-19 disease detection process, more comprehensive analyzes are needed to test the success of machine learning algorithms in the disease detection process. In this study, we aimed to detect COVID-19 patients based on machine learning automatically. These models are Random Forest (RF), Logistic Regression (LR), k-Nearest Neighbors (KNN), Naive Bayes (NB), and Ensemble learning (EL) models. In the study, the features obtained by the deep learning model were used for the input data of machine learning algorithms. Deep learning is a machine learning method that consists of multi-layered neural networks. Deep learning can automatically discover complex patterns in data and essential features in representative data. Experimental stage;

(i) Deep features were extracted from the COVID-CT dataset with the DenseNet201 model previously trained with the ImageNet dataset.

(ii) feature vector obtained from deep learning algorithm was used as input data of RF, DT, KNN, and Gaussian NB machine learning algorithms. The classification performance of machine learning algorithms is directly proportional to the selection of hyper-parameters.

In this study, the Randomized Search CV algorithm is used in the process of determining the most suitable hyper-parameters for machine learning algorithms. (iii) Principal Component Analysis (PCA) method has been used to reduce the computational cost of the algorithms, eliminate noise and unnecessary information, and reduce the data size. The PCA method was applied to the feature vector obtained from the deep learning algorithm in the experimental process. PCA is a statistical method used to determine the relationships among the variables in a multivariate dataset and to determine the basic structures of the variables. PCA calculates the correlation of variables in the data set and determines the principal components using eigenvalue analysis. Eigenvalues and eigenvectors are obtained from the correlation matrix. When the eigenvalues are ordered from largest to smallest, the principal components with the largest eigenvalues are selected. These principal components represent the most variable and essential features of the data. PCA compresses or reduces the size of data through selected principal components. During this process, essential properties of the data are preserved. Thus, the data set is expressed with fewer variables. (iv) Finally, another method applied within the scope of the study to increase the success of machine learning algorithms in the diagnosis process of COVID-19 patients is ensemble learning. The voting classifier classification method is used in the Ensemble learning method. How can we predict cost-effectively COVID-19 patients, and how can we choose the best algorithm? The accuracy of the method is a critical element in evaluating the classification performance. There are many possibilities to explore in medical imaging [41], and each discipline offers approaches with its workspace. The important thing is to present effective scientific development and study. Unlike the medical literature, we presented a machine learning-based diagnostic approach. Radiologists and clinic physicians must be the pioneer in the Pandemic in medical imaging and interpretation [42]; however, different experts can be required to contribute to the system and the process. In this challenging process, Machine learning-based approaches can offer a secondary perspective.

2. Material and Method

Machine learning is considered a branch of artificial intelligence. Machine-learning algorithms are proven as a valuable part of computer-aided diagnosis and decision [43]. Machine learning algorithms and ensemble learning methods were used to predict non-COVID-19/COVID-19 from Chest-CT data.

The study has two main steps in the classification process: training and testing. The suggested workflow diagram is given in Figure 1. The algorithms used for the study are Random Forest, Logistic Regression, KNN, and Naive Bayes, respectively. The Voting Classifier algorithm was used in the Ensemble learning application.

2.1. Dataset

This section describes how the COVID-CT dataset is obtained and built (Table 1). We collected 757 CT images from https://github.com/UCSD-AI4H/COVID-CT [44]. GitHub is a public platform. These CT images have different sizes (e.g., 525x442, 450x319, 485x345 etc.) and different standards. All Chest-CT images were resized due to different scanning characteristics and image size differences. Table 1 represents the ML methods used and statistics of the dataset for COVID-19 prediction. Some examples of the dataset used in the study are given in Figure 2.

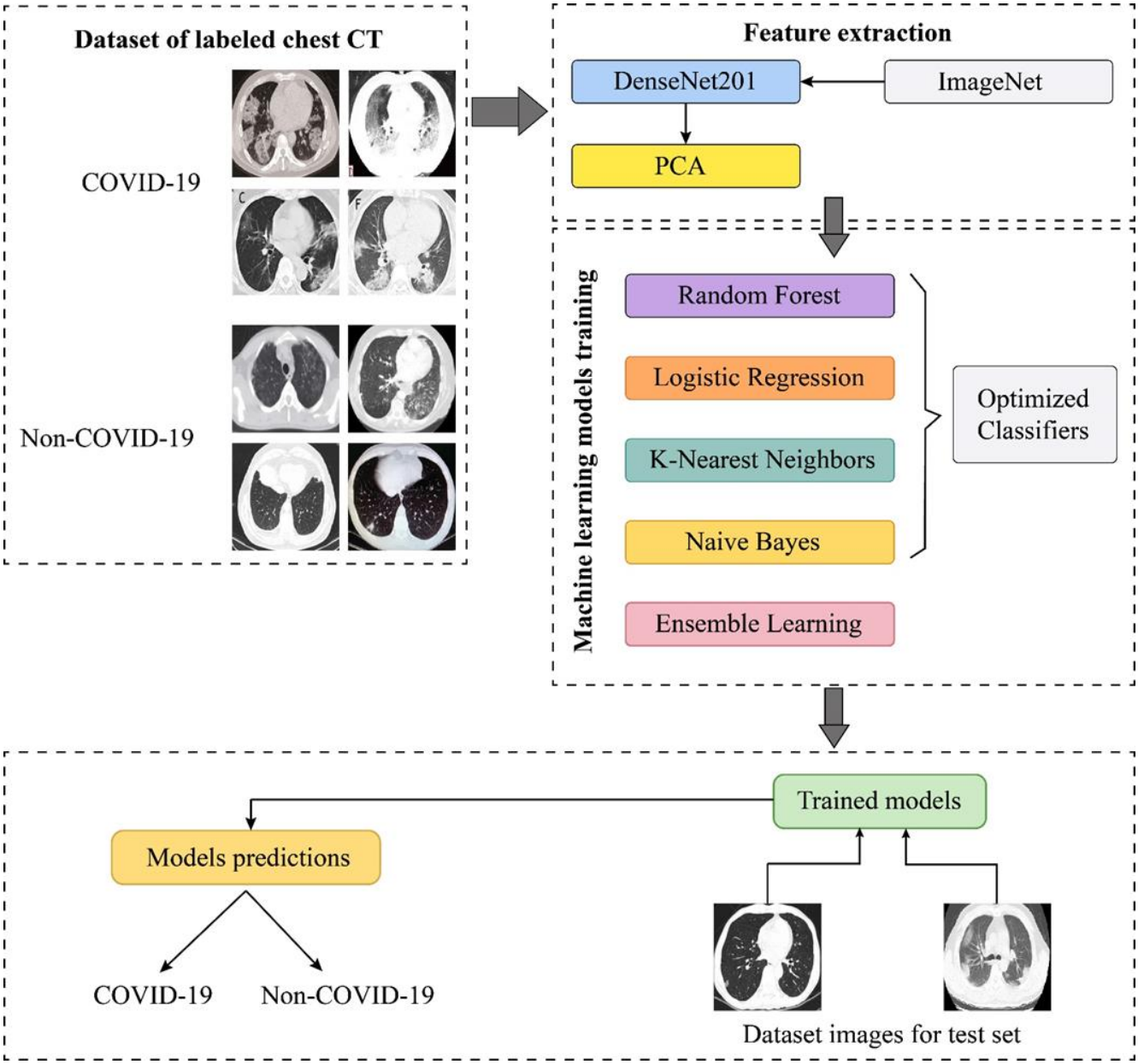

Figure 1. Flowchart of the study.

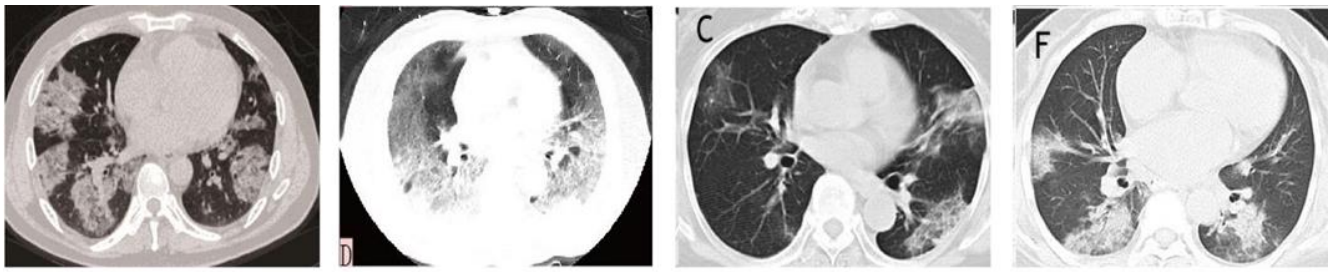

(a) COVID-19 infected patients

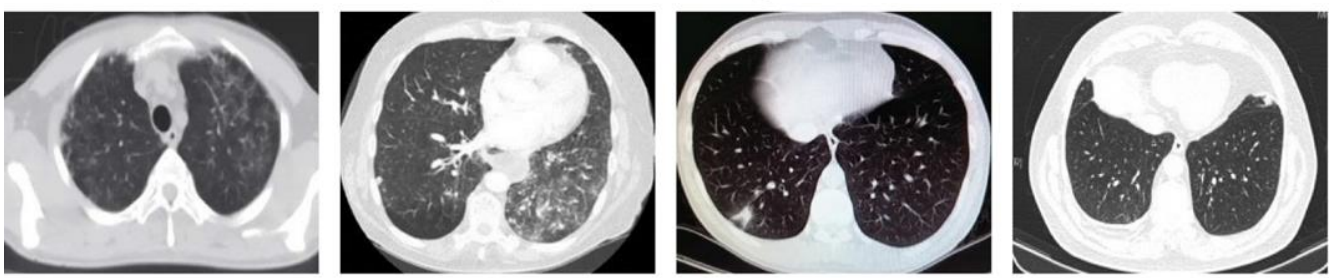

(b) Non-COVID-19 infected patients

Figure 2. Samples of CT images.

Table 1. Statistics of the dataset.

Medical imaging technique	Label	Category	Number of images	Number of training	Number for testing
CT	0	Non-COVID-19	397	317	80
	1	COVID-19	360	288	72

2.2. Implementation details of machine learning algorithms and pre-processing

This research study presents a methodology for classifying COVID-19 chest CT and normal chest CT images using machine learning architectures. We implement our models using the Python programming language and scikit-learn machine learning library. The study was done on a laptop with an Intel i5 processor, 6 GB of RAM, and a GTX 940MX NVidia GPU with 2GB of VRAM. In this study, feature extraction from the COVID-CT dataset was performed with the pre-trained DenseNet201 [45] deep learning model. Here are the preprocessing steps applied: (i) All images are resized from 224x224 pixels. The interpolation (INTER_CUBIC) technique was used in the resizing process. (ii) In the second step, min-max normalization was applied to the matrix obtained in the first step. Min-max normalization compresses the values in the dataset into a unit range. Thus, different variables/features share the same scale. This allows the model to learn the relevant features in a balanced way. (iii) Labels are assigned for data entries in the final stage. Accordingly, the "0" label for Non-COVID-19 images and the "1" label for COVID-19 images are defined.

Finally, feature vectors obtained from the deep learning model are used as input data for optimized machine learning algorithms. In addition, the PCA method has been applied to reduce the feature vector size obtained in the last step. In the experimental process, before and after the application of the PCA method, it was analyzed comparatively. In the application made with the PCA method, 200 features were used. Finally, within the scope of the study, the EL method was applied for a collective learning requirement with RF, DT, KNN, and Gaussian NB algorithms used in the diagnosis process of COVID-19 patients. Before and after applying the PCA method in the application process of the EL method, it was analyzed comparatively. The results are in the Results section. The trans-test approach was used in the studies performed with a machine learning algorithm and EL. Accordingly, the CT dataset consisting of Non-COVID-19/COVID-19 images is divided into 80% training and 20% test dataset.

The training process of machine learning algorithms was carried out with the training dataset. After the training process was completed, the performance of the models was performed with the test dataset. Accuracy, precision, recall, F1-score, MSE, RMSE, and confusion metrics were used to evaluate the experimental results.

2.3. Machine learning algorithm

In this section, the theoretical framework of traditional machine learning algorithms used for the detection of patients with COVID-19 infection is given. In this study, the Randomized Search CV algorithm in the sklearn-model_selection module was used to determine the hyperparameters of machine learning algorithms used to detect COVID-19 patients. The hyperparameters used in the algorithms are given in Table 2.

Table 2. Random Forest, Logistic Regression, K-Nearest Neighbors and Naive Bayes hyperparameters.

ML algorithms	Hyperparameters	Defined Parameters
Random Forest	bootstrap	False
	max_features	"auto"
	n_estimator (number of trees)	50
	min_samples_split	18
	min_samples_leaf	3
	max_depth	182
	criterion	"gini"
	random_state	0
Logistic Regression	C	1
	penalty	"l2"
	max_iter	79
	solver	"saga"
	multi_class	"auto"
K-Nearest Neighbors	n_neighbors	13
	weights	"uniform"
	algorithm	"brute"
	leaf_size	148
	p	2
	metric	"euclidean"
Naive Bayes	priors	None
	var_smoothing	1e-11

2.3.1. Random Forest

RF is a supervised machine learning method with decision networks based on the classification algorithm [46, 47], and it is often preferred in image classification [48]. The algorithm is trained by averaging the obtained samples according to the set of Decision Trees. It combines multiple classifiers to solve a complex problem and improves the model's performance [49]. A dataset contains large-size CT images, and the dataset is divided into subsets and sent to each decision tree. The Random Forest algorithm is noise-resistant and has better performance [50].

2.3.2. Logistic Regression

The logistic regression algorithm explains the connection between the two-dimensional response variable. The most significant feature of logistic regression is that variables do not require normal distribution [51]. Logistic Regression is divided into three types as Binomial, Multinomial, and Ordinal. We used binomial logistic regression, which has two possible dependent variables, such as COVID-19 or non-COVID-19.

2.3.3. K-Nearest Neighbors

The K-Nearest Neighbors is one of the traditional supervised machine learning algorithms. KNN is a non-parametric algorithm that estimates the data into categories and to which class the newest data will be included [52, 53]. Uses all of the data in the KNN dataset. The success of KNN depends on the Euclidean distance metric used to recognize neighbors close to the test data of the data to be classified [54]. Euclidean distance sends the newly added data to the nearest class with the help of Euclidean distance. In the algorithm, the number k has no optimal value. The trial-and-error method can determine the k metric by experimental processes.

2.3.4. Naive Bayes

Naive Bayes is the oldest machine learning method [43]. This method does not include the same iterative training process as many other machine learning methods. The Bernoulli classifier works the independent Booleans variables, and it is a fast and easy ML algorithm to predict a class of data. The Bernoulli Naive Bayes classifier assumes that features take only two values (COVID-19 or non-COVID-19).

2.3.5. Ensemble Learning

Ensemble learning is a machine learning algorithm. It strategically combines multiple heterogeneous/homogeneous classifiers to create a high-performance model in classification/regression applications [55]. Many studies show that the ensemble learning method is widely used in different problems [55]. In this study, the Voting Classifier classifier was used. In this research, the Voting Classifier function in the ensemble module of the Scikit-learn library was used to classify the COVID-19 disease proposed by the voting ensemble learning method. Other hyperparameters include the estimators ('RF', rf), ('GNB', gnb), ('LR', lr), ('KNN', knn)]), voting=(hard)).

2.4. Quantitative Analysis

Receiver operating characteristics (ROC) curves, F_1-score, Precision, Recall, Accuracy, Mean Square Error (MSE), and Root Mean Square Error (RMSE) metrics were used to perform quantitative analysis in the classification performed with machine learning algorithms. In this section, mathematical expressions of evaluation metrics are given. The Confusion Matrix (CM) is summarized in Table 3.

Table 3. Confusion matrix

	Predicted Positive	Predicted Negative
Actual Positive	True Positive (TP)	False Negative (FN)
Actual Negative	False Positive (FP)	True Negative (TN)

$$\text{Accuracy} = \frac{\text{TP} + \text{TN}}{\text{TP} + \text{TN} + \text{FP} + \text{FN}} \quad (1)$$

$$\text{Recall} = \frac{\text{TP}}{\text{TP} + \text{FN}} \quad (2)$$

$$\text{Precision} = \frac{\text{TP}}{\text{TP} + \text{FP}} \quad (3)$$

$$\text{F}_1 - \text{Score} = \frac{2 * (\text{Recall} * \text{Precision})}{(\text{Recall} + \text{Precision})} \quad (4)$$

$$\text{MSE} = \frac{\sum_{i=1}^{n} (y_i - \hat{y}_i)^2}{n} \quad (5)$$

$$\text{RMSE} = \sqrt{\text{MSE}} = \sqrt{\frac{\sum_{i=1}^{n} (y_i - \hat{y}_i)^2}{n}} \quad (6)$$

In Equation (5-6); "n" total number of data, "y" actual values "ŷ" predictive values.

3. Results

In our experiment, we used different machine-learning methods for evaluation. This study evaluated the applicability of four machine learning models (Random Forest, Logistic Regression, K-Nearest Neighbors, and Naive Bayes) and an ensemble learning model for diagnosing COVID-19 patients. According to the accuracy metric value before the PCA application, Random Forest, K-Nearest Neighbors algorithms, and the proposed ensemble learning method produced the most successful results with a value of 96.71%. On the other hand, in the COVID-19 disease diagnosis process, Naive Bayes has the lowest success rate of 94.74% according to the accuracy metric in this study (Table 4). Our other findings, according to the F1-score metric value, the Random Forest produced the most successful results with a rate of 96.60%. In comparison, Naive Bayes produced the lowest result, with a rate of 94.59%.

The Precision, Recall, F1-score, MSE, and RMSE metrics of the Ensemble Learning method were 95.89%, 97.22%, 96.55%, 0.0329, and 0.1814, respectively.

The confusion matrix of machine learning algorithms is given in Figure 3.

The statistical results obtained according to the dataset classes before the PCA application are given in Table 5.

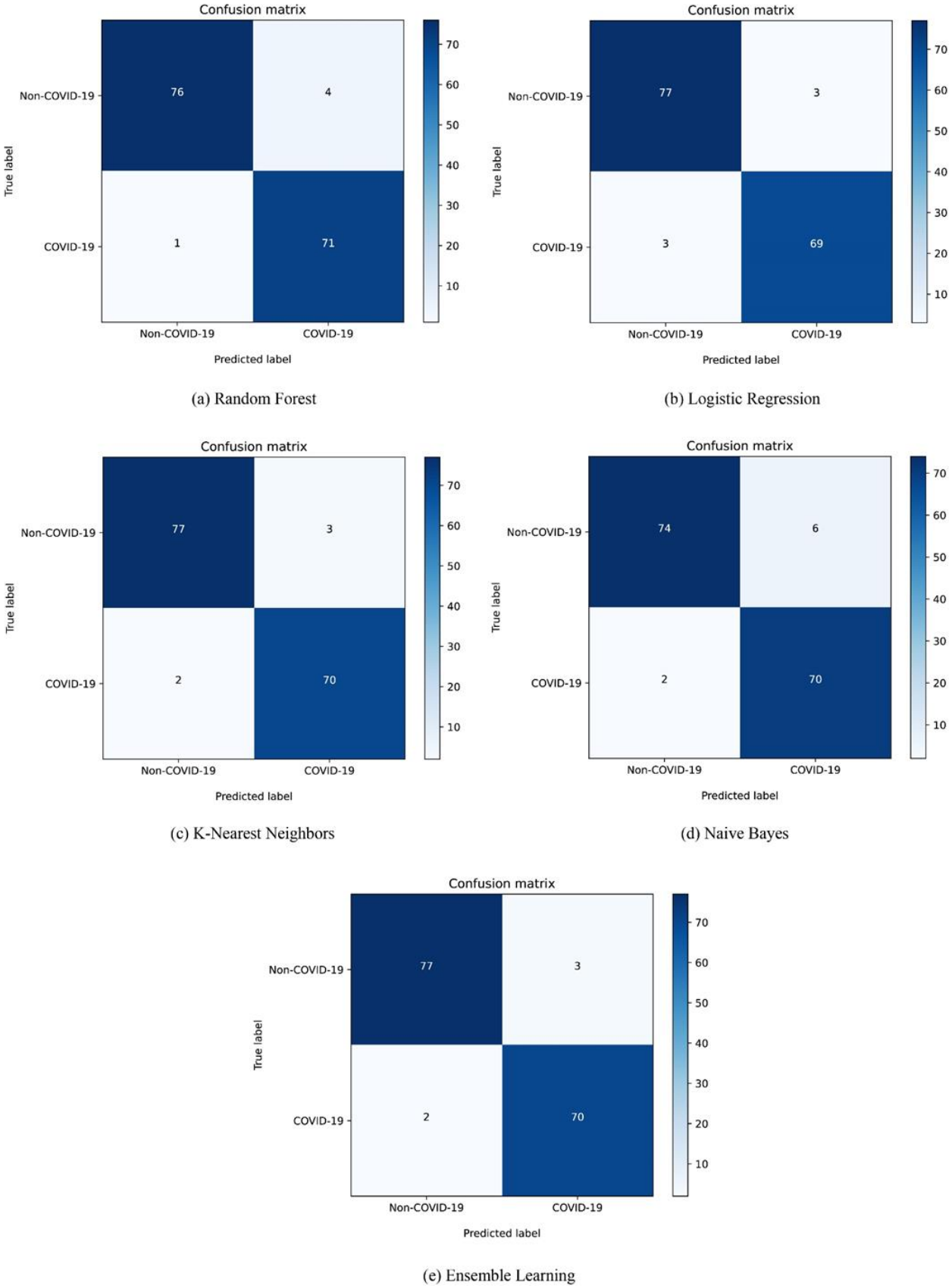

(a) Random Forest

(b) Logistic Regression

(c) K-Nearest Neighbors

(d) Naive Bayes

(e) Ensemble Learning

Figure 3. Confusion matrix visualization of machine learning algorithms (without PCA).

Table 4. Comparing the performance of algorithms (without PCA).

Models	Accuracy	Precision	Recall	F_1-score	MSE	RMSE
Random Forest	0.9671	0.9467	0.9861	0.9660	0.0329	0.1814
Logistic Regression	0.9605	0.9583	0.9583	0.9583	0.0395	0.1987
K-Nearest Neighbors	0.9671	0.9589	0.9722	0.9655	0.0329	0.1814
Naive Bayes	0.9474	0.9211	0.9722	0.9459	0.0526	0.2294
Ensemble Learning	0.9671	0.9589	0.9722	0.9655	0.0329	0.1814

Table 5. Results of before/after pre-training precision, recall, F1-score metrics (without PCA).

Model	Class	Precision	Recall	F_1-score	Number for testing
Random Forest	Non-COVID-19	0.9870	0.9500	0.9682	80
	COVID-19	0.9467	0.9861	0.9660	72
Logistic Regression	Non-COVID-19	0.9625	0.9625	0.9625	80
	COVID-19	0.9583	0.9583	0.9583	72
K-Nearest Neighbors	Non-COVID-19	0.9747	0.9625	0.9686	80
	COVID-19	0.9589	0.9722	0.9655	72
Naive Bayes	Non-COVID-19	0.9737	0.9250	0.9487	80
	COVID-19	0.9211	0.9722	0.9459	72
Ensemble Learning	Non-COVID-19	0.9747	0.9625	0.9686	80
	COVID-19	0.9589	0.9722	0.9655	72

In Table 5, the testing process was carried out with machine learning models and 152 CT images.

Before the PCA application, according to Table 5, the Random Forest algorithm produced 96.82% F1-scores in detecting 80 Non-COVID-19 images and 96.60% F1-scores in detecting 72 COVID-19 images. The K-Nearest Neighbors algorithm produced 96.86% F1-scores in detecting 80 Non-COVID-19 images and 96.55% F1-scores in detecting 72 COVID-19 images. The naive Bayes algorithm produced a 94.87% F1-score in detecting 80 Non-COVID-19 images and a 94.59% F1-score in detecting 72 COVID-19 images. While the Ensemble Learning method produces 97.47%, 96.25%, and 96.86% values, respectively, according to the Precision, Recall, and F1-score metrics in detecting 80 Non-COVID-19 images, it has Precision, Recall, F1-score metrics in detecting 72 COVID-19 images. It produced 95.89%, 97.22%, and 96.55% values, respectively.

Before the PCA application, in Figure 3a, the Random Forest model produced 5 incorrect (FN=1, FP=4) prediction results on 152 test images. However, at the same time, it performed successfully by making correct predictions for 147 (TN=76 and TP=71) test data exhibited. In Figure 3b, the Logistic Regression model produced 6 incorrect (FN=3, FP=3) prediction results on 152 test images, while correct predictions for 146 (TN=77 and TP=69) test data. In Figure 3c, the K-Nearest Neighbors model produced 5 incorrect (FN=2, FP=3) prediction results on 152 test images. At the same time, it predicted correctly for 147 (TN=77 and TP=70) test data and produced the most successful result with the Random Forest algorithm. In Figure 3d, the Naive Bayes model, which produced the lowest result before PCA, produced 8 incorrect (FN=2, FP=6) prediction results on 152 test images, while it predicted correctly for 144 (TN=74 and TP=70) test data. Finally, in Figure 3e, the Ensemble Learning method produced 5 incorrect (FN=2, FP=3) prediction results on 152 test images. In contrast, correct predictions for 147 (TN=77 and TP=70) test data, K-Nearest Neighbors, and Random Forest algorithms produced the most successful result.

After applying the PCA method, the Logistic Regression algorithm produced the most successful result with a value of 96.05%, according to the accuracy metric value. In the COVID-19 disease diagnosis process, Random Forest has the lowest success rate of 92.76% according to the accuracy metric value in this study (Table 6). Our other findings; according to the F1-score metric value, the Logistic Regression algorithm produced the most successful result with a rate of 95.83%, while Random Forest produced the lowest result at 92.52%. The Accuracy, Precision, Recall, F1-score, MSE, and RMSE metrics of the Ensemble Learning method were 93.42%, 91.89%, 94.44%, 93.15%, and 0.0658, 0.2565, respectively. The confusion matrix of machine learning algorithms is given in Figure 4.

After applying the PCA method, the statistical results obtained according to the dataset classes are given in Table 7. In Table 7, the testing process was carried out with machine learning models and 152 CT images.

After applying the PCA method, according to Table 7, the Logistic Regression algorithm produced 96.25% F_1-scores in detecting 80 Non-COVID-19 images and 95.83% F_1-scores in detecting 72 COVID-19 images. The Random Forest algorithm produced 92.99% F_1-scores in detecting 80 Non-COVID-19 images and 92.52% F_1-scores in detecting 72 COVID-19 images.

Table 6. Comparing the performance of algorithms (with PCA).

Models	Accuracy	Precision	Recall	F_1-score	MSE	RMSE
Random Forest	0.9276	0.9067	0.9444	0.9252	0.0724	0.2690
Logistic Regression	0.9605	0.9583	0.9583	0.9583	0.0395	0.1987
K-Nearest Neighbors	0.9408	0.9200	0.9583	0.9388	0.0592	0.2433
Naive Bayes	0.9342	0.9189	0.9444	0.9315	0.0658	0.2565
Ensemble Learning	0.9342	0.9189	0.9444	0.9315	0.0658	0.2565

Table 7. Results of before/after pre-training precision, recall, F1-score metrics (with PCA).

Model	Class	Precision	Recall	F_1-score	Number for testing
Random Forest	Non-COVID-19	0.9481	0.9125	0.9299	80
	COVID-19	0.9067	0.9444	0.9252	72
Logistic Regression	Non-COVID-19	0.9625	0.9625	0.9625	80
	COVID-19	0.9583	0.9583	0.9583	72
K-Nearest Neighbors	Non-COVID-19	0.9610	0.9250	0.9427	80
	COVID-19	0.9200	0.9583	0.9388	72
Naive Bayes	Non-COVID-19	0.9487	0.9250	0.9367	80
	COVID-19	0.9189	0.9444	0.9315	72
Ensemble Learning	Non-COVID-19	0.9487	0.9250	0.9367	80
	COVID-19	0.9189	0.9444	0.9315	72

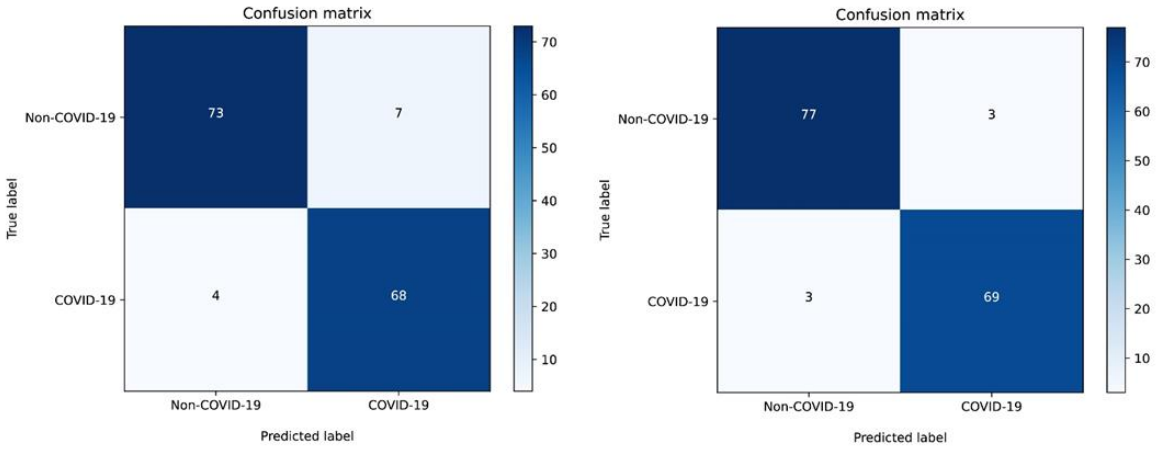

(a) Random Forest

(b) Logistic Regression

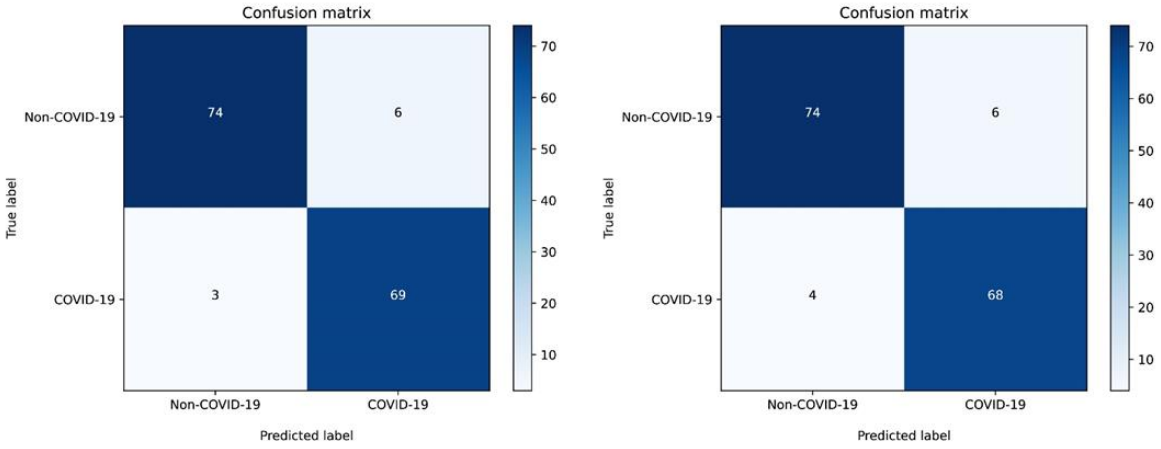

(c) K-Nearest Neighbors

(d) Naive Bayes

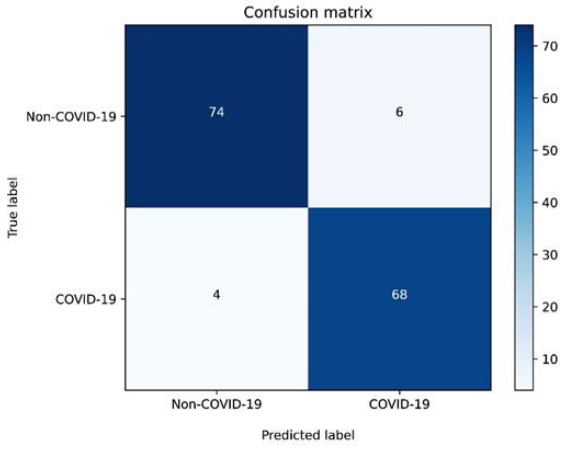

(e) Ensemble Learning

Figure 4. Confusion matrix visualization of machine learning algorithms (with PCA).

While the Ensemble Learning method produces 94.87%, 92.50%, and 93.67% values, respectively, according to the Precision, Recall, and F_1-score metrics in detecting 80 Non-COVID-19 images, it has Precision, Recall, F_1-score metrics in detecting 72 COVID-19 images. It produced 91.89%, 94.44%, and 93.15% values, respectively.

In Figure 4a, after applying the PCA method, the Random Forest model that produced the lowest result made 11 incorrect (FN=4, FP=7) prediction results on 152 test images while 141 (TN=73 and TP=68) correct for test data guessed.

In Figure 4b, the Logistic Regression model produced 6 incorrect (FN=3, FP=3) prediction results on 152 test images, while it correctly predicted 146 (TN=77 and TP=69) test data, achieving the most successful performance.

In Figure 4c, the K-Nearest Neighbors model produced 9 incorrect (FN=3, FP=6) prediction results on 152 test images, while it correctly predicted 143 (TN=74 and TP=69) test data.

In Figure 4d, the Naive Bayes model produced 10 incorrect (FN=4, FP=6) prediction results on 152 test images, while it predicted correctly for 142 (TN=74 and TP=68) test data.

Finally, in Figure 4e, the Ensemble Learning method produced 10 incorrect (FN=4, FP=6) prediction results on 152 test images, while it correctly predicted 142 (TN=74 and TP=68) test data.

According to Figure 5, before the PCA method was applied, the machine learning algorithms Random Forest, K-Nearest Neighbors, and Ensemble Learning produced the most successful results. In contrast, Naive Bayes had the most unsuccessful results.

After applying the PCA method, Logistic Regression produced the most successful result, while Random Forest produced the most unsuccessful result.

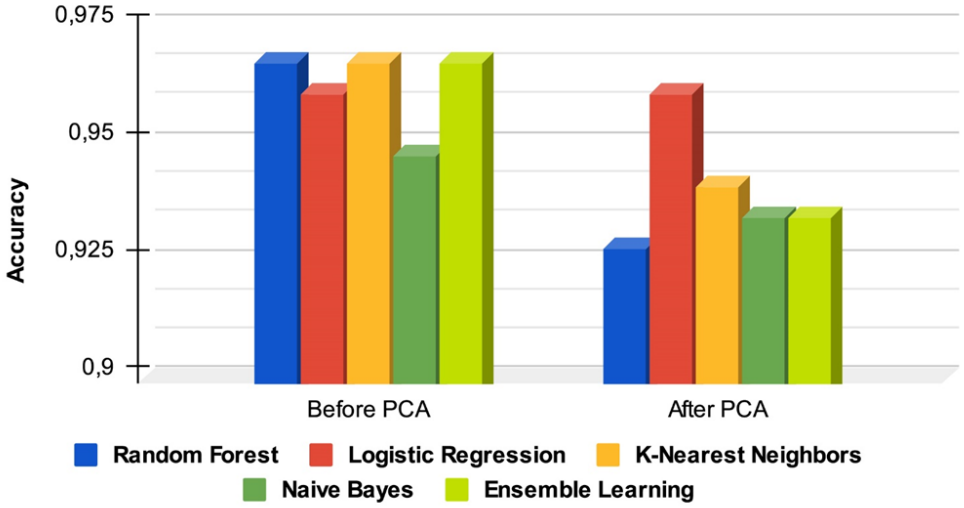

Figure 5. Chest CT dataset pre and after-PCA method accuracy values.

4. Discussion

In this paper, the definition of the most well-known machine learning-based methods were presented and explained to predict Covid-19-CT images. This study presents a comparative analysis for Random Forest, k-Nearest Neighbors, Logistic Regression, Naive Bayes algorithms of ML models to predict/diagnose the COVID-19 outbreak and suggests machine learning as a useful tool to predict COVID-19. The paper further suggests that the Ensemble learning method can realize better prediction. According to the statistical results, the ensemble learning model produced successful results.

The study can offer radiologists and clinical doctors a second perspective. COVID-19 diagnosis performed using machine learning-based algorithms can help radiologists and physicians report, interpret, and gain time. The experimental results of the proposed study with the Covid-19 detection studies in the literature are compared and given in Table 8.

According to Table 6, our proposed Ensemble Learning method achieved 96.71% accuracy with 757 images. The LBP-KNN method achieved an accuracy rate of 98.66% with 5000 images. In the study carried out with the MobileNet model, one of the deep neural networks, an accuracy rate of 94.74% was achieved with 757 medical images.

Table 8. Experimental comparison results of the proposed method and the studies in the literature.

Reference	Method	Number of images	Accuracy (%)
Chen [37]	HE-GLCM-SVM	296	75.69
Hasoon et al. [38]	LBP-KNN	5000	98.66
Barstugan et al. [39]	SVM	150	98.71
Yang et al. [40]	GLCM-SVM	180	85.95
Turk et al. [56]	MobileNet	757	94.74
Proposed	Ensemble Learning	757	96.71

5. Conclusion

In this study, machine learning methods are recommended for diagnosing COVID-19 patients. In detecting COVID-19, the Ensemble Learning method was used with Random Forest, Logistic Regression, K-Nearest Neighbors, and Naive Bayes algorithms. In the study, machine learning algorithms are optimized with Randomized Search CV method. In preparing the input dataset of machine learning models, the DenseNet201 deep learning model was pre-trained with ImageNet. In addition, the PCA method was also used in this process.

In the study's first phase, DenseNet201 architecture was used to obtain the COVID-CT dataset features. In the second step, the PCA method was applied to reduce the data size of the obtained feature vector. In the last stage, the Ensemble Learning method was applied for collective learning with optimized machine learning (RF, DT, KNN and Gaussian NB) algorithms used in the diagnosis process of COVID-19 patients. Experimental results are presented comparatively before and after PCA. Accordingly, in the pre-PCA diagnostic study, Random Forest, K-Nearest Neighbors, and Ensemble Learning methods produced the most successful results of 96.71%, while the Naive Bayes algorithm was the most unsuccessful model with an accuracy rate of 94.74%. In the post-PCA diagnostic study, the Logistic Regression algorithm produced the most successful result with an accuracy rate of 96.05%. In contrast, the Random Forest algorithm was the most unsuccessful model, with an accuracy rate of 92.76%. Our study produced very satisfactory results in this state.

However, different models are needed to reach a definite conclusion, including large datasets and deep learning algorithms. Machine learning techniques can be used effectively in disease detection as a secondary view.

Author contributions

Hatice Çatal Reis: Conceptualization, Methodology, Writing, and Editing-Reviewing. **Veysel Türk:** Software, Visualization, Investigation, Writing and Editing. **Serhat Kaya:** Data obtained, Pre-processing.

Conflicts of interest

The authors declare no conflicts of interest.

References

1. Shiri, I., Salimi, Y., Pakbin, M., Hajianfar, G., Avval, A. H., Sanaat, A., ... & Zaidi, H. (2022). COVID-19 prognostic modeling using CT radiomic features and machine learning algorithms: Analysis of a multi-institutional dataset of 14,339 patients. Computers in Biology and Medicine, 145, 105467. https://doi.org/10.1016/j.compbiomed.2022.105467
2. Del Rio, C., Omer, S. B., & Malani, P. N. (2022). Winter of Omicron—the evolving COVID-19 pandemic. Jama, 327(4), 319-320. https://doi.org/10.1001/jama.2021.24315.
3. Başeğmez, M., & Aydin, C. C. (2022). Türkiye'de COVID-19 sürecinde alınan önlemler çerçevesinde okul bahçe ve sınıflarının CBS ile değerlendirilmesi. Geomatik, 7(3), 209-219. https://doi.org/10.29128/geomatik.971403
4. Crawford, J., & Cifuentes-Faura, J. (2022). Sustainability in higher education during the COVID-19 pandemic: A systematic review. Sustainability, 14(3), 1879. https://doi.org/10.3390/su14031879
5. Maatuk, A. M., Elberkawi, E. K., Aljawarneh, S., Rashaideh, H., & Alharbi, H. (2022). The COVID-19 pandemic and E-learning: challenges and opportunities from the perspective of students and instructors. Journal of Computing in Higher Education, 34(1), 21-38. https://doi.org/10.1007/s12528-021-09274-2
6. Yig, K. G. (2023). Experiences of mathematics education teacher candidates in the emergency remote education: Reflections on the new normal. Mehmet Akif Ersoy University Journal of Education Faculty, (65), 549-577. https://doi.org/10.21764/maeuefd.1162499.
7. Panneer, S., Kantamaneni, K., Akkayasamy, V. S., Susairaj, A. X., Panda, P. K., Acharya, S. S., ... & Pushparaj, R. R. B. (2022). The great lockdown in the wake of COVID-19 and its implications: lessons for low and middle-income countries. International Journal of Environmental Research and Public Health, 19(1), 610. https://doi.org/10.3390/ijerph19010610
8. De Miquel, C., Domènech-Abella, J., Felez-Nobrega, M., Cristóbal-Narváez, P., Mortier, P., Vilagut, G., ... & Haro, J. M. (2022). The mental health of employees with job loss and income loss during the COVID-19 pandemic: the mediating role of perceived financial stress. International Journal of Environmental Research and Public Health, 19(6), 3158. https://doi.org/10.3390/ijerph19063158
9. Aldhafiri, F. K. (2022). COVID-19 and gut dysbiosis, understanding the role of probiotic supplements in reversing gut dysbiosis and immunity. Nutrition Clinique et Métabolisme, 36(3), 153-161. https://doi.org/10.1016/j.nupar.2022.01.003
10. Alves, M. H. M. E., Mahnke, L. C., Macedo, T. C., dos Santos Silva, T. K., & Junior, L. B. C. (2022). The enzymes in COVID-19: A review. Biochimie, 197, 38-48. https://doi.org/10.1016/j.biochi.2022.01.015
11. Chowdhury, M. E., Rahman, T., Khandakar, A., Mazhar, R., Kadir, M. A., Mahbub, Z. B., ... & Islam, M. T. (2020). Can AI help in screening viral and COVID-19 pneumonia?. IEEE Access, 8, 132665-132676. https://doi.org/10.1109/ACCESS.2020.3010287.
12. Siripanthong, B., Asatryan, B., Hanff, T. C., Chatha, S. R., Khanji, M. Y., Ricci, F., ... & Chahal, C. A. A. (2022). The pathogenesis and long-term consequences of COVID-19 cardiac injury. Basic to Translational Science, 7(3_Part_1), 294-308. https://doi.org/10.1016/j.jacbts.2021.10.011.
13. Raghav, A., Khan, Z. A., Upadhayay, V. K., Tripathi, P., Gautam, K. A., Mishra, B. K., ... & Jeong, G. B. (2021). Mesenchymal stem cell-derived exosomes exhibit

promising potential for treating SARS-CoV-2-infected patients. Cells, 10(3), 587. https://doi.org/10.3390/cells10030587
14. Cui, X., Chen, W., Zhou, H., Gong, Y., Zhu, B., Lv, X., ... & Ma, H. (2021). Pulmonary edema in COVID-19 patients: mechanisms and treatment potential. Frontiers in Pharmacology, 12, 664349. https://doi.org/10.3389/fphar.2021.664349
15. Puntmann, V. O., Carerj, M. L., Wieters, I., Fahim, M., Arendt, C., Hoffmann, J., ... & Nagel, E. (2020). Outcomes of cardiovascular magnetic resonance imaging in patients recently recovered from coronavirus disease 2019 (COVID-19). JAMA cardiology, 5(11), 1265-1273. https://doi.org/10.1001/jamacardio.2020.3557.
16. Douaud, G., Lee, S., Alfaro-Almagro, F., Arthofer, C., Wang, C., McCarthy, P., ... & Smith, S. M. (2022). SARS-CoV-2 is associated with changes in brain structure in UK Biobank. Nature, 604(7907), 697-707. https://doi.org/10.1038/s41586-022-04569-5
17. Sagris, M., Theofilis, P., Antonopoulos, A. S., Oikonomou, E., Tsioufis, K., & Tousoulis, D. (2022). Genetic predisposition and inflammatory inhibitors in COVID-19: where do we Stand?. Biomedicines, 10(2), 242. https://doi.org/10.3390/biomedicines10020242
18. Çatal Reis, H. (2018). Bone anomaly of the foot detection using medical photogrammetry. International Journal of Engineering and Geosciences, 3(1), 1-5. https://doi.org/10.26833/ijeg.333686.
19. Ai, T., Yang, Z., Hou, H., Zhan, C., Chen, C., Lv, W., ... & Xia, L. (2020). Correlation of chest CT and RT-PCR testing for coronavirus disease 2019 (COVID-19) in China: a report of 1014 cases. Radiology, 296(2), E32-E40. https://doi.org/10.1148/radiol.2020200642
20. La Salvia, M., Secco, G., Torti, E., Florimbi, G., Guido, L., Lago, P., ... & Leporati, F. (2021). Deep learning and lung ultrasound for Covid-19 pneumonia detection and severity classification. Computers in Biology and Medicine, 136, 104742. https://doi.org/10.1016/j.compbiomed.2021.104742
21. Fang, Y., Zhang, H., Xie, J., Lin, M., Ying, L., Pang, P., & Ji, W. (2020). Sensitivity of chest CT for COVID-19: comparison to RT-PCR. Radiology, 296(2), E115-E117. https://doi.org/10.1148/radiol.2020200432
22. Gupta, A., Gupta, S., & Katarya, R. (2021). InstaCovNet-19: A deep learning classification model for the detection of COVID-19 patients using Chest X-ray. Applied Soft Computing, 99, 106859. https://doi.org/10.1016/j.asoc.2020.106859
23. Zu, Z. Y., Jiang, M. D., Xu, P. P., Chen, W., Ni, Q. Q., Lu, G. M., & Zhang, L. J. (2020). Coronavirus disease 2019 (COVID-19): a perspective from China. Radiology, 296(2), E15-E25. https://doi.org/10.1148/radiol.2020200490
24. Ojha, V., Mani, A., Pandey, N. N., Sharma, S., & Kumar, S. (2020). CT in coronavirus disease 2019 (COVID-19): a systematic review of chest CT findings in 4410 adult patients. European radiology, 30, 6129-6138. https://doi.org/10.1007/s00330-020-06975-7
25. Tabatabaei, S. M. H., Talari, H., Moghaddas, F., & Rajebi, H. (2020). CT features and short-term prognosis of COVID-19 pneumonia: a single-center study from Kashan, Iran. Radiology: Cardiothoracic Imaging, 2(2), e200130. https://doi.org/10.1148/ryct.2020200130
26. Wang, Y., Dong, C., Hu, Y., Li, C., Ren, Q., Zhang, X., ... & Zhou, M. (2020). Temporal changes of CT findings in 90 patients with COVID-19 pneumonia: a longitudinal study. Radiology, 296(2), E55-E64. https://doi.org/10.1148/radiol.2020200843
27. Hani, C., Trieu, N. H., Saab, I., Dangeard, S., Bennani, S., Chassagnon, G., & Revel, M. P. (2020). COVID-19 pneumonia: a review of typical CT findings and differential diagnosis. Diagnostic and Interventional Imaging, 101(5), 263-268. https://doi.org/10.1016/j.diii.2020.03.014
28. Wang, K., Kang, S., Tian, R., Zhang, X., & Wang, Y. (2020). Imaging manifestations and diagnostic value of chest CT of coronavirus disease 2019 (COVID-19) in the Xiaogan area. Clinical Radiology, 75(5), 341-347. https://doi.org/10.1016/j.crad.2020.03.004
29. Liu, G., Wang, G., Yang, Z., Liu, G., Ma, H., Lv, Y., ... & Zhu, W. (2022). A lung ultrasound-based nomogram for the prediction of refractory Mycoplasma pneumoniae pneumonia in hospitalized children. Infection and Drug Resistance, 15, 6343-6355. https://doi.org/10.2147/IDR.S387890
30. Kaur, N., & Mittal, A. (2022). CADxReport: Chest x-ray report generation using co-attention mechanism and reinforcement learning. Computers in Biology and Medicine, 145, 105498. https://doi.org/10.1016/j.compbiomed.2022.105498
31. Gakhar, M., & Aggarwal, A. (2022). ThoraciNet: thoracic abnormality detection and disease classification using fusion DCNNs. Physical and Engineering Sciences in Medicine, 45, 961-970. https://doi.org/10.1007/s13246-022-01137-z
32. Packhäuser, K., Gündel, S., Münster, N., Syben, C., Christlein, V., & Maier, A. (2022). Deep learning-based patient re-identification is able to exploit the biometric nature of medical chest X-ray data. Scientific Reports, 12(1), 14851. https://doi.org/10.1038/s41598-022-19045-3
33. Roberts, M., Driggs, D., Thorpe, M., Gilbey, J., Yeung, M., Ursprung, S., ... & Schönlieb, C. B. (2021). Common pitfalls and recommendations for using machine learning to detect and prognosticate for COVID-19 using chest radiographs and CT scans. Nature Machine Intelligence, 3(3), 199-217. https://doi.org/10.1038/s42256-021-00307-0
34. Ardabili, S. F., Mosavi, A., Ghamisi, P., Ferdinand, F., Varkonyi-Koczy, A. R., Reuter, U., ... & Atkinson, P. M. (2020). Covid-19 outbreak prediction with machine learning. Algorithms, 13, 249. https://doi.org/10.3390/a13100249.
35. Canayaz, M., Şehribanoğlu, S., Özdağ, R., & Demir, M. (2022). COVID-19 diagnosis on CT images with Bayes optimization-based deep neural networks and machine learning algorithms. Neural Computing and Applications, 34(7), 5349-5365. https://doi.org/10.1007/s00521-022-07052-4

36. Muurlink, O. T., Stephenson, P., Islam, M. Z., & Taylor-Robinson, A. W. (2018). Long-term predictors of dengue outbreaks in Bangladesh: A data mining approach. Infectious Disease Modelling, 3, 322-330. https://doi.org/10.1016/j.idm.2018.11.004
37. Chen, Y. (2021). Covid-19 classification based on gray-level co-occurrence matrix and support vector machine. COVID-19: Prediction, Decision-making, and its Impacts, 47-55. https://doi.org/10.1007/978-981-15-9682-7_6
38. Hasoon, J. N., Fadel, A. H., Hameed, R. S., Mostafa, S. A., Khalaf, B. A., Mohammed, M. A., & Nedoma, J. (2021). COVID-19 anomaly detection and classification method based on supervised machine learning of chest X-ray images. Results in Physics, 31, 105045. https://doi.org/10.1016/j.rinp.2021.105045
39. Barstugan, M., Ozkaya, U., & Ozturk, S. (2020). Coronavirus (covid-19) classification using ct images by machine learning methods. arXiv preprint https://doi.org/10.48550/arXiv.2003.09424.
40. Yang, N., Liu, F., Li, C., Xiao, W., Xie, S., Yuan, S., ... & Jiang, G. (2021). Diagnostic classification of coronavirus disease 2019 (COVID-19) and other pneumonias using radiomics features in CT chest images. Scientific Reports, 11, 17885. https://doi.org/10.1038/s41598-021-97497-9
41. Currie, G., Hawk, K. E., Rohren, E., Vial, A., & Klein, R. (2019). Machine learning and deep learning in medical imaging: intelligent imaging. Journal of Medical Imaging and Radiation Sciences, 50(4), 477-487. https://doi.org/10.1016/j.jmir.2019.09.005
42. Tang, A., Tam, R., Cadrin-Chênevert, A., Guest, W., Chong, J., Barfett, J., ... & Canadian Association of Radiologists (CAR) Artificial Intelligence Working Group. (2018). Canadian Association of Radiologists white paper on artificial intelligence in radiology. Canadian Association of Radiologists Journal, 69(2), 120-135. https://doi.org/10.1016/j.carj.2018.02.0
43. Erickson, B. J., Korfiatis, P., Akkus, Z., & Kline, T. L. (2017). Machine learning for medical imaging. Radiographics, 37(2), 505-515. https://doi.org/10.1148/rg.2017160130
44. Yang, X., He, X., Zhao, J., Zhang, Y., Zhang, S., & Xie, P. (2020). COVID-CT-dataset: a CT scan dataset about COVID-19. arXiv preprint https://doi.org/10.48550/arXiv.2003.13865.
45. Huang, G., Liu, Z., Van Der Maaten, L., & Weinberger, K. Q. (2017). Densely connected convolutional networks. In Proceedings of the IEEE conference on computer vision and pattern recognition, 4700-4708. https://doi.org/10.1109/CVPR.2017.243.
46. Avci, C., Budak, M., Yagmur, N. & Balcik, F. (2023). Comparison between random forest and support vector machine algorithms for LULC classification. International Journal of Engineering and Geosciences, 8(1), 1-10. https://doi.org/10.26833/ijeg.987605.
47. Erdem, F., Derinpinar, M.A., Nasirzadehdizaji, R., Oy, S., Seker, D. Z. & Bayram, B. (2018). Rastgele orman yöntemi kullanılarak kıyı çizgisi çıkarımı İstanbul Örneği. Geomatik, 3 (2), 100-107. https://doi.org/10.29128/geomatik.362179.
48. Akar, O. & Tunc Gormus, E. (2019). Göktürk-2 ve Hyperion EO-1 uydu görüntülerinden rastgele orman sınıflandırıcısı ve destek vektör makineleri ile arazi kullanım haritalarının üretilmesi. Geomatik, 4 (1), 68-81. https://doi.org/10.29128/geomatik.476668.
49. Duman, H. S., & Başaraner, M. (2022). Şekil göstergeleri ve topluluk öğrenmesi sınıflandırma algoritmaları ile bina detaylarının şekil karmaşıklık analizi. Geomatik, 7(3), 197-208. https://doi.org/10.29128/geomatik.947334
50. Gong, M., Bai, Y., Qin, J., Wang, J., Yang, P., & Wang, S. (2020). Gradient boosting machine for predicting return temperature of district heating system: A case study for residential buildings in Tianjin. Journal of Building Engineering, 27, 100950. https://doi.org/10.1016/j.jobe.2019.100950
51. Nguyen, P. T., Ha, D. H., Avand, M., Jaafari, A., Nguyen, H. D., Al-Ansari, N., ... & Pham, B. T. (2020). Soft computing ensemble models based on logistic regression for groundwater potential mapping. Applied Sciences, 10(7), 2469. https://doi.org/10.3390/app10072469
52. Siddique, M. A. B., Sakib, S., & Rahman, M. A. (2019, December). Performance analysis of deep autoencoder and NCA dimensionality reduction techniques with KNN, ENN and SVM classifiers. 2nd International Conference on Innovation in Engineering and Technology (ICIET), 1-6. https://doi.org/10.1109/ICIET48527.2019.9290722
53. Apaydin, C., & Abdikan, S. (2021). Fındık bahçelerinin Sentinel-2 verileri kullanılarak piksel tabanlı sınıflandırma yöntemleriyle belirlenmesi. Geomatik, 6(2),107-114 https://doi.org/10.29128/geomatik.705988
54. Shahabi, H., Shirzadi, A., Ghaderi, K., Omidvar, E., Al-Ansari, N., Clague, J. J., ... & Ahmad, A. (2020). Flood detection and susceptibility mapping using sentinel-1 remote sensing data and a machine learning approach: Hybrid intelligence of bagging ensemble based on k-nearest neighbor classifier. Remote Sensing, 12(2), 266. https://doi.org/10.3390/rs12020266
55. Hou, S., Liu, Y., & Yang, Q. (2022). Real-time prediction of rock mass classification based on TBM operation big data and stacking technique of ensemble learning. Journal of Rock Mechanics and Geotechnical Engineering, 14(1), 123-143. https://doi.org/10.1016/j.jrmge.2021.05.004
56. Turk, V., Catal Reis, H. & Kaya, S. (2022). Automatic prediction of covid-19 from chest-computed tomography (CT) images using deep learning architectures. Gumushane University Journal of Science. https://doi.org/10.17714/gumusfenbil.1002738.

Mersin Photogrammetry Journal
https://dergipark.org.tr/en/pub/mephoj
e-ISSN 2687-654X

Accuracy comparison of mobile mapping system for road inventory

Hüseyin Kurşun *[1]

[1]Istanbul Technical University, Department of Geomatics Engineering, Türkiye

Keywords
Mobile Mapping System
Digital Twin
High-Definition Maps
Photogrammetry
Road Inventory

Research Article
DOI: 10.53093/mephoj.1334286

Received:28.07.2023
Revised: 31.08.2023
Accepted:31.08.2023
Published:17.10.2023

Abstract

Mobile Mapping Systems (MMSs) stand out as the preferred solution for achieving highly precise 3D environmental models, particularly in urban planning, highway mapping, asset inventory, corridor mapping, traffic safety evaluation, autonomous vehicle, digital twin, and emergency response mapping where traditional aerial or satellite surveys often fall short in providing precise data. Understanding the intricate factors that impact the accuracy of mobile mapping is pivotal to harnessing the full potential of this advanced measurement technique. This study analyzes the spatial accuracy of geographical data produced by the mobile mapping method, considering factors such as the speed of the mobile mapping tool, measurement time difference, camera shooting distance of the produced data, and differences in picture shooting distances. The acquired results were examined for their applicability in the production of inventory along the highway route, revealing their practical usability through analysis and findings. This investigation delves into the proficiency and precision benchmarks of mobile mapping systems, specifically in the context of creating road inventory and supporting decision-making for road systems. The study discusses the usability and accuracy criteria of mobile mapping systems for creating transportation inventory and decision support systems.

1. Introduction

The enormous growth of everyday socioeconomic activity and the long-term sustainability of contemporary societies depend on the proper utilization of road networks. Road infrastructure has the potential to be a significant financial asset for society and the economy in many developing nations, but this potential is frequently overlooked. This is primarily due to a lack of awareness regarding its true value. Furthermore, the absence of comprehensive information, insightful perspectives, and an understanding of the importance of investing sufficiently in road maintenance has led to chronic underfunding and gradual decline in quality. The degradation of the road network leads to the loss of essential infrastructure, particularly impacting connectivity. Additionally, poor management of road inventories has given rise to significant challenges, including a surge in uncontrolled traffic accidents and a lack of reliable data for autonomous high-definition mapping systems [1].

According to the Turkish Statistical Institute (TSI), between 2003 and 2022, as shown in Figure 1 an in-depth analysis of investments and funding of the transport and communication sector, focusing particularly on the month of June. Unveiled a substantial allocation of 1,670 billion intended to strengthen Türkiye's transportation system. This strategic allocation is poised to yield significant benefits, supporting critical areas like maintaining infrastructure, seamlessly expanding the highway network, and refining the road management system.

Significantly, substantial resources have been allocated to the highway sector, demonstrating a clear commitment. It's worth mentioning that a budget of 979.9 billion has been earmarked for highway development. This financial dedication aims to expedite the deployment of Information and Decision Support Systems, which are crucial instruments for proficiently overseeing Türkiye's expansive road network. However, the situation takes a different turn when we consider the staggering numbers. In Türkiye, the total number of registered vehicles reached a remarkable 27.525.301 by the end of June 2023, with land vehicles dominating the statistics. This significant volume of vehicles significantly contributes to the ongoing traffic crises and a surge in

* **Corresponding Author**
*(huseyinkursun@gmail.com) ORCID ID 0000-0002-0342-5210

Cite this article
Kurşun, H. (2023). Accuracy comparison of mobile mapping system for road inventory. Mersin Photogrammetry Journal, 5(2), 55-66

accidents. This pressing issue calls for immediate action to expand the road network and to enhance the management system for these roads.

In the expansive landscape of Türkiye, the transportation system stands as a vast network of highways. With the road length depicted in Figure 2, Türkiye's highway infrastructure paints a picture of connectivity and accessibility, playing a pivotal role in shaping the country's mobility and economic dynamics.

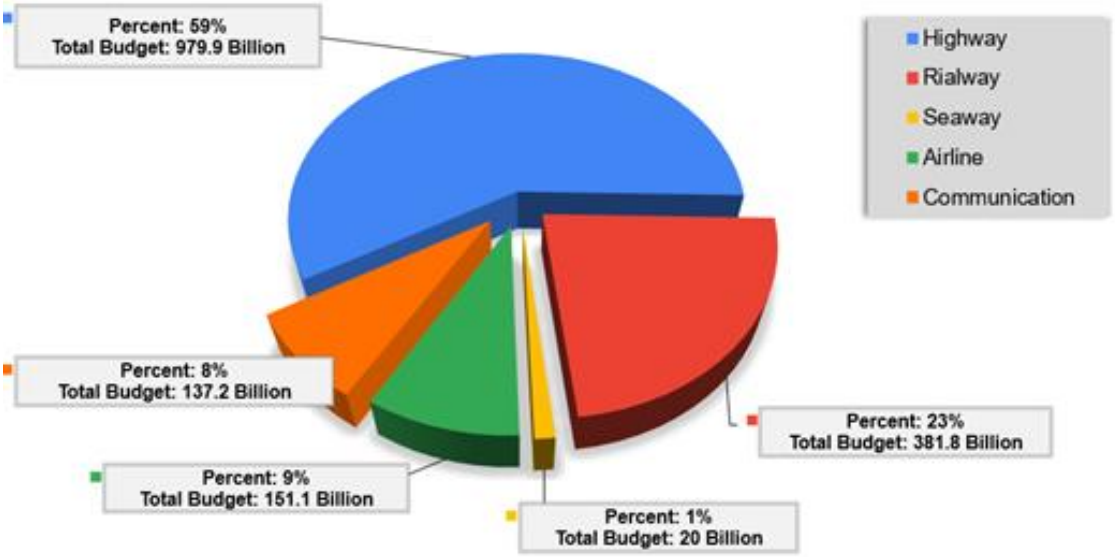

Figure 1. The distribution of transport and communication sector budget in 2022.

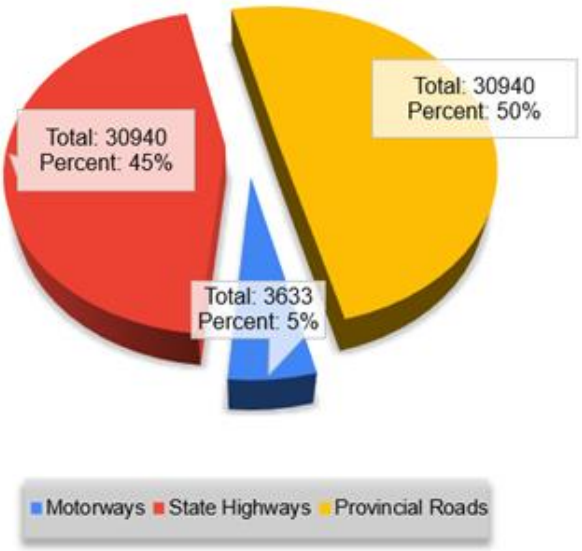

Figure 2. Road network according to surface types (km) in 2023.

The total road length in Türkiye stretches over 68.689 kilometers, and when considering both directions, it extends to 96.047 kilometers due to dual carriageways. This expansive road network includes numerous components, like guardrails spanning thousands of kilometers, road markings covering hundreds of thousands of kilometers, tunnels spanning hundreds of kilometers, thousands of bridges, over one hundred thousand intersections, millions of traffic signs, tens of thousands of signal lights, and a variety of other elements. Collectively, these elements contribute to an exhaustive inventory comprising over 4 million diverse items.

While technology aids data collection, visual inspections remain vital. Traditional methods like GNSS and total station require more teams, more times, and more costs. However, they're inefficient, lack adaptability for updates, and pose safety risks [2]. These limitations also hinder their support for varied data needs like animations and autonomous driving.

All of the mentioned disadvantages outlined herein are anticipated to be mitigated in the mobile mapping system, similar to how it can assist in inventory activities and maintenance and repair operations on linear routes such as highways and railways. Through the utilization of artificial intelligence technology, automatic inventory production can be achieved, and autonomous vehicles can utilize the data as sensors for HD map generation [3]. Furthermore, it is envisaged that this technology can be employed for incident scene investigation and information extraction from various vehicle accidents on highways. It inherently facilitates data quality control and enables the measurement of advertising display areas along roadways, among numerous other benefits.

It is also projected that the data acquired can be actively applied in various engineering projects, and as of the data collection date, new data can be generated for distinct research purposes.

Given the immense scope of the area and for large scale maps, the utilization of a Mobile Mapping system (MMS) emerges as a highly efficient and suitable approach.

Field studies differ in terms of cost, accuracy, detail and speed according to the measurement method used. In addition, depending on technological developments, measurement techniques and methods of obtaining spatial data have also changed throughout history. Spatial data from past to present are collected with different techniques and mapped at different scales.

Depending on the rapid developments in technology, at the end of the 1990s, classical measuring instruments are largely replaced by fully automatic measuring equipment, sensors and satellite technology. Although both terrestrial photogrammetry studies and classical field measurements are sufficient in terms of accuracy, in large areas it hardly provides sufficient performance in terms of speed and workforce on long roads. Therefore, there is a need for mobile mapping systems that will highlight the speed parameters.

The first studies within the scope of mobile mapping date back to the 1970s. In the 1970s, mobile mapping methods were used by photographic recording systems used by many road transport units in North America to monitor pavement quality, road maintenance efficiency, road obstructions, and for similar applications.

With the development of GNSS, IMU and other sensors have been integrated and used for positioning. Urban developments and growth in transportation infrastructure and developments in construction production speed have necessitated the development of more efficient and improved mobile mapping techniques. Some studies attempt to identify and categorize a sizable number of things. One such effort uses a patch-based match graph structure to discriminate between seven kinds of objects, including various types of vegetation. [4,5]. Extract urban objects. However, these systems encountered accuracy issues when a point cloud's resolution was insufficient to discriminate between a traffic sign's precise meaning, necessitating the analysis of optical pictures [6]. To enhance and better comprehend the dynamics of mobile mapping systems, it's imperative to delve into the contributing factors and their effects. These systems rely on a range of elements, including vehicle speed, time intervals, and image capture distances. Analyzing the potential influence of these factors on accuracy is a key aspect of optimizing mobile mapping techniques.

The systems can achieve centimeter-accurate instrument positioning of measured objects from geo-oriented image sequences and 3-dimensional coordinate accuracy in meters or sub-meter. Another advantage of mobile mapping systems is that the outbound data connection to a geodatabase is easy and simple. In general, the advantages of these sensors are numerous. Apart from the fact that 3D data has a well-established reputation for high dependability, employing a 3D point cloud to create 3D maps makes the process considerably simpler. In contrast to other 2D sensors, the 3D LiDAR dependably functions in all weather and lighting situations [7].

The collected geometric and attribute information can be used directly to create and update a database. With the development of rapid communication and image compression technologies, real-time image data can be transferred from mobile mapping system to the GIS database in the office environment. Moreover, such data can be studied and updated live with web, mobile and desktop applications.

Mobile mapping devices using CCD cameras or video cameras have been developed recently for mapping the inventory of roads. Road markings' size, shape, and color characteristics have been employed as crucial indicators for road marking extraction [8-10]. As a result, MMS technology delivers an inventive method for updating geospatial data, distinguished by quick data collecting and direct georeferencing over vast areas. Highway mapping, corridor mapping, and traffic safety evaluation are common MMS uses [11,12].

MMS finds diverse applications across multiple industries, serving as a versatile tool for a broad spectrum of technology-driven use cases.

When it comes to maintenance and disaster management, for instance, map updates might be too infrequent to fulfill the demands of regions that are developing quickly. Large-scale maps may often be updated using lidar data, satellite and aerial photos, and other data sources. The development of MMS technology over the past three decades provides several benefits for the collecting of geographical data, especially its low cost and excellent effectiveness [11-13].

Due to their great precision, speed, and cost-effectiveness in gathering 3D data as well as their use of autonomous driving technology, MMSs are now often used for Building Information Management (BIM) projects. Based on exact 3D positional data, high-definition maps offer the required road data for autonomous driving, such as lanes, signs, and road facilities [14]. The 3D reconstructed model of an asset is created using the gathered point clouds and pictures, which are then subjected to semantic segmentation or classification to extract comprehensive information about each constituent in the asset. The completed result is subsequently uploaded to the BIM software for the purpose of extracting and simulating crucial data pertaining to the project's life cycle. Typically, MMS can deliver data that are accurate enough for the generated BIM products [15].

The Digital Twin (DT) has been used in a variety of industries recently to develop more intelligent maintenance techniques [16]. DTs have been adopted for operation and maintenance in the road sector, including dealing with the maintenance of tunnels [17], bridges [18, 19], or road pavement [20]. The suggested models included both a detailed collection of classification metadata, such as materials, functions, and interactions between the components, and 3D geometry of the infrastructure components. The focus is on creating comprehensive models that encompass 3D geometry and semantic information about materials, functions, and relationships, with maintenance management systems being a key application of the Digital Twin concept.

The primary aim of this study is to establish a to make accuracy assessment for the usability of mobile mapping systems in road inventory production. This study focuses on a road inventory project conducted using a mobile mapping system developed in-house, comprising a laser scanner, panoramic camera, and Inertial Measurement Unit (IMU). To evaluate the accuracy of the mobile mapping system developed for road inventory collection, a precision comparison was carried out within a scenario created on the ITU Ayazaga Campus. This comparison took into account factors such as distance, speed, and the brightness of the sun. In this study, data generation rate, usage areas and location accuracy of the data produced, especially the production and manageability of

transportation data and asset management data in transportation networks were investigated using mobile mapping methods. From the obtained panoramic images and LiDAR data.

1.1. Using MMS in asset management system

Asset management is an essential component of infrastructure and superstructure projects. Updating and maintaining asset information comes with a hefty price. Recently, it has become possible to solve the difficulties arising from time and cost in data collection with MMS methods.

Making intelligent choices regarding the administration and upkeep of infrastructure is made easier with the use of GIS, which offers a tangible mapping between geographical data and associated attribute details. Recent developments in GIS technology have increased the effectiveness of asset and stock management [21,22]. Viewing a positioned asset provides better visualization and helpful decision making. Enforcement of connectivity, constraints, and topologically located relationship constraints helps urban maintain data integrity and inconsistency. A range of commercial software with Enhanced Maintenance Management System features has been very popular in the GIS industry for almost fifteen years. From road inventory management to public safety in road, electricity, water, gas, and utilities, GIS asset management systems are applied to nearly every area of utility.

MMS has contributed to the development and collection of the asset inventory database in terms of time, cost and quality. The most prominent features include road centerlines, road boundaries, lanes, sidewalks, curbs, pillars, signage, and roadside vegetation/trees. Transport assets mainly consist of roads and sidewalks. However, other assets such as signage, signal lights, poles and electricity, telecommunications and water utilities found above and below roads and sidewalks also belong to the main components of transportation assets. These assets help increase the efficiency of the road network and thus improve transportation safety [23].

MMS differs from the traditional mapping method with its fast data collection and low cost. For example, MMS can collect more than 3000 kilometers of road data per month. It basically differs from the traditional mapping method with its fast data collection speed and low cost. Although mobile mapping systems greatly reduce data collection time, it often takes more time and resources than data collection times to extract the requested data from the collected data. Therefore, most of the time and resources to create an inventory of assets are spent digitizing the data and entering its details. Due to the heavy workload during the digitization of data, research involving semi-automatic and automatic feature extraction methods from mobile mapping data has gained importance and some progress has been made.

Traffic signposts serve as a crucial part of our transportation system. They have a significant role within the Intelligent Transportation System (ITS), ensuring safety and providing route guidance through the power of Artificial Intelligence (AI). The information of pole-like objects may be utilized for ITS-related applications such as semantic mapping, improved driver assistance, road infrastructure maintenance, and smart city applications. For example, the location of street light poles may be utilized to enhance the stability of road monitoring for a driver assist system [24].

2. Mobile mapping system

The concept of a mobile mapping system integrating multiple sensors of a mobile platform dates back to the past. Although satellite positioning technology such as GNSS was not available during this time, a combination of accelerometers, gyroscopes, and odometer were used to determine the vehicle's motion and direction. Photographs are georeferenced according to recorded vehicle locations [23]. In addition, the possibility of precise positioning and direct georeferencing emerged using GNSS in kinematic mode. The combination of direct georeferencing advances and digital imaging technology has allowed for reduced costs, better precision, and increased flexibility and evolution of the Mobile Mapping System. Obtaining the third dimension and point cloud from overlapping stereo images or panoramic images is possible with the development of software technologies, while the cameras record the existing images of the field. On the other hand, laser scanners calculate the spacing and direction of laser points and directly output the three-dimensional coordinate of each point in the scene. Thus, combining laser scanners with this system allows us to obtain the coordinates of points in three-dimensional space. Integrating this geo-referenced multi-sensor data offers better opportunities to find solutions to specific problems in the spatial domain [25].

An important consideration when moving from traditional mapping methods to mobile mapping technology is the high initial cost of the system. The feasibility of creating an affordable MMS utilizing low-cost laser scanners and budget-friendly cameras has been achieved through diverse methodologies.

2.1. MMS requirements

MMS consists of laser scanner(s), GNSS, an IMU, a DMI, and digital camera(s) [26,27].

The main components of the MMS built for data collection purposes include the following:

2.1.1. One or more laser scanners

LiDAR records 3D point data of the environment in the frame of the data generation scene, which helps to create a 3D model of the scene and extract features.

2.1.2. One or more camera

Cameras capture pictures/video frames of the site, thus providing their managers with digital pictures or videos showing the conditions of the assets.

2.1.3. Global navigation satellite system receiver (GNSS)

The common system to determine the accurate 3D positions in open areas is Global Navigation Satellite System (GNSS). It uses triangulation method with using multiple satellite systems such as GPS, GLONASS, Galileo, and BeiDou to determine precise position. The accuracy of this system is around meter-level however it can be decreased to centimeter level with using these 2 methods which are Differential GPS (DGPS) and Real-Time Kinematic GPS (RTK-GPS) [28]. All in all, Mapping System (MMS) aims for 5-50 mm accuracy with fusion sensors even at high speeds in open areas.

2.1.4. Inertial measurement unit (IMU)

The Inertial Measurement Unit (IMU) is a self-contained sensor that records relative orientation, acceleration, and magnetometer data in 9 axes. It can calculate the position from the start point since it doesn't use any external sources. The measurements from the accelerometer, gyroscope, and magnetometer are used by an onboard computing unit with a dead reckoning algorithm for real-time positioning, forming an Inertial Navigation System (INS). The accuracy of this device mainly depends on the accuracy of sensors used. IMUs can function indoors, outdoors, and in GNSS-denied environments, but the accuracy is limited to short periods relative to the start point due to dead reckoning. Fusing the IMUs and GNSS is a common approach for precise positioning.

2.1.5. Distance measuring instrument (DMI)

The Distance Measurement Instrument (DMI) is used to measure the distance traveled. This system used in the MMS to increase the accuracy of MMS system. This unit can measure the distance, velocity and acceleration after it calibrated.

2.1.6. On-board computer

It is equipped with software or programs that control the operation of sensors and record their data. Point cloud data obtained from the laser scanner at hundreds of thousands of points per second, panoramic images captured at desired intervals, GNSS data, and IMU data are quite voluminous. There is a recording unit and a video card with a high data recording speed. If a laptop/tablet is used for remote connection, it is important to enable Wi-Fi on the computer.

2.1.7. Mobile platforms

Such as a car or truck in land applications, an airplane or drone in aerial applications.

Figure 3 presents a detailed visual representation of the components found within MMS.

Figure 3. MMS data lifecycle.

$$\begin{bmatrix} X_P \\ Y_P \\ Z_P \end{bmatrix} = \begin{bmatrix} X_{GNSS} \\ X_{GNSS} \\ Z_{GNSS} \end{bmatrix} + R^M_{IMU}(\omega, \varphi, \kappa).\left(R^{IMU}_S(\Delta\omega, \Delta\varphi, \Delta\kappa).r^s_P(ad) + \begin{bmatrix} L_X \\ L_Y \\ L_Z \end{bmatrix}^{IMU}_S - \begin{bmatrix} L^{\frac{G}{I}}_X \\ L^{\frac{G}{I}}_Y \\ L^{\frac{G}{I}}_Z \end{bmatrix}^{IMU}_{GNSS} \right) \quad (1)$$

Mobile laser scanning systems work in the global geodetic coordinate system [29,30]. The measuring principle of mobile LiDAR systems coordinates can be calculated by the Equation 1 [31].

Where; X_P, Y_P, Z_P : Location of the target P in the ECEF Coordinate system;

$R^M_{IMU}(\omega, \varphi, \kappa)$: Rotation matrix between IMU and ECEF (Earth Center Earth Fixed);

$R^{IMU}_S(\Delta\omega, \Delta\varphi, \Delta\kappa)$: rotation matrix between the IMU and the laser scanner; $X_{GNSS}, Y_{GNSS}, Z_{GNSS}$: Location of GNSS antenna in ECEF System; L_X, L_Y, L_Z : Lever-arm distance from the navigation and IMU origin to the laser scanner origin; $L^{\frac{G}{I}}_X, L^{\frac{G}{I}}_Y, L^{\frac{G}{I}}_Z$: Lever-arm offsets from the IMU origin to the GNSS origin;

R^{INS}_S : Rotation matrix between the laser scanner and IMU; r^S_P : Relative position vector of Point P in the laser scanner coordinate System.

Refer to Figure 4 for the coordinate system visual.

3. Case study

3.1. Designed MMS architecture

Vehicle design involves harmonizing onboard equipment, calibrating components, optimizing their placement, and managing the associated software, ensuring seamless functionality and synergy.

As a Panoramic camera on the vehicle, Ladybug 5+ brand camera with 30 MP resolution, Velodyne VLP-32c, LiDAR sensor and instant acceleration during picture taking. IMU works in integration with the Applanix Poslv MMS and the Odometer (DMI), which enables panoramic shooting by triggering according to the determined quantity and two GNSS antenna cameras to receive

precise coordinates. MMS system used in this study was designed and integrated by our research team. Figure 5 above provides visual insight and the graphical representation of the top view of the system is also shown in Figure 6.

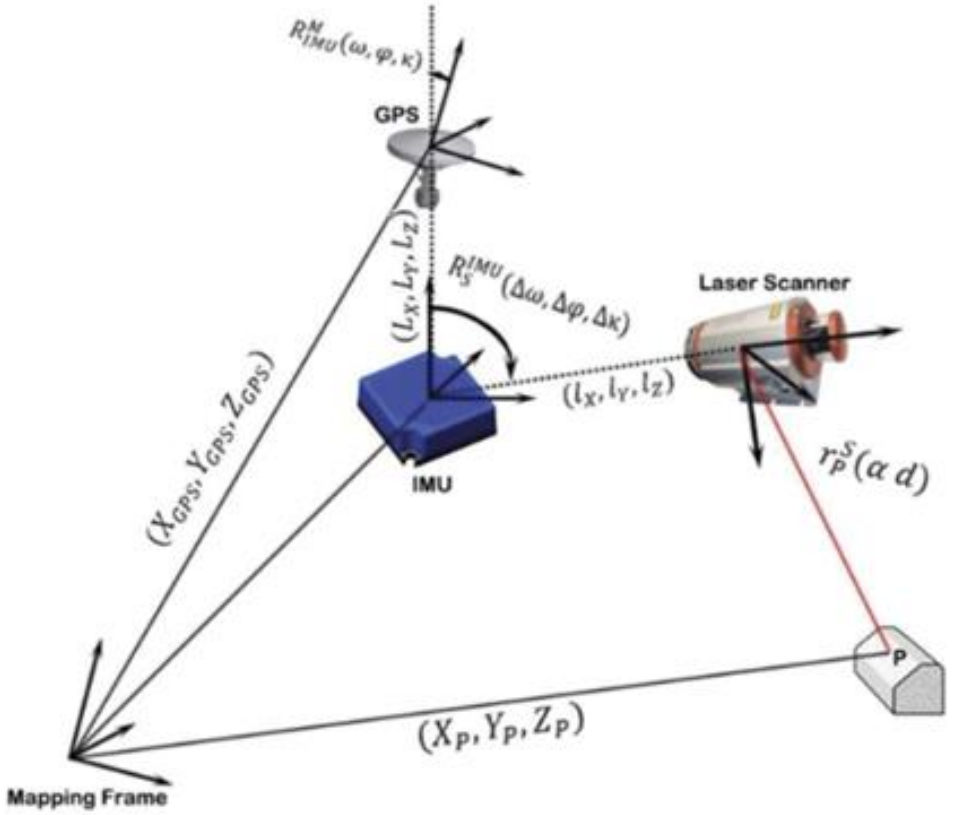

Figure 4. Mobile LiDAR geometric measurement coordinate system [28].

Figure 5. Image of MMS designed by our research team.

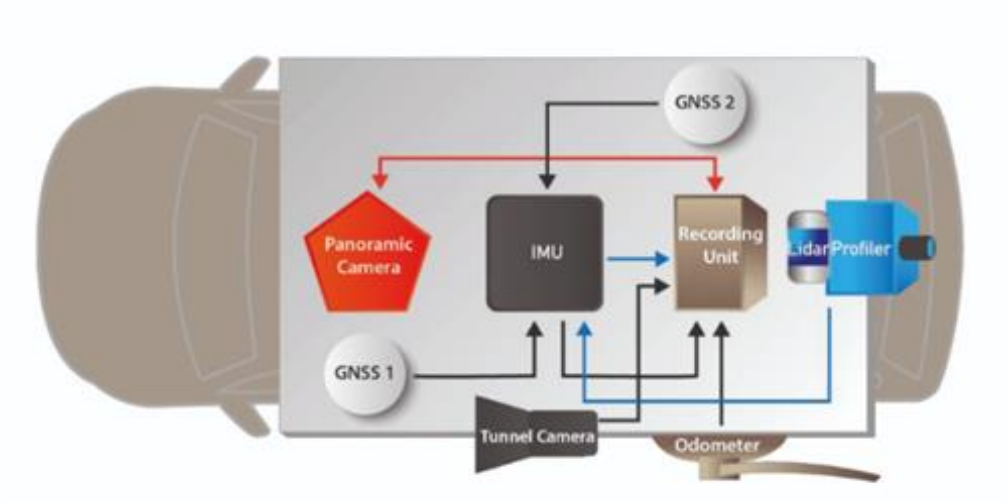

Figure 6. Top view of MMS designed by our research team.

3.1.1. Velodyne VLP-32c laser scanner

For mapping purposes, the Velodyne laser scanner is often used. These scanners, which are primarily used for obstacle detection in robotics applications, feature just one laser diode, as seen in Figure 7. Velodyne features 32 channels and a laser with a vertical range of +15 to -25 degrees.

Figure 7. Velodyne VLP-32c in the test measurement.

With a range accuracy of up to 3 cm, the LiDAR head can spin 360 degrees in a two-dimensional plane. The sensor works on an infra-red band with a wavelength of 903 nm. equipped with an angular resolution (Horizontal/Azimuth): 0.1° to 0.4°, and frame rate: 5 Hz to 20 Hz.

3D Lidar Data Points Generated:

Single Return Mode: ~600,000 points per second

Dual Return Mode: ~1,200,000 points per second

The range of these locations is calculated using the duration of flight technique. The sensor's normal range is 1 to 200 meters. Velodyne is a natural candidate for creating affordable mapping solutions because of these qualities. Velodyne Lidar (2022) specifications (https://velodynelidar.com/wpcontent/uploads/2019/12/63-9378_Rev-F_Ultra-Puck_Datasheet_Web.pdf) (2023).

3.1.2. Flir Ladybug5 panoramic camera

Ladybug5+ camera, takes 360-degree panoramic pictures and is widely used in mobile mapping systems as shown in Figure 8. Here are some of the features of this camera:

- It consists of 6 cameras of 5 Mega Pixel. A total of 30 megapixel and frame rate panoramic images are obtained.
- Data output in various formats is provided with Global Shutter readout method in 8-bit, 12-bit, 16-bit, JPEG.
- Image resolution 2048 x 2448 and pixel size Mar.45.
- It has the capacity to shoot video up to 60 fps and it has the capacity to broadcast live 360-degree video.
- Various adjustments can be made via its own software, such as gamma value, white adjustment, etc.
- Triggers can be given externally.
- It has day and night shooting features.

Figure 8. Ladybug 5+ in the test measurement.

For more information explore the homepage: (Teledyne Flir (2022) Ladybug5+ specifications www.flir.com/products/ladybug5plus/?vertical=machine+vision&segment=iis) (2023). It takes pictures at equal distances and collects detailed data about the route along the route. Tigger box (trigger box) instrument is used to collect data at equal distances. This device transmits the trigger received from the DMI (Distance Measuring Indicator) to the camera and records the time the picture was taken to the computer along with the picture.

3.1.3. Applanix Pos lv 420 IMU/GNSS/DMI

A GNSS-IMU integrated solution is provided by the Applanix Poslv420 instrument. It is composed of a GNSS that offers locations with a horizontal precision of 2 cm and a vertical accuracy of 5 cm in L1/L2 post-processed mode, and a horizontal accuracy of 3 cm and a vertical accuracy of 5 cm in L1/L2 Sensors real-time kinematic mode.

The desired absolute precision of feature points for a mapping application is <20 cm. Its 420 unit is lightweight and well suited for mobile mapping applications because it weighs 2.6 kg and is 158 x 158 x 124 mm. At a frequency of 200Hz, it offers a navigational answer. Several GNSS performance requirements include:

X,Y Position (m): Accuracy of 0.020 meters.

Z Position (m): Precision of 0.050 meters.

Roll & Pitch (degrees): Deviation limited to 0.015 degrees.

True Heading (degrees): Error within 0.020 degrees.

For more information and for a visual representation, refer to Figure 9 and the homepage below: Applanix (2022) POS LV420 specifications www.applanix.com/downloads/products/specs/POS-LV-Datasheet.pdf (2023).

Figure 9. We used IMU in the test measurement

3.2. Data Collection

To establish the basis for investigations into the feasibility of using mobile mapping systems for road inventory production, we selected a test area for accuracy determination studies. ,At the Istanbul Technical University ITU Ayazaga Campus, our study area spans a 250-meter measurement zone along the intersecting routes of Prof. Dr. Bedri Karafakıoğlu street alongside the sport road, shaping a perpendicular alignment as shown in Figure 9. For point position precision measurements, triangulation was made at 3 different points, static measurements were made, and the coordinates of the points were calculated. Along the measurement route area, used on sidewalks, building corners and details, routing signs, lighting poles and guardrails, etc. At 40 points, the detail points to be measured were established by sticking paper reflectors that can remain until the completion of our field work at Figure 10. The establishment of MMS was strategically guided by identifying optimal locations and the specific types of details essential for measuring and producing comprehensive database information. Using total station measurement devices installed at triangulation points, a series of precise measurements were conducted for each point, resulting in the calculation of their coordinates.

The measured point coordinates were calculated according to Universal Transverse Mercator UTM coordinate systems. Heights were measured using an orthometric method.

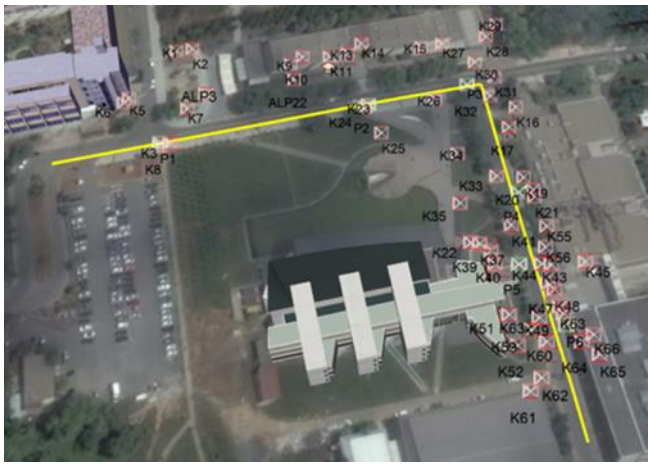

Figure 10. ITU Ayazağa Campus field studies area.

3.2.1. Data collection with mobile mapping in the field

Data were collected with MMS for point location accuracy measurements at ITU Ayazağa Campus. In order to collect data with the MMS, panoramic pictures were taken at 20 and 40 km speeds, 3, 5, 10 m intervals as shown in Figure 11 and laser point cloud data were collected with the Mobile Mapping tool at different times in the morning, noon and afternoon on two different days.

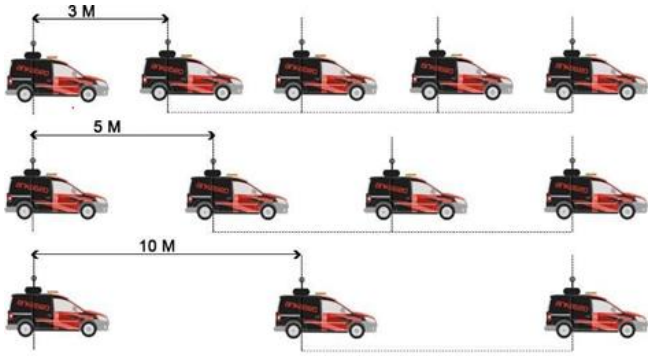

Figure 11. Measurements based on captured image distance intervals

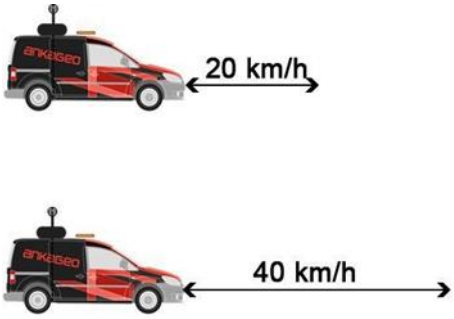

Figure 12. Speed measurements within interval ranges.

Data was collected from the field on December 19, 2018 at 14:00 and 16:50, and on Saturday, December 20, at 9:30, 12:30 and 16:50, 2 days in 5 different time intervals. At each measurement time, 25 different data collection processes were carried out with different parameters at 5 different time intervals from the field at 20 km/h and 40 km/h vehicle speeds as referred in Figure 12, and at each vehicle speed at 3 m, 5 m and 10 m picture shooting intervals.

3.2.2. Mobile mapping data and Geo-Coordinating of data

The relative GNSS positioning method was used based on the reference station named ISTN belonging to TUSAGA-Active CORS Network. On the Mobile Mapping Web application software, the coordinates of 40 points were measured by marking the panoramic images and taking their positions from the laser points where the comparisons were made by making a full series of measurements of the same points by taking the geodetic point of departure from the triangulation point on the campus.

4. Results and Discussion

4.1. Post-Processing of data collected by MMS from the field

Data from Panoramic camera, Lidar, IMU, GNSS, and DMI in the field are recorded in real time from the recording unit. These data are pre-processed with special software, aimed at reducing the margin of error in real-time data collected from the field. Firstly, the data coming from the recording unit is loaded into the post-processing software. Additionally, Rinex data taken from the fixed stations closest to the location where the data was acquired is uploaded to the software. It is important to determine the fixed stations that are near the data from the field. To ensure high accuracy in spatial details, a post-processing technique was applied where the raw real-time trajectory data is refined using the POSPac MMS software as referred in Figure 13. The collected data from the field is in its raw form, often accompanied by GNSS error biases. To rectify this, POSPac MMS software is employed along with data from static GNSS stations located near the capture site. This combination allows for post-processing of the data. Subsequently, the refined information is integrated with reference stations using the Rinex format, resulting in the extraction of accurate trajectory data. By post-processing method generating position data with an accuracy of up to 1 cm with the assistance of Rinex data.

Figure 13. Post-processing method in POSPac MMS software.

4.2. Accuracy Comparison

In this study, coordinates were calculated on the measurements of 40 target points along the road route for point location precision. The x and y coordinates of the points were calculated by making a predictive calculation with the data obtained from the electronic length meter. Since the distance measurement accuracy of the electronic length meter used was 2 mm ± 2 ppm, the predictive data were used for validation. For

comparison with the MMS method, the coordinates of the points measured on the software were compared. The coordinates obtained with the geodetic method were taken as the real values and the coordinates obtained with the MMS were compared by calculating the mean square error. The obtained results are shown in Table 1. This study focused on developing MMS and assessing its real-world performance, including applicability, accuracy, and usability, through field measurements.

Table 1. Comparison of data.

Time	Picture Taking Range (m)	Speed (km/h)	Differences (cm)			
			Min.	Max.	Mean	KOH
Morning	3	20	3,3	20,4	11,56	12,17
		40	2,8	17,9	10,36	10,91
	5	20	3,8	32,8	11,23	12,62
		40	2,6	21,4	10,03	10,72
	10	20	3	23,8	13,14	14,05
		40	2,4	21,2	10,1	10,75
Noon	3	20	2,7	19,1	10,6	11,13
		40	1,6	18,3	8,7	9,4
	5	20	2,2	19	10,11	11,28
		40	2,5	25	10,29	11,52
	10	20	1,1	22,5	10,77	11,99
		40	4,2	16	10,29	10,85
Evening	3	20	3,2	19,9	10,28	11,12
		40	2,5	23,7	10,2	11,38
	5	20	1,9	17,9	10,9	11,74
		40	1,4	17,5	9,07	9,89
	10	20	1,8	25,2	13,26	14,66
		40	3,3	28,3	10,41	11,55

4.3. Comprehensive analysis and uncovering result

Analyzing Measurement Variability in Shooting Range Data: Insights and Implications based on the measurements in Table 1.

4.3.1. Consistency across shooting ranges and time variations

The shooting range distances of 3 m, 5 m, and 10 m did not yield significant differences in measurements. Notably, measurements at 3 m and 5 m intervals exhibited remarkable proximity. The variation observed across different times of the day (morning, noon, and evening) was consistently below 2 decimeters (dm).

4.3.2. Impact of image density on measurement differences

There was a correlation between image density and measurement variations. Notably, increased image density yielded comparable differences for sections up to 25 meters.

4.3.3. Spatial features and measurement variability

While measurements generally presented differences below 2 dm, variations between 1 cm and 1 dm were evident. Notably, objects such as curbs, guardrails, advertisement signboards, and lighting poles contributed to these variations. Most of these objects exhibited a parallel or close alignment with the camera.

4.3.4. Time of day and measurement precision

Measurements taken at noon exhibited enhanced accuracy, indicating a 1-2 cm improvement compared to morning and evening measurements. This difference may stem from factors like varying lighting conditions and temperature-induced systemic changes during the morning and evening.

4.3.5. Impact of vehicle speed on measurements

Measurements taken at a speed of 40 km/h demonstrated greater accuracy compared to those taken at 20 km/h. This disparity is attributed to challenges in stabilizing the vehicle at lower speeds.

4.3.6. Optimal picture intervals for accuracy

Picture intervals of 3 m and 5 m yielded superior results compared to the 10 m intervals. The latter intervals led to data loss, impacting measurement precision.

4.3.7. Range dependency and measurement precision

Measurements conducted within the 0-10 m range consistently provided more accurate results than measurements within the 10-25 m range.

To sum up, this comprehensive analysis of shooting range measurements underscores the nuances influencing measurement variability. Factors like image density, spatial features, time of day, vehicle speed, and picture intervals all play crucial roles in shaping the accuracy and reliability of measurements. These insights offer valuable considerations for enhancing the precision of shooting range data collection and analysis.

5. Conclusion

This study has explored the usability of mobile mapping methods in road inventory and asset management systems. Both image technology and laser technology were utilized in the mobile mapping process, resulting in accurate and consistent data collection. The obtained measurements were compared with the geodetic measurement method as an accuracy reference.

The research revealed that mobile mapping systems can efficiently collect point and linear data, such as traffic signs, lighting poles, road centerlines, trees, building corners, and more, along with attribute information and symbology. The achieved location accuracies demonstrated that this technology is highly effective for city road, highway, and railway inventory collection, as well as building facade surveys. While the Mobile Mapping System data might not meet the precision requirements for cadastral surveys, its panoramic imagery offers extensive visual insights and verification possibilities. As a result, it proves to be a valuable asset for urban planning, asset management, and road safety improvement.

The study highlights the Mobile Mapping System's potential to revolutionize map applications, bringing a three-dimensional dimension to the mapping experience in terms of accuracy where the successful implementation of a low-cost system, maintaining high-quality georeferenced information, underscores the practicality and efficacy of this approach. The obtained data from mobile mopping can be used in production high resolution map HD maps for autonomous vehicles.

In addition to its practical applications, the Mobile Mapping System plays a crucial role in enhancing road safety by managing and increasing the sustainability of road safety equipment data, supporting Regional Operations and Engineering Services. Considering its diverse applications and numerous advantages, the Mobile Mapping System emerges as an indispensable tool in today's data-driven landscape. As the technology continues to advance, it promises to reshape asset inventory mapping and solidify its position as a key component of modern mapping practices.

In this study, the method employed involves a mobile mapping system that, in addition to measurement purposes, has a broad range of applications in various fields. However, the lack of a nationally accepted regulation (standard) for its use could potentially limit the practicality of the study. It is believed that this study could make a significant contribution to the process of preparing such a regulation, which would facilitate the utilization of this technology.

Acknowledgement

The research presented in this paper is part of Doctoral Dissertation of the first author carried out at Graduate School of Istanbul Technical University (ITU). The author is deeply grateful to his supervisor, Prof. Dr. Reha Metin Alkan for his guidance.

Conflicts of interest

The authors declare no conflicts of interest.

References

1. Natsui, R. K., Mireku, K. K., Amuzu, G. G. K., & Sasu, E. (2022, June). An Integrated Geographical Information and Road Asset Management System for road transport network sustainability in developing countries. 28th International Conference on Engineering, Technology and Innovation (ICE/ITMC) & 31st International Association for Management of Technology (IAMOT) Joint Conference (pp. 1-6). IEEE. https://doi.org/10.1109/ICE/ITMC-IAMOT55089.2022.10033144.
2. Keleş, M. D., & Aydin, C. C. (2020). Mobil lidar verisi ile kent ölçeğinde cadde bazlı envanter çalışması ve coğrafi sistemleri entegrasyonu-Ankara Örneği. Geomatik, 5(3), 193-200. https://doi.org/10.29128/geomatik.643569
3. Elhashash, M., Albanwan, H., & Qin, R. (2022). A review of mobile mapping systems: From sensors to applications. Sensors, 22(11), 4262. https://doi.org/10.3390/s22114262
4. Luo, H., Wang, C., Wen, C., Cai, Z., Chen, Z., Wang, H., ... & Li, J. (2015). Patch-based semantic labeling of road scene using colorized mobile LiDAR point clouds. IEEE Transactions on Intelligent Transportation Systems, 17(5), 1286-1297. https://doi.org/10.1109/TITS.2015.2499196
5. Yang, B., Dong, Z., Zhao, G., & Dai, W. (2015). Hierarchical extraction of urban objects from mobile laser scanning data. ISPRS Journal of Photogrammetry and Remote Sensing, 99, 45-57. https://doi.org/10.1016/j.isprsjprs.2014.10.005
6. Wen, C., Li, J., Luo, H., Yu, Y., Cai, Z., Wang, H., & Wang, C. (2015). Spatial-related traffic sign inspection for inventory purposes using mobile laser scanning data. IEEE Transactions on Intelligent Transportation Systems, 17(1), 27-37. https://doi.org/10.1109/TITS.2015.2418214
7. Wu, Y., Wang, Y., Zhang, S., & Ogai, H. (2020). Deep 3D object detection networks using LiDAR data: A review. IEEE Sensors Journal, 21(2), 1152-1171. https://doi.org/10.1109/JSEN.2020.3020626
8. Broggi, A. (1995, September). A massively parallel approach to real-time vision-based road markings detection. In Proceedings of the Intelligent Vehicles' 95, 84-89

https://doi.org/10.1109/IVS.1995.528262
9. He, Y., Wang, H., & Zhang, B. (2004). Color-based road detection in urban traffic scenes. IEEE Transactions on intelligent transportation systems, 5(4), 309-318. https://doi.org/10.1109/TITS.2004.838221
10. Veit, T., Tarel, J. P., Nicolle, P., & Charbonnier, P. (2008, October). Evaluation of road marking feature extraction. In 2008 11th International IEEE Conference on Intelligent Transportation Systems, 174-181. https://doi.org/10.1109/ITSC.2008.4732564.
11. Grejner-Brzezinska, D. A., Li, R., Haala, N., & Toth, C. (2004). From Mobile Mapping to Telegeoinformatics. Photogrammetric Engineering & Remote Sensing, 70(2), 197-210. https://doi.org/10.14358/PERS.70.2.197
12. Chen, S., Chen, F., Liu, J., Wu, J., & Bienkiewicz, B. (2010). Mobile mapping technology of wind velocity data along highway for traffic safety evaluation. Transportation research part C: emerging technologies, 18(4), 507-518. https://doi.org/10.1016/j.trc.2009.10.003
13. Li, R. (1997). Mobile mapping: An emerging technology for spatial data acquisition. Photogrammetric Engineering and Remote Sensing, 63(9), 1085-1092.
14. Poggenhans, F., Pauls, J. H., Janosovits, J., Orf, S., Naumann, M., Kuhnt, F., & Mayr, M. (2018, November). Lanelet2: A high-definition map framework for the future of automated driving. In 2018 21st international conference on intelligent transportation systems (ITSC), 1672-1679. https://doi.org/10.1109/ITSC.2018.8569929
15. Otero, R., Lagüela, S., Garrido, I., & Arias, P. (2020). Mobile indoor mapping technologies: A review. Automation in Construction, 120, 103399. https://doi.org/10.1016/j.autcon.2020.103399
16. Errandonea, I., Beltrán, S., & Arrizabalaga, S. (2020). Digital Twin for maintenance: A literature review. Computers in Industry, 123, 103316. https://doi.org/10.1016/j.compind.2020.103316
17. Yu, G., Wang, Y., Mao, Z., Hu, M., Sugumaran, V., & Wang, Y. K. (2021). A digital twin-based decision analysis framework for operation and maintenance of tunnels. Tunnelling and underground space technology, 116, 104125. https://doi.org/10.1016/j.tust.2021.104125
18. Korus, K., Salamak, M., & Winkler, J. (2023, June). Digital Twins as the Next Step in the Design and Management of Bridge Structures. In International Symposium of the International Federation for Structural Concrete (pp. 1586-1593). Cham: Springer Nature Switzerland. https://doi.org/10.1007/978-3-031-32511-3_162
19. Kaewunruen, S., Sresakoolchai, J., Ma, W., & Phil-Ebosie, O. (2021). Digital twin aided vulnerability assessment and risk-based maintenance planning of bridge infrastructures exposed to extreme conditions. Sustainability, 13(4), 2051. https://doi.org/10.3390/su13042051
20. Bosurgi, G., Celauro, C., Pellegrino, O., Rustica, N., & Giuseppe, S. (2020). The BIM (building information modeling)-based approach for road pavement maintenance. In Proceedings of the 5th International Symposium on Asphalt Pavements & Environment (APE) 5, 480-490. https://doi.org/10.1007/978-3-030-29779-4_47
21. Sairam, N., Nagarajan, S., & Ornitz, S. (2016). Development of mobile mapping system for 3D road asset inventory. Sensors, 16(3), 367. https://doi.org/10.3390/s16030367
22. Schultz, A. J. (2012). The role of GIS in asset management: Integration at the Otay Water Distict. Master's Thesis, University of Southern California, USA
23. Tao, C. V. (2000). Mobile mapping technology for road network data acquisition. Journal of Geospatial Engineering, 2(2), 1-14.
24. Fleischer, K., & Nagel, H. H. (2001, August). Machine-vision-based detection and tracking of stationary infrastructural objects beside inner-city roads. In ITSC 2001. 2001 IEEE Intelligent Transportation Systems. Proceedings (Cat. No. 01TH8585), 525-530. https://doi.org/10.1109/ITSC.2001.948713
25. Schwarz, K. P., & Li, Y. C. (1996). What can airborne gravimetry contribute to geoid determination?. Journal of Geophysical Research: Solid Earth, 101(B8), 17873-17881. https://doi.org/10.1029/96JB00819
26. Murray, S., Haughey, S., Brogan, M., Fitzgerald, C., McLoughlin, S., & Deegan, C. (2011). Mobile mapping system for the automated detection and analysis of road delineation. IET intelligent transport systems, 5(4), 221-230. https://doi.org/10.1049/iet-its.2010.0105
27. Brogan, M., McLoughlin, S., & Deegan, C. (2013). Assessment of stereo camera calibration techniques for a portable mobile mapping system. IET Computer Vision, 7(3), 209-217. https://doi.org/10.1049/iet-cvi.2012.0085
28. Glennie, C. (2007). Rigorous 3D Error Analysis of Kinematic Scanning LIDAR Systems. Journal of Applied Geodesy, 1(3), 147–157. https://doi.org/10.1515/jag.2007.017
29. Toth, C. K. (2009). R&D of Mobile LIDAR Mapping and Future Trends. American Society for Photogrammetry and Remote Sensing Annual Conference, ASPRS, 9-13.
30. Olsen, M. J., Roe, G. V., Glennie, C., Persi, F., Reedy, M., Hurwitz, D., Williams, K., Tuss, H., Squellati, A. & Knodler, M. (2013). Guidelines for the Use of Mobile LIDAR in Transportation Applications, (Vol. 748). Transportation Research Board. https://doi.org/10.13140/RG.2.1.2991.6884
31. Gan-Mor, S., Clark, R. L., & Upchurch, B. L. (2007). Implement lateral position accuracy under RTK-GPS tractor guidance. Computers and Electronics in Agriculture, 59(1-2), 31-38. https://doi.org/10.1016/j.compag.2007.04.008

Mersin Photogrammetry Journal
https://dergipark.org.tr/en/pub/mephoj
e-ISSN 2687-654X

Analysing detail preserving capabilities of bilateral, laplacian and taubin mesh filtering methods

Erkan Besdok [*1], **Pinar Civicioglu** [2]

[1]*Erciyes University, Department of Geomatics Engineering, Türkiye*
[2]*Erciyes University, Department. of Aircraft Electrics and Electronics, Türkiye*

Keywords
Mesh Filtering
Bilateral Filter
Laplacian Filter
Taubin Filter

Research Article
DOI: 10.53093/mephoj.1349021

Received:24.08.2023
Revised: 09.09.2023
Accepted:25.09.2023
Published:17.10.2023

Abstract

Mesh filtering of surfaces is crucial for noise reduction, feature preservation, and mesh simplification in graphics, visualization, and computer vision. In this paper, the detail preservation capacities of 3 frequently used filters, i.e., Bilateral, Laplacian, and Taubin mesh filters, in mesh filtering have been thoroughly examined by experiments conducted on 4 different test meshes. While the Bilateral filter excels in preserving sharp features due to its integration of geometric proximity with intensity similarity, the Laplacian filter prioritizes smoothness by averaging neighboring vertex positions, and the Taubin filter offers a balanced approach by merging attributes of both Laplacian and high-pass filters. The Bilateral filter's primary strength lies in its ability to maintain sharp features on a mesh, ensuring that intricate details are preserved by considering both the spatial closeness and intensity similarity of vertices. The Laplacian filter, although effective in achieving mesh smoothness, has the propensity to excessively smooth out sharp and defining features, potentially causing a loss of critical details in the processed mesh. The Taubin filter integrates the best of both worlds, ensuring smoothness without excessive mesh shrinkage; however, it might not excel in feature preservation as effectively as the Bilateral filter or smooth as uniformly as the Laplacian filter, making it a middle-ground option for certain applications. The statistical analysis of the experimental results has shown that the Taubin method is statistically a more successful mesh filtering method for the test sets used in this paper.

1. Introduction

Mesh surface filtering [1-7] is a pivotal process in the domain of computer graphics and computational geometry, aimed at enhancing the visual quality and computational efficiency of three-dimensional (3D) mesh models. A 3D mesh is a discrete representation of a surface composed of vertices, edges, and faces. However, due to various factors such as acquisition methods, simplification techniques, or transmission limitations, meshes often contain imperfections, noise, and artifacts that can degrade their appearance and usability. Mesh surface filtering [8-14], therefore, involves the application of algorithms to refine and improve the geometric and topological characteristics of mesh surfaces.

The rationale behind filtering mesh surfaces resides in the pursuit of producing visually pleasing and physically plausible models for applications ranging from video games and virtual reality to medical imaging and architectural design. The overarching goal is to mitigate undesired visual artifacts and irregularities that might stem from processes like 3D scanning, simplification, or transmission over networks. Filtering not only enhances the aesthetics of rendered scenes but also assists in downstream tasks such as mesh compression, collision detection, and finite element analysis.

Advantages of mesh filtering methods are manifold. Firstly, they enable noise reduction [15-21], effectively ameliorating the presence of outliers and spurious geometries that could arise from sensor inaccuracies or data corruption. Secondly, these methods can enhance mesh coherency by addressing issues like cracks and gaps between adjacent faces, thereby facilitating smoother interactions during rendering and simulation. Moreover, filtering contributes to the preservation of salient features while attenuating superfluous details, which proves invaluable in applications where

* **Corresponding Author**

*(ebesdok@erciyes.edu.tr) ORCID ID 0000-0001-9309-375X
(civici@erciyes.edu.tr) ORCID ID 0000-0003-1850-8489

Cite this article

Beşdok, E., & Civicioğlu, P. (2023). Analysing detail preserving capabilities of bilateral, laplacian and taubin mesh filtering methods. Mersin Photogrammetry Journal, 5(2), 67-74

maintaining the fidelity of critical structures is essential. Additionally, by optimizing the mesh representation [8, 22-25], computational overhead is reduced, enabling real-time rendering and interaction even in resource-constrained environments.

However, mesh filtering methods are not devoid of limitations. One notable concern is the potential loss of fine details during the filtering process, as aggressive filtering can inadvertently erase intricate features that are pertinent in certain applications. Furthermore, there is an inherent trade-off between filtering strength and computational cost; complex filtering algorithms may demand significant processing power and memory resources, impeding their applicability on low-end devices. Selecting an appropriate filtering method and parameter configuration can also be nontrivial, necessitating domain expertise and iterative refinement.

In conclusion, mesh surface filtering constitutes a vital facet of modern computer graphics, serving to enhance visual quality, alleviate artifacts, and improve computational efficiency in 3D mesh models. While its advantages encompass noise reduction, coherency enhancement, and feature preservation, caution must be exercised to mitigate potential drawbacks such as detail loss and computational overhead. The ongoing evolution of filtering techniques continues to address these challenges, contributing to the creation of compelling, high-fidelity virtual environments and simulations across diverse domains.

Mesh filtering methods [10, 26-28] have gained considerable attention due to their applications in graphics, computer vision, and geometric modelling. These methods target the removal of noise, preservation of salient features, and simplification of mesh structures. One of the early and widely-adopted techniques is Laplacian smoothing, which averages the positions of neighbouring vertices, but it often over-smooths and may degrade mesh quality. Bilateral mesh filtering [2, 5, 23, 29, 30] emerged as a promising alternative by combining geometric closeness and intensity resemblance, effectively preserving sharp features. However, its computational expense has been a limitation for real-time applications.

Taubin [31] introduced a method that leverages the combination of low-pass and high-pass filters, preventing mesh shrinkage observed in traditional Laplacian approaches. Recently, non-local means and anisotropic diffusion methods have been explored, inspired by their success in image processing. These methods consider wider neighbourhoods or adapt filtering based on local mesh properties. Guided mesh filtering, where the filter operation is guided by another signal, has also shown promising results, especially in texture and feature preservation. Wavelet-based techniques, which decompose the mesh into frequency bands, enable multi-resolution processing and have applications in mesh compression.

Deep learning-based mesh filtering [32, 33], a burgeoning area, employs neural networks to learn optimal filtering parameters from data. While traditional methods rely on hand-crafted heuristics, these learnable filters adapt based on the input, making them versatile. In conclusion, mesh filtering remains an active research domain with methodologies ranging from classical algorithms to modern machine learning approaches, each with its own merits and challenges.

Bilateral mesh filtering maintains sharp features by weighing both geometric proximity and feature similarity, making it particularly suitable for preserving edges but can be computationally intensive. On the other hand, Laplacian filtering smoothens the surface by averaging neighbouring vertices, which can lead to over-smoothing of sharp details if not controlled properly. In contrast, Taubin filtering employs a sequence of low-pass and high-pass filters, ensuring effective smoothing without causing the mesh to shrink, offering a balance between detail preservation and noise reduction.

This paper presents experiments on the use of Bilateral, Laplacian, and Taubin mesh filters in photogrammetry and computer vision. These filters are commonly used in these fields because they are effective at smoothing meshes while preserving sharp features.

The rest of this paper is organized as follows: Section 2 introduces Mesh Filtering Methods. In Section 3, Experiments are presented. In Section 4, Results and Conclusions are given.

2. Mesh Filtering Methods

This section briefly presents the analytical structures, basic features, advantages, and disadvantages of the Bilateral, Laplacian, and Taubin filters used in the Experiments section of this paper.

2.1. Bilateral Mesh Filtering

Bilateral mesh filtering is a method that applies Bilateral filtering principles to 3D mesh data. It aims to smooth the mesh while preserving important features such as edges and corners. The filtering process takes into account both geometric distance and attribute similarity between vertices to determine the filtering weights.

Given a mesh with vertices V and faces F, the filtered position p_i, for vertex p_i can be computed using Equation 1:

$$p_{i'} = \frac{1}{W_i} \sum_{j=1}^{N} w_{ij} \cdot p_j \tag{1}$$

where, N is the number of neighboring vertices of p_i. The p_j represents the neighboring vertex positions. The w_{ij} is the Bilateral weight between vertices p_i and p_j. w_{ij} *is* the normalization term. The w_{ij} is computed as a combination of spatial and range weights by using Equation 2:

$$w_{ij} = w_s(\|p_i - p_j\|) \cdot w_r(p_i, p_j) \tag{2}$$

where, $w_s(\|p_i - p_j\|)$ is the spatial weight based on the geometric distance between vertices p_i and p_j. The $w_r(p_i, p_j)$ is the range weight based on attribute similarity between vertices p_i and p_j. In this filter, $w_s(\|p_i - p_j\|)$ and $w_r(p_i, p_j)$ represent the spatial and range weights, respectively. Bilateral mesh filter iterates

over each vertex in the mesh, computes the weighted sum of neighboring vertex positions, and updates the filtered position accordingly while considering normalization. Pseudo-code of Bilateral mesh filter is given in Figure 1.

Data: Input mesh with vertices V and faces F
Result: Filtered mesh vertices V'
foreach *vertex* $p_i \in V$ **do**
  Initialize filtered position $p'_i = (0, 0, 0)$;
  Initialize normalization term $W_i = 0$;
  foreach *neighboring vertex* p_j *of* p_i **do**
    Calculate spatial weight $w_{\text{spatial}} = w_s(\|p_i - p_j\|)$;
    Calculate range weight $w_{\text{range}} = w_r(p_i, p_j)$;
    Calculate bilateral weight $w_{ij} = w_{\text{spatial}} \cdot w_{\text{range}}$;
    Update filtered position $p'_i = p'_i + w_{ij} \cdot p_j$;
    Update normalization term $W_i = W_i + w_{ij}$;
  Update filtered position $p'_i = \frac{p'_i}{W_i}$;

Figure 1. Pseudo-code of Bilateral mesh filter.

Bilateral mesh filter offers several advantages that make it a valuable technique for enhancing the visual quality and preserving important features of 3D mesh models:

Bilateral filtering is inherently designed to preserve edges and boundaries within the data. This characteristic is crucial for maintaining the sharpness and integrity of important features in the mesh, such as edges, corners, and creases. Unlike traditional smoothing methods that tend to blur edges, bilateral filtering ensures that these features remain well-defined. One of the strengths of bilateral mesh filtering lies in its ability to take into account attributes associated with vertices, such as normal or colours. This enables the filtering process to consider not only geometric proximity but also attribute similarity when computing filtering weights. As a result, attributes are preserved more effectively, contributing to the overall visual fidelity of the mesh. Bilateral filtering effectively reduces noise and small-scale irregularities present in the mesh data. The incorporation of attribute-based filtering helps distinguish between meaningful variations and noise, allowing the method to selectively smooth out noise while retaining genuine geometric and attribute details.

Bilateral filtering is highly adaptable and can be tailored to specific applications and requirements. By adjusting the parameters of the spatial and range weights, users can control the strength of the filtering effect. This adaptability makes bilateral filtering suitable for a wide range of scenarios, from artistic stylization to scientific simulations. Unlike some traditional smoothing methods that may result in blurring and distortion of geometric details, bilateral filtering smooths the mesh while preserving important features. This is particularly advantageous for applications where maintaining the integrity of the mesh's structural characteristics is essential.

Bilateral filtering strikes a balance between noise reduction and feature preservation. It selectively smooths areas that are less critical while leaving important features untouched. This characteristic is particularly valuable for applications where a compromise between overall smoothness and the preservation of key details is required.

The advantages of bilateral mesh filtering extend across various domains, including computer graphics, medical imaging, computer-aided design, and more. It finds applications in rendering, modelling, simulation, and analysis, making it a versatile technique with wide-ranging benefits. While more computationally intensive methods may achieve better results, bilateral filtering strikes a good balance between quality and efficiency. It is often suitable for real-time or interactive applications, offering an effective compromise between filtering strength and computational complexity.

In summary, bilateral mesh filtering is advantageous due to its ability to preserve edges, accommodate attribute-based filtering, reduce noise, offer customizable adjustments, and strike a balance between feature preservation and smoothing. These advantages make it a valuable tool for enhancing the visual quality and fidelity of 3D mesh models across diverse applications.

2.2. Laplacian Mesh Filtering

Laplacian Mesh Filtering is a widely used method for mesh smoothing and denoising. It leverages the Laplacian operator to iteratively update vertex positions based on the local geometric information of neighbouring vertices.

The Laplacian operator quantifies the difference between a vertex and the average of its neighbours, capturing the curvature and shape characteristics of the mesh. Let's denote the Laplacian operator as Δ and the position of a vertex v_i as $\boldsymbol{p}_i = (x_i, y_i, z_i)$. The Laplacian operator applied to the position of a vertex is defined in Equation 3:

$$\Delta \boldsymbol{p}_i = \frac{1}{|\mathcal{N}_i|} \sum_{v_j \in \mathcal{N}_i} (\boldsymbol{p}_j - \boldsymbol{p}_i) \tag{3}$$

where $\mathcal{N}_i$ represents the set of neighboring vertices of v_i.

The basic outline of the Laplacian Mesh Filtering algorithm is given below:

1. Initialize: Given a mesh with vertices $\boldsymbol{p}_i$ and connectivity information.
2. Choose the number of iterations N.
3. For k = 1 to N:
   a. For each vertex v_i:
      i. Compute the Laplacian update: $\Delta \boldsymbol{p}_i = \frac{1}{|\mathcal{N}_i|} \sum_{v_j \in \mathcal{N}_i} (\boldsymbol{p}_j - \boldsymbol{p}_i)$.
      ii. Update the vertex position: $\boldsymbol{p}_i^{(k)} = \boldsymbol{p}_i^{(k-1)} + \lambda \cdot \Delta \boldsymbol{p}_i$,

where λ is a user-defined weight controlling the step size.

The Pseudo-code of Laplacian mesh filtering is given in Figure 2.

In this pseudo-code, $\boldsymbol{p}_i^{(k)}$ represents the position of vertex v_i after k iterations.

Laplacian Mesh Filtering iteratively adjusts vertex positions, redistributing their positions based on the average displacement of neighbouring vertices. This

process tends to smooth out noise and small-scale irregularities in the mesh while preserving overall shape characteristics. The parameter λ controls the extent of the update and should be chosen carefully to achieve the desired smoothing effect without causing over-smoothing or distortion.

Input: Mesh vertices $\{\mathbf{p}_i\}$, Connectivity information $\{\mathcal{N}_i\}$, Number of iterations N, Weight λ
Output: Smoothed mesh vertices
for $k = 1$ *to* N **do**
  for *each vertex* v_i **do**
    Compute Laplacian update: $\Delta\mathbf{p}_i = \frac{1}{|\mathcal{N}_i|}\sum_{v_j \in \mathcal{N}_i}(\mathbf{p}_j - \mathbf{p}_i)$;
    Update vertex position: $\mathbf{p}_i^{(k)} = \mathbf{p}_i^{(k-1)} + \lambda \cdot \Delta\mathbf{p}_i$;

Figure 2. Pseudo-code of Laplacian mesh filtering.

The Laplacian Mesh Filtering method is conceptually straightforward and easy to implement. It involves a simple iterative process that updates vertex positions based on the Laplacian operator, making it accessible to both novice and experienced users.

Laplacian filtering tends to preserve local geometric coherence. It smooths the mesh while maintaining the overall shape characteristics and connectivity of the original mesh. This makes it suitable for applications where preserving essential features is important.

Laplacian filtering is effective in reducing noise and small-scale irregularities in the mesh. By averaging vertex positions with their neighbours, the method can mitigate high-frequency noise that might be present due to data acquisition or other factors. The filtering strength can be controlled using the parameter λ. Users can adjust this parameter to achieve the desired level of smoothing. This level of control is valuable when adapting the filtering to different meshes and requirements.

While Laplacian filtering is efficient at smoothing, it can inadvertently lead to detail loss, particularly in regions with high curvature or intricate features. The iterative nature of the algorithm tends to distribute vertex positions toward an average, potentially diminishing fine details. In some cases, Laplacian filtering can introduce shape distortion, especially when the smoothing process is too aggressive. This might cause unintended changes in the mesh's shape that could impact the overall visual quality or intended characteristics of the model.

Laplacian filtering can lead to uneven smoothing, where some parts of the mesh are smoothed more than others. This is due to the reliance on local neighbourhood information, which might not be uniform across the entire mesh. The performance of Laplacian filtering is highly dependent on the choice of the λ parameter. Selecting an inappropriate value can lead to suboptimal results, such as under-smoothing or over-smoothing. In meshes with irregular connectivity or boundary conditions, Laplacian filtering can sometimes introduce artifacts like shrinkage or expansion of specific regions. This is because the filtering process is sensitive to the local vertex distribution and connectivity.

In summary, Laplacian Mesh Filtering offers a straightforward approach to mesh smoothing with advantages including simplicity, noise reduction, and local coherence. However, it comes with the trade-offs of potential detail loss, shape distortion, and sensitivity to parameter choices. Users should carefully consider these factors and their specific application requirements when choosing Laplacian filtering as a mesh enhancement technique.

2.3. Taubin Mesh Filtering

Taubin Mesh Filtering is a popular method for smoothing and denoising 3D mesh surfaces. It was introduced by Gabriel Taubin in 1995 as an iterative technique that alternates between applying two distinct filters: a Laplacian smoothing filter and a high-pass filter. This approach effectively reduces noise while preserving important features of the mesh.

Given a 3D mesh represented by vertices ($\boldsymbol{v}_i$) and faces ($\boldsymbol{f}_j$) with associated normal ($\boldsymbol{n}_i$), the Laplacian smoothing step can be represented by using Equation 4:

$$\boldsymbol{v}_i^{(k+1)} = \boldsymbol{v}_i^{(k)} + \lambda_1 \cdot \text{Laplacian}(\mathbf{v}_i^{(k)}) \qquad (4)$$

where (λ_1) is a user-defined parameter controlling the amount of smoothing, and Laplacian($\mathbf{v}_i^{(k)}$) computes the Laplacian operator on vertex ($\boldsymbol{v}_i$) at iteration (k).

The Laplacian operator measures the difference between the vertex and the average of its neighbouring vertices, thus smoothing out irregularities. Following the Laplacian smoothing, the high-pass filter step is applied using Equation 5:

$$\boldsymbol{v}_i^{(k+1)} = \boldsymbol{v}_i^{(k+1)} - \lambda_2 \cdot \text{Laplacian}(\mathbf{v}_i^{(k+1)}) \qquad (5)$$

Here, (λ_2) is another user-defined parameter controlling the amount of high-frequency detail preservation. This step effectively compensates for the excessive smoothing introduced by the previous step, enhancing the overall fidelity of the filtered mesh.

The pseudo-code of Taubin Mesh Filtering method is given in Figure 3.

Input : 3D Mesh with vertices $\mathbf{V}$, faces $\mathbf{F}$, normals $\mathbf{N}$, smoothing parameters λ_1 and λ_2, number of iterations K
Output: Filtered mesh vertices $\mathbf{V}$
for $k \leftarrow 1$ **to** K **do**
  for $i \leftarrow 1$ to *num_vertices*($\mathbf{V}$) **do**
    $\mathbf{L}_i \leftarrow \text{ComputeLaplacian}(\mathbf{V}, \mathbf{F}, \mathbf{N}, i)$; // Laplacian operator
    $\mathbf{V}[i] \leftarrow \mathbf{V}[i] + \lambda_1 \cdot \mathbf{L}_i$; // Laplacian smoothing
  for $i \leftarrow 1$ to *num_vertices*($\mathbf{V}$) **do**
    $\mathbf{L}_i \leftarrow \text{ComputeLaplacian}(\mathbf{V}, \mathbf{F}, \mathbf{N}, i)$; // Laplacian operator
    $\mathbf{V}[i] \leftarrow \mathbf{V}[i] - \lambda_2 \cdot \mathbf{L}_i$; // High-pass filtering
return $\mathbf{V}$

Figure 3. Pseudo-code of Taubin mesh filtering.

This pseudo-code outlines the core steps of the Taubin Mesh Filtering method, including Laplacian computation and the iterative application of smoothing and high-pass filtering. The parameters (λ_1), (λ_2), and the number of iterations (K) can be adjusted to achieve the desired level of smoothing and detail preservation for a given mesh.

The Taubin Mesh Filtering method offers several advantages and drawbacks, making it an interesting choice for mesh smoothing and denoising in certain scenarios.

Taubin Mesh Filtering employs an iterative process that alternates between Laplacian smoothing and high-

pass filtering. This approach allows for controlled smoothing while preserving important geometric details. The iterative nature enables users to fine-tune the degree of filtering. The method is effective in reducing noise and artifacts present in mesh data.

The Laplacian smoothing step averages vertex positions, which helps in attenuating high-frequency noise components, resulting in a smoother appearance. The high pass filtering step counteracts excessive smoothing introduced by the Laplacian operation. This ensures that significant geometric features, such as edges and corners, are better preserved compared to methods that solely rely on simple smoothing techniques. The user has control over two crucial parameters: (λ_1) and (λ_2). These parameters influence the amount of smoothing and detail preservation, allowing users to tailor the filtering process to suit the specific characteristics of the input mesh and the desired visual outcome. The method is relatively computationally efficient due to its localized nature. The Laplacian and high pass filtering operations involve neighbouring vertices, making them amenable to parallelization and optimization techniques.

Depending on the chosen parameter values and the number of iterations, aggressive smoothing may result in the loss of fine geometric details. While the high pass filter aims to mitigate this, there can still be instances where essential details are inadvertently smoothed out.

The effectiveness of the Taubin method is closely tied to parameter settings. Selecting appropriate values for (λ_1) and (λ_2) is not always straightforward, and finding the right balance between smoothing and preserving details requires experimentation. In certain cases, excessive filtering iterations can lead to mesh distortion. Particularly, regions with high curvature might exhibit undesirable artifacts due to the iterative nature of the smoothing process.

The Taubin method's effectiveness diminishes in cases where the input mesh has highly irregular or noisy features. For instance, when the noise levels are extremely high or the mesh lacks clear geometric structure, the method might struggle to achieve satisfactory results. Despite its advantages, Taubin Mesh Filtering may necessitate manual intervention to achieve optimal results. Users might need to fine-tune parameters and conduct iterative trials to strike a balance between smoothing and feature preservation.

In conclusion, the Taubin Mesh Filtering method is a versatile approach for smoothing and denoising 3D mesh surfaces. Its iterative nature and parameter control offer flexibility in achieving varying degrees of noise reduction and detail preservation. However, careful consideration of parameter settings and an understanding of its limitations are essential to ensure effective application and avoid unintended consequences such as detail loss or mesh distortion.

3. Experiments

In the experiments, 4 different meshes were used: “David” (Figure 4A), “Roma” (Figure 4B), “Man” (Figure 5A), and “Girl” (Figure 5B).

The “David” test mesh has 72,685 faces, and 36,714 vertices. The “Roma” test mesh consists of 55,847 faces, and 28,254 vertices. The “Man” test mesh contains 30,000 faces, and 15,258 vertices. The “Girl” test mesh has 6,999 faces, and 3,658 vertices. The spatial coordinates of the related mesh’s are given in centimetre. The spatial boundaries for the "Man" are given as: $150 \leq x \leq 200,\ 3.77 \leq y \leq 43.32,\ and\ 2.23 \leq z \leq 67.39$. The spatial boundaries for the "Roma" are given as: $100 \leq x \leq 200,\ 110.31 \leq y \leq 165.95,\ and\ 204.33 \leq z \leq 295.11$. The spatial boundaries for the "David" are given as: $100 \leq x \leq 200,\ 75 \leq y \leq 150,\ 100 \leq z \leq 200$. The spatial boundaries for the "Girl" are given as: $100 \leq x \leq 200,\ 84.14 \leq y \leq 170.63,\ and\ 56.29 \leq z \leq 210.63$.

Corrupted meshes are generated by adding random valued uniform impulsive noise to the vertex positions of the original meshes. The vertex positions of the generated corrupted meshes are repaired by optimizing the internal parameters of the filters used in the experiments.

The optimal values for the related threshold parameters of Bilateral, Laplacian, and Taubin filters have been optimized using the BSA algorithm [34-37]. Taubin filter is applied to related meshes using 5 iterations. BSA is a very powerful, non-recursive, iterative evolutionary search method developed by Çivicioğlu [34]. Evolutionary search algorithms are very popular because they produce useful results in the optimization of non-differentiable, multimodal, and continuous numerical problems. For BSA, the size of the population is set to 20, and the maximum number of iterations is empirically chosen as 100,000. The search space lower and upper bound values have been determined as [low=0; up=1] only for the first iteration. In the following iterations, BSA employed the unbounded search method to obtain the optimum values for the related filters.

The objective function used for BSA is given in Equation 6:

$$\underbrace{argmin}_{parameters\ of\ Filter} \Sigma|CMesh_{Filter} - OMesh| \qquad (6)$$

where $CMesh_{Filter}$, and $OMesh$ denote response of the filter used in the current experiment, and original mesh, respectively.

All the filtering methods used in the Experiments were implemented in MATLAB. The Experiments were conducted by using a computer with Intel(R) Xeon(R) CPU E5-2650 v2 @ 2.60GHz 2.60 GHz (2 CPU), 64GB RAM.

Table 1 shows the ‘Mean Square Error’’ values calculated between the meshes obtained from the experiments and the original mesh. When Table 1 is examined, it is seen that the Taubin method is relatively more successful in filtering out the relevant data.

Table 1. ‘Mean Square Error’ values computed between filtered and original mesh.

Test Set	Noisy	Filtering Methods		
		Bilateral Filer	Laplacian	Taubin
David	0.0837	0.0417	0.0215	0.0108
Roma	0.0954	0.0567	0.0349	0.0181
Man	0.1054	0.0600	0.0381	0.0270
Girl	0.0910	0.0580	0.0276	0.0198

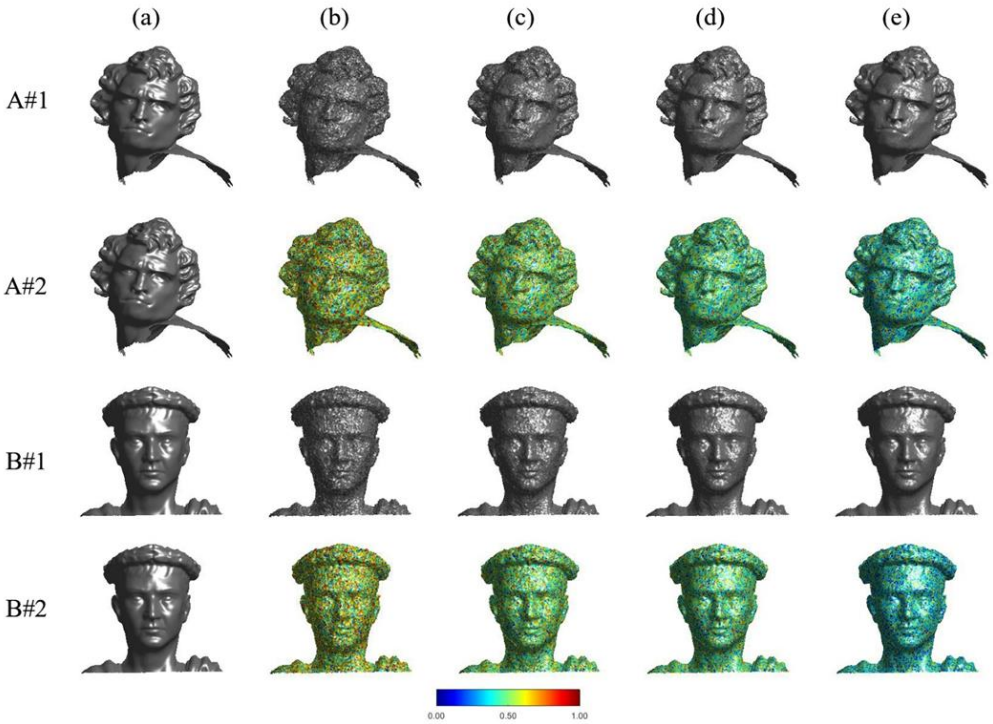

Figure 4. The mesh surface without texture for (a) Original, (b) Corrupted, (c) Bilateral Filtering, (d) Laplacian, and (e) Taubin are illustrated in rows A#1, and B#1. The normalized- displacement values superimposed on the related mesh surfaces as texture for (b) Corrupted, (c) Bilateral Filtering, (d) Laplacian, and (e) Taubin are illustrated in rows A#2, and B#2.

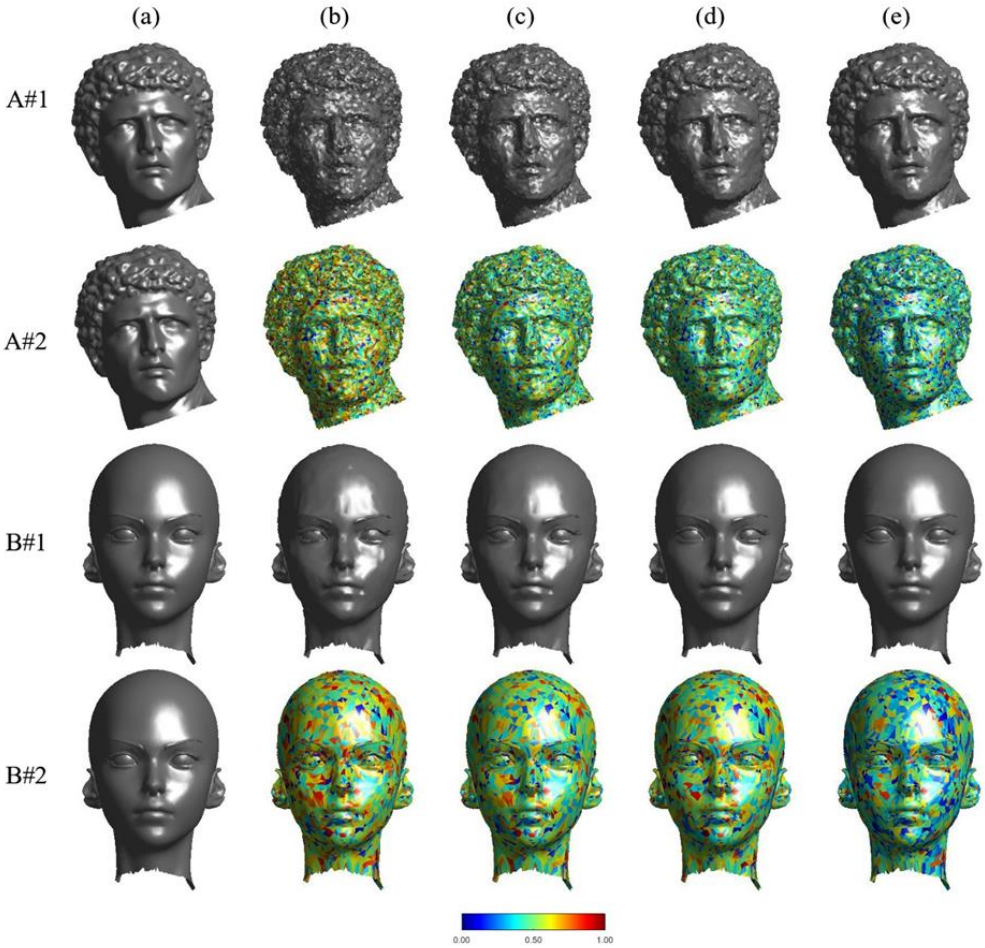

Figure 5. The mesh surface without texture for (a) Original, (b) Corrupted, (c) Bilateral Filtering, (d) Laplacian, and (e) Taubin are illustrated in rows C#1, and D#1. The normalized-displacement values superimposed on the related mesh surfaces as texture for (b) Corrupted, (c) Bilateral Filtering, (d) Laplacian, and (e) Taubin are illustrated in rows C#2, and D#2.

The meshes produced by the relevant filters at the end of the experiments are shown in Figure 4 and Figure 5. Column (a) of Figure 4 and Figure 5 shows the original mesh surface. Column (b) of Figure 4 and Figure 5 shows the corrupted mesh with random valued uniform impulsive noise, where noise ~ **U** [- 0.50; 0.50] as cm., and **U** denotes continuous uniform distribution.

4. Results and Conclusion

In this paper, the detail preservation capabilities of Bilateral, Laplacian, and Taubin mesh filtering methods have been examined in detail using 4 test sets. The Bilateral filter has a relatively more complex analytical structure compared to the Laplacian, and Taubin filters. Taubin filtering is relatively more successful in preventing deformation on the mesh. In concave and convex areas, Laplacian, and Taubin tend to preserve mesh details relatively better. The Bilateral filter causes a partial over-smoothing effect on the edge areas. In contrast, visually, the Bilateral filter tends to produce more continuous surface data. The Laplacian method has caused a partial over-sharp effect on the edge areas. Although the results obtained from the study suggest that the success of the mesh filter is somewhat data-dependent, it has been observed that the Taubin method is more successful in detail preservation compared to other methods used in the experiments.

Author contributions

Erkan Beşdok: Data curation, Software, Validation. **Pınar Çivicioğlu:** Conceptualization, Methodology, Software, Writing, Editing

Conflicts of interest

The authors declare no conflicts of interest.

References

1. Liu, Y., Coombes, M., & Liu, C. (2023). Mesh-based consensus distributed particle filtering for sensor networks. IEEE Transactions on Signal and Information Processing over Networks, 9, 346-356. https://doi.org/10.1109/TSIPN.2023.3278469
2. Liu, B., Li, B., Cao, J., Wang, W., & Liu, X. (2023). Adaptive and propagated mesh filtering. Computer-Aided Design, 154, 103422. https://doi.org/10.1016/j.cad.2022.103422
3. Fábián, G. (2023). Generalized Savitzky–Golay filter for smoothing triangular meshes. Computer Aided Geometric Design, 100, 102167. https://doi.org/10.1016/j.cagd.2022.102167
4. Han, H. D., & Han, J. K. (2022). Modified bilateral filter for feature enhancement in mesh denoising. IEEE Access, 10, 56845-56862. https://doi.org/10.1109/ACCESS.2022.3176961
5. Zhong, S., Song, Z., Liu, Z., Xie, Z., Chen, J., Liu, L., & Chen, R. (2021). Shape-aware mesh normal filtering. Computer-Aided Design, 140, 103088. https://doi.org/10.1016/j.cad.2021.103088
6. Zhao, W., Liu, X., Wang, S., Fan, X., & Zhao, D. (2019). Graph-based feature-preserving mesh normal filtering. IEEE Transactions on Visualization and Computer Graphics, 27(3), 1937-1952. https://do.iorg/10.1109/TVCG.2019.2944357
7. Zhang, J., Deng, B., Hong, Y., Peng, Y., Qin, W., & Liu, L. (2018). Static/dynamic filtering for mesh geometry. IEEE transactions on visualization and computer graphics, 25(4), 1774-1787. https://do.org/10.1109/TVCG.2018.2816926
8. Noel, G., Djouani, K., Van Wyk, B., & Hamam, Y. (2012). Bilateral mesh filtering. Pattern Recognition Letters, 33(9), 1101-1107. https://doi.org/10.1016/j.patrec.2012.02.008
9. Loménie, N., & Stamon, G. (2008). Morphological mesh filtering and α-objects. Pattern Recognition Letters, 29(10), 1571-1579. https://doi.org/10.1016/j.patrec.2008.03.019
10. Kim, B., & Rossignac, J. (2005). Geofilter: Geometric selection of mesh filter parameters. In Computer Graphics Forum, 24(3), 295-302.
11. Leipoldt, K. J., Happich, T., Kreysa, E., & Gemünd, H. P. (1991). Scattering matrix methods for far-infrared metal mesh filters. International Journal of Infrared and Millimeter Waves, 12, 263-274. https://doi.org/10.1007/BF01010300
12. Chen, P. A. (1987). The performance of dielectric coated mesh filter. International Journal of Infrared and Millimeter Waves, 8, 29-33. https://doi.org/10.1007/BF01010643
13. Byrne, D. M., Brouns, A. J., Case, F. C., Tiberio, R. C., Whitehead, B. L., & Wolf, E. D. (1985). Infrared mesh filters fabricated by electron-beam lithography. Journal of Vacuum Science & Technology B: Microelectronics Processing and Phenomena, 3(1), 268-271. https://doi.org/10.1116/1.583243
14. Byrne, D. M., Brouns, A. J., & Case, F. C. (1984). Infrared mesh filters (A). Journal of the Optical Society of America A, 1, 1330.
15. Civicioglu, P. (2009). Removal of random-valued impulsive noise from corrupted images. IEEE Transactions on Consumer Electronics, 55(4), 2097-2104. https://do.org/10.1109/TCE.2009.5373774
16. Civicioglu, P. (2007). Using uncorrupted neighborhoods of the pixels for impulsive noise suppression with ANFIS. IEEE Transactions on Image Processing, 16(3), 759-773. https://doi.org/10.1109/TIP.2007.891067
17. Çivicioğlu, P. (2005). Using LM artificial neural networks and η-closest-pixels for impulsive noise suppression from highly corrupted images. In International Symposium on Neural Networks (pp. 679-684). https://doi.org/10.1007/11427445_110
18. Beşdok, E., Çivicioğlu, P., & Alçı, M. (2005). Using Anfis with circular polygons for impulsive noise suppression from highly distorted images. AEU-International Journal of Electronics and Communications, 59(4), 213-221. https://doi.org/10.1016/j.aeue.2004.11.041

19. Çivicioğlu, P., Alçı, M., & Beşdok, E. (2004). Using an exact radial basis function artificial neural network for impulsive noise suppression from highly distorted image databases. In International Conference on Advances in Information Systems, 383-391. https://doi.org/10.1007/978-3-540-30198-1_39
20. Çivicioğlu, P., Alçı, M., & Beşdok, E. (2004). Impulsive noise suppression from images with the noise exclusive filter. EURASIP Journal on Advances in Signal Processing, 16, 2434–2440. https://doi.org/10.1155/S1110865704403151
21. Çivicioğlu, P., & Alçı, M. (2004). Edge detection of highly distorted images suffering from impulsive noise. AEU-International Journal of Electronics and Communications, 58(6), 413-419. https://doi.org/10.1078/1434-8411-54100262
22. Liu, B., Cao, J., Wang, W., Ma, N., Li, B., Liu, L., & Liu, X. (2018). Propagated mesh normal filtering. Computers & Graphics, 74, 119-125. https://doi.org/10.1016/j.cag.2018.05.003
23. Zhang, W., Deng, B., Zhang, J., Bouaziz, S., & Liu, L. (2015). Guided mesh normal filtering. In Computer Graphics Forum, 34(7), 23-34. https://doi.org/10.1111/cgf.12742
24. Wei, M., Yu, J., Pang, W. M., Wang, J., Qin, J., Liu, L., & Heng, P. A. (2014). Bi-normal filtering for mesh denoising. IEEE Transactions on Visualization and Computer Graphics, 21(1), 43-55. https://doi.org/10.1109/TVCG.2014.2326872
25. Shen, J. G., Zhang, S. Y., Chen, Z. Y., Zhang, Y., & Ye, X. Z. (2009). Mesh sharpening via normal filtering. Journal of Zhejiang University-Science A, 10(4), 546-553. https://doi.org/10.1631/jzus.A0820505
26. Mao, Z., Ma, L., Zhao, M., & Xiao, X. (2006). SUSAN structure preserving filtering for mesh denoising. The Visual Computer, 22, 276-284. https://doi.org/10.1007/s00371-006-0005-7
27. Hou, Q., Bai, L., & Wang, Y. (2005). Mesh smoothing via adaptive bilateral filtering. In International Conference on Computational Science, 273-280. https://doi.org/10.1007/11428848_34
28. Balan, R., & Taubin, G. (2000). 3d mesh geometry filtering algorithms for progressive transmission schemes. Computer-aided design, 32(13), 825-846. https://doi.org/10.1016/S0010-4485(00)00069-5
29. Liu, S., Rho, S., Wang, R., & Jiang, F. (2018). Feature-preserving mesh denoising based on guided normal filtering. Multimedia Tools and Applications, 77, 23009-23021. https://doi.org/10.1007/s11042-018-5735-9
30. Zheng, Y., Fu, H., Au, O. K. C., & Tai, C. L. (2010). Bilateral normal filtering for mesh denoising. IEEE Transactions on Visualization and Computer Graphics, 17(10), 1521-1530. https://doi.org/10.1109/TVCG.2010.264
31. Agathos, A., Azariadis, P., & Kyratzi, S. (2022). Elliptic Gabriel Taubin smoothing of point clouds. Computers & Graphics, 106, 20-32. https://doi.org/10.1016/j.cag.2022.05.009
32. Nousias, S., Arvanitis, G., Lalos, A. S., & Moustakas, K. (2020). Fast mesh denoising with data driven normal filtering using deep variational autoencoders. IEEE Transactions on Industrial Informatics, 17(2), 980-990. https://doi.org/10.1109/TII.2020.3000491
33. Li, X., Li, R., Zhu, L., Fu, C. W., & Heng, P. A. (2020). DNF-Net: A deep normal filtering network for mesh denoising. IEEE Transactions on Visualization and Computer Graphics, 27(10), 4060-4072. https://doi.org/10.1109/TVCG.2020.3001681
34. Civicioglu, P. (2013). Backtracking search optimization algorithm for numerical optimization problems. Applied Mathematics and computation, 219(15), 8121-8144. https://doi.org/10.1016/j.amc.2013.02.017
35. Civicioglu, P., & Besdok, E. (2019). Bernstain-search differential evolution algorithm for numerical function optimization. Expert Systems with Applications, 138, 112831. https://doi.org/10.1016/j.eswa.2019.112831
36. Civicioglu, P., & Besdok, E. (2023). Bernstein-Levy differential evolution algorithm for numerical function optimization. Neural Computing and Applications, 35(9), 6603-6621. https://doi.org/10.1007/s00521-022-08013-7
37. Civicioglu, P., Besdok, E., Gunen, M. A., & Atasever, U. H. (2020). Weighted differential evolution algorithm for numerical function optimization: a comparative study with cuckoo search, artificial bee colony, adaptive differential evolution, and backtracking search optimization algorithms. Neural Computing and Applications, 32, 3923-3937. https://doi.org/10.1007/s00521-018-3822-5

Mersin Photogrammetry Journal
https://dergipark.org.tr/en/pub/mephoj
e-ISSN 2687-654X

Assessing road roughness using UAV-derived dense point clouds

Nizar Polat [1], **Şeyma Akça** [*1]

[1]*Harran University, Department of Geomatics Engineering, Türkiye*

Keywords
UAV
S*f*M
Point cloud
Road infrastructure
Roughness

Research Article
DOI:10.53093/mephoj.1358902

Received:12.09.2023
Revised: 10.10.2023
Accepted:13.10.2023
Published:17.10.2023

Abstract

The quality and safety of road networks are of paramount importance in modern transportation infrastructure. Road surface conditions, particularly road roughness, significantly impact vehicular travel safety, user comfort, vehicle operating costs, and overall road infrastructure maintenance. Traditional methods for road roughness analysis, such as manual inspections or image annotation, often present limitations in terms of data completeness, efficiency, and cost-effectiveness, especially for extensive road networks. This study investigates the potential of Unmanned Aerial Vehicles (UAVs) equipped with Structure-from-Motion (S*f*M) derived point clouds to transform road roughness assessment. By leveraging the capabilities of UAVs, including rapid data acquisition and high-resolution imagery, and employing S*f*M to generate detailed point clouds, this research aims to provide a comprehensive analysis of road surface conditions. The study, conducted on a road segment within the Harran University Osmanbey campus, systematically examines road roughness at different kernel sizes: 30 cm (*smaller*), 50 cm (*moderate*), and 75 cm (*larger).* Through this investigation, insights are gained into how different scales of analysis influence roughness measurements. The findings highlight the potential of UAV-derived point clouds as a promising avenue for road roughness analysis, offering transportation authorities and road administrators an efficient and cost-effective means of maintaining and enhancing road networks. The integration of this technology could lead to the development of safer, more efficient, and economically sustainable road transportation systems, benefiting both road users and infrastructure managers. As research and technological advancements in UAV-based road roughness assessment continue to progress, the potential for revolutionizing road management practices becomes increasingly apparent, ultimately leading to improved road quality and enhanced travel experiences for road users.

1. Introduction

The quality and safety of road networks are paramount concerns in modern transportation infrastructure [1]. The condition of road surfaces, particularly their roughness, plays a pivotal role in ensuring safe and efficient travel for road users [2, 3]. Road roughness not only affects the comfort and safety of vehicular travel but also impacts vehicle operating costs, fuel consumption, and overall road infrastructure maintenance [4]. Therefore, precise and comprehensive assessment of road roughness is essential for transportation authorities and road management agencies [1].

One of the key metrics used for road roughness assessment is the International Roughness Index [IRI], which quantifies the deviations or irregularities in the road's longitudinal profile [1, 6]. These irregularities are closely linked to ride quality, vehicle safety, and overall road network efficiency. By incorporating IRI into road roughness analysis, transportation authorities can gain valuable insights into road conditions and prioritize maintenance and repair efforts effectively. Traditionally, road roughness analysis has relied on manual inspections or the digital annotation of images captured along road corridors [6, 7]. While these methods have provided valuable insights, they often present limitations in terms of data completeness, efficiency, and cost-

* **Corresponding Author**
(nizarpolat@harran.edu.tr) ORCID ID 0000 – 0002 – 6061– 7796
*(seymakca@harran.edu.tr) ORCID ID 0000 – 0002 – 7888 – 2020

Cite this article
Polat, N., & Akça, Ş. (2023). Assessing road roughness using UAV-derived dense point clouds. Mersin Photogrammetry Journal, 5(2), 75-81

effectiveness, particularly when dealing with extensive road networks. To address these challenges and enhance the accuracy of road roughness assessment, recent advancements in remote sensing technologies, particularly those involving Unmanned Aerial Vehicles (UAV*s*), have opened up new avenues for data acquisition and analysis [8, 9].

Unmanned Aerial Vehicles, equipped with cameras, have the capability to rapidly capture detailed and high-resolution aerial photographs. These images, when processed using the Structure-from-Motion (S*f*M) method to generate point clouds, offer a wealth of information about the road's geometry, surface conditions, and roughness [10]. As such, UAV-based point clouds derived from aerial photographs present an enticing opportunity for road roughness analysis, offering distinct advantages in terms of speed, cost-efficiency, and data coverage [11].

This study, carried out on a road within the Harran University Osmanbey campus, focuses on the utilization of point clouds generated using the S*f*M method from aerial photographs collected by UAV to conduct a comprehensive analysis of road roughness. By leveraging the advantages of UAV technology, the S*f*M method, and advanced point cloud analysis techniques, this research endeavors to develop an accurate and efficient methodology for characterizing road roughness conditions. The primary objective is to investigate the feasibility of UAV-derived point clouds, including the IRI metric, as a valuable resource for road management and maintenance, with an emphasis on enhancing road safety, optimizing maintenance schedules, and minimizing operational costs.

Through the integration of UAV technology, the S*f*M method, and advanced point cloud analysis techniques, this study aims to contribute to the field of transportation infrastructure management. By exploring the potential of S*f*M-derived point clouds, it seeks to provide transportation authorities and road administrators with a practical and cost-effective solution for maintaining and improving the quality of road networks. Ultimately, this research endeavors to foster safer, more efficient, and economically sustainable road transportation systems.

2. Method

In this section, we outline the methodology employed for the generation of point clouds using the S*f*M approach from aerial photographs collected by the UAV and subsequent roughness analysis. We describe the steps involved in S*f*M-based point cloud generation, followed by the specific procedures for assessing road roughness using different kernel sizes.

2.1. S*f*M based point cloud generation

UAVs have revolutionized the field of remote sensing by providing a versatile platform for collecting high-resolution aerial images [12]. The methodology employed in this study harnessed the S*f*M approach for extracting point cloud data from the aerial photographs collected by the UAV. This process entailed a series of technical steps to ensure the accuracy and precision of the obtained 3D point cloud. First and foremost, the UAV's camera underwent a meticulous calibration procedure to ascertain its intrinsic parameters, including focal length and lens distortion coefficients. The subsequent phase involved the systematic acquisition of high-resolution aerial images during the UAV flight, thoroughly covering the targeted road segment within the Harran University Osmanbey campus from diverse angles and viewpoints. Key features, often referred to as keypoints, were then meticulously extracted from these images to facilitate the establishment of correspondences between overlapping images.

When coupled with the S*f*M technique, UAV-based imagery can be efficiently processed to derive valuable three-dimensional (3D) information [13]. S*f*M, a computer vision methodology, plays a pivotal role in this process by analyzing common features across a series of overlapping 2D images captured from different angles. By leveraging camera parameters such as focal length, distortion, camera position, and orientation, S*f*M calculates the 3D coordinates of these features, ultimately generating a point cloud [14]. This point cloud represents the spatial layout of the objects and terrain within the surveyed area in a highly detailed and accurate manner.

The extracted features from multiple images were matched to identify common points visible from various perspectives. With this correspondence in place, S*f*M algorithms accurately determined the positions and orientations of the UAV camera for each image, thus enabling the creation of a 3D point cloud through triangulation. Initially, a sparse point cloud was generated to provide a basic approximation of the scene's structure. However, this sparse cloud was further refined through bundle adjustment techniques, which minimized discrepancies between observed feature positions and their corresponding 3D positions in the point cloud.

Subsequently, the sparse point cloud was densified to create a detailed and comprehensive representation of the road surface. This densification process involved interpolating and adding additional 3D points to enhance the point cloud's richness. Finally, to ensure the alignment of the point cloud data with real-world geographic coordinates, georeferencing techniques were employed, culminating in a precisely calibrated and spatially referenced point cloud dataset. These technical steps collectively laid the groundwork for the subsequent road roughness analysis, empowering the study to draw meaningful insights from the UAV-derived point cloud data.

2.2. Roughness analysis

At this point, we have to remind that the roughness analysis was performed in Cloud Compare software. To initiate the roughness analysis, a crucial step involved the definition of a 'kernel' and its corresponding 'kernel size'. This 'kernel' represented a neighborhood radius around each point within the point cloud dataset. The 'kernel size' determined the spatial extent within which neighboring points were considered for roughness calculations. By strategically defining these parameters,

the study ensured that the analysis captured variations in road roughness across the entire dataset effectively [15].

The core metric for assessing road roughness was the distance between each point and the best fitting plane computed using its nearest neighbors within the designated 'kernel'. This distance, measured orthogonally to the plane, provided a quantitative measure of surface irregularities. The selection of this 'best fit plane' approach allowed for a robust evaluation of the road's topographical variations, ensuring that the analysis was sensitive to even subtle changes in surface height.

The roughness calculation further delved into the differences in elevation between each central point and the average height of its neighboring points. This 'height difference' parameter was computed along the specified 'vertical' orientation, enabling the study to capture vertical deviations in the road surface. The use of this parameter allowed for a multi-dimensional assessment of road roughness, considering both horizontal and vertical variations.

In scenarios where there were insufficient neighboring points to reliably compute a least-squares (LS) plane-typically fewer than three neighbors-the study systematically assigned an invalid scalar value (NaN) to those points. This precautionary measure ensured that roughness calculations were only performed on points with a sufficient neighborhood context, maintaining the integrity of the analysis.

3. Results and Discussion

Within the scope of the study, ground control points were established before flying with the UAV in the field. Then a photogrammetric flight plan was prepared. According to the plan, an altitude of 20 m was preferred for a road segment of approximately 185 m in length. No lower altitude was flown because it was considered a serious risk that trees and lighting lamps in the median could jeopardize the flight. 143 aerial images were obtained over the study area by using DJI Mavic 2 Pro. The overlap ratios were set to 80% in the flight plan. Thus, the maximum level of detail was wanted to be captured. The point cloud obtained as a result of the study contains more than 6 million points. All photogrammetric process were performed in Agisoft Metashape (Figure 1).

Figure 1. UAV flight lines and point cloud of the study area.

Within the scope of the study, it is necessary to decide on the kernel size, as stated in the method section, in order to determine the rough areas from the point cloud. The road roughness level varies depending on the selected kernel size. As seen in Figure 2, a defect that can be noticed visually and should be considered in terms of comfort and safety is not very rough in the small kernel size (10 cm in our study). However, as the kernel size increases, roughness or defects are detected.

Since the applied algorithm takes into account the height information of the points remaining in the kernel, examining the data set carefully and filtering outliers, if any, by pre-processing will yield more accurate results. In our case, the statistical outlier filter was performed. Apart from this, it would be rational to determine for what purpose the roughness analysis will be made.

The kernel size, also referred to as the neighborhood radius, is a critical parameter that significantly affects the calculation of road roughness from point cloud data. It essentially determines the scale at which roughness is assessed. Considering that the contact area of rubber-tired vehicles with the road surface typically falls within the range of 30 to 70 cm^2 [16], we selected specific kernel sizes for our study. To elaborate, we investigated three distinct kernel sizes: 30 cm, considered as *"smaller"*; 50 cm, denoted as *"moderate"*; and 75 cm, categorized as *"larger"*. The subsequent section delves into the manner in which road roughness reacts to variations in core size. The roughness result of 30 cm kernel size is given in Figure 3.

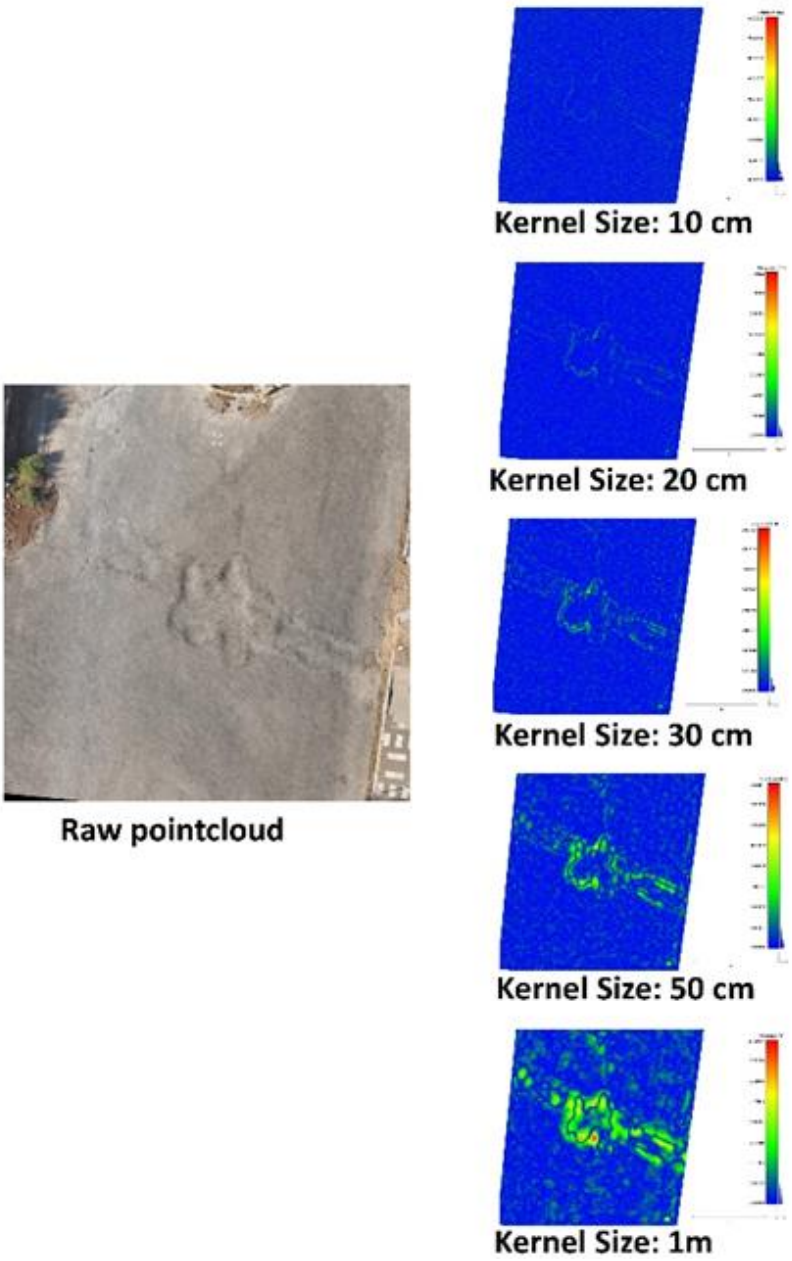

Figure 2. Roughness results of different kernel sizes.

Figure 3. Roughness result of 30 cm kernel size.

According to Figure 3, it is possible to say that smaller kernel sizes typically have a radius that covers only a limited area around each point in the point cloud. Moreover, with smaller kernel sizes, the analysis focuses on fine-scale variations in the road surface. This level of detail is particularly useful for identifying and quantifying small-scale irregularities, such as minor cracks, tiny potholes, or subtle surface texture variations. Smaller kernel sizes provide a highly detailed assessment of road roughness and are preferred when capturing fine-grained features is crucial.

The roughness result for a moderate kernel size (50 cm) is given in Figure 4.

As seen in Figure 4, the moderate kernel sizes strike a balance between capturing fine details and assessing broader trends on the road surface. This kernel sizes encompass a moderately sized area around each point, providing a more generalized view of roughness. It is possible to say that the analysis with moderate kernel sizes can effectively highlight medium-scale features like undulations, rutting, or larger cracks. Moderate kernel sizes are versatile and are often chosen when a comprehensive yet manageable assessment of road roughness is required.

The roughness result for a larger kernel size (75 cm) is given in Figure 5.

As shown in Figure 5, the larger kernel sizes involve a radius that covers a substantial area surrounding each point. With this larger kernel size, the analysis focuses on capturing the overall road condition, smoothing out localized variations. These kernel sizes are effective at assessing the road's macro-level characteristics, including large undulations, dips, or extensive surface defects. Larger kernel sizes are chosen when the primary interest is in understanding the general road roughness pattern and identifying major road surface issues.

In the end, the selection of a specific kernel size depends on the objectives of the road roughness analysis. Smaller kernel sizes are ideal for detailed inspections, moderate sizes offer a balanced view, and larger sizes provide a broader perspective of road conditions. Researchers and practitioners can tailor their choice based on the level of detail required and the specific characteristics of the road being evaluated.

Figure 4. Roughness result of 50 cm kernel.

Figure 5. Roughness result of 75 cm kernel.

4. Conclusion

In this study, we explored the potential of UAVs equipped with S*f*M-derived point clouds to revolutionize the assessment of road roughness. Road roughness is a crucial parameter affecting road safety, user comfort, vehicle operating costs, and infrastructure maintenance. Traditional methods of road roughness analysis, relying on manual inspections or image annotation, often suffer from limitations in data completeness, efficiency, and cost-effectiveness, especially for extensive road networks. Our investigation, conducted on a road segment within the Harran University Osmanbey campus, demonstrated the efficacy of UAV technology combined with S*f*M-derived point clouds as a robust and practical solution for road roughness assessment. By harnessing the advantages of UAVs, such as rapid data acquisition and high-resolution imagery, and employing S*f*M to generate detailed point clouds, we were able to provide a comprehensive analysis of road surface conditions.

Through a systematic examination of road roughness at varying kernel sizes, specifically 30 cm (*smaller*), 50 cm (*moderate*), and 75 cm (*larger*), we gained valuable insights into how different scales of analysis impact roughness measurements. This research not only contributes to the field of transportation infrastructure management but also underscores the significance of UAV technology in enhancing road safety, optimizing maintenance schedules, and minimizing operational costs.

Our findings suggest that UAV-derived point clouds offer a promising avenue for road roughness analysis, providing transportation authorities and road administrators with an efficient and cost-effective means of maintaining and enhancing road networks. By leveraging this technology, we can work towards the development of safer, more efficient, and economically sustainable road transportation systems.

As we move forward, further research and technological advancements in UAV-based road roughness assessment have the potential to revolutionize road management practices, ultimately leading to enhanced road quality and improved travel experiences for road users.

Author contributions

Nizar Polat: Conceptualization, Methodology, Software, Writing Reviewing and Editing **Şeyma Akça:** Data curation, Visualization, Investigation, Software, and Validation.

Conflicts of interest

The authors declare no conflicts of interest.

References

1. King, B. A. (2014). The effect of road roughness on traffic speed and road safety. Master's Thesis. University of Southern Queensland.
2. Bester, C. J. (2003). The effect of road roughness on safety. 82nd Annual Meeting of the Transportation Research Board, Washington, DC.
3. Davies, R. B., Cenek, P. D., & Henderson, R. J. (2005). The effect of skid resistance and texture on crash risk. Proceedings Surface Friction Roads and Runways, Christchurch, 1-4.
4. Wu, J., & Song, X. (2020). Review on smart highways critical technology. Journal of Shandong University (Engineering Science), 50, 52-69
5. Ihs, A. (2005). The influence of road surface condition on traffic safety and ride comfort. 6th International Conference on Managing Pavements 19–24 October 2004. Brisbane Convention & Exhibition Centre, Queensland Australia, 11-21.
6. Kumar, P., Lewis, P., McElhinney, C. P., & Rahman, A. A. (2015). An algorithm for automated estimation of road roughness from mobile laser scanning data. The Photogrammetric Record, 30(149), 30-45. https://doi.org/10.1111/phor.12090
7. Hesami, R., & McManus, K. J. (2009). Signal processing approach to road roughness analysis and measurement. TENCON 2009-2009 IEEE Region 10 Conference, 1-6. https://doi.org/10.1109/TENCON.2009.5396085
8. Zhou, Y., Guo, X., Hou, F., & Wu, J. (2022). Review of intelligent road defects detection technology. Sustainability, 14(10), 6306. https://doi.org/10.3390/su14106306
9. Yiğit, A. Y., & Uysal, M. (2021). Yüksek çözünürlüklü insansız hava aracı (İHA) görüntülerinden karayolların tespiti. Bitlis Eren Üniversitesi Fen Bilimleri Dergisi, 10(3), 1040-1054. https://doi.org/10.17798/bitlisfen.900817
10. Uysal, M., Toprak, A. S., & Polat, N. (2015). DEM generation with UAV Photogrammetry and accuracy analysis in Sahitler Hill. Measurement, 73, 539-543. https://doi.org/10.1016/j.measurement.2015.06.010
11. Akca, S., & Polat, N. (2022). Semantic segmentation and quantification of trees in an orchard using UAV orthophoto. Earth Science Informatics, 15(4), 2265-2274. https://doi.org/10.1007/s12145-022-00871-y
12. Smith, A., & Sarlo, R. (2022). Automated extraction of structural beam lines and connections from point clouds of steel buildings. Computer-Aided Civil and Infrastructure Engineering, 37(1), 110-125. https://doi.org/10.1111/mice.12699
13. Snavely, N., Seitz, S. M., & Szeliski, R. (2008). Modeling the world from internet photo collections. International journal of computer vision, 80, 189-210. https://doi.org/10.1007/s11263-007-0107-3
14. Toprak, A. S., Polat, N., & Uysal, M. (2019). 3D modeling of lion tombstones with UAV photogrammetry: a case study in ancient Phrygia

(Turkey). Archaeological and Anthropological Sciences, 11(5), 1973-1976. https://doi.org/10.1007/s12520-018-0649-z
15. https://www.cloudcompare.org/doc/wiki/index.php/Roughness
16. Gillespie, T. D. (2021). Fundamentals of vehicle dynamics. SAE international.

Mersin Photogrammetry Journal
https://dergipark.org.tr/en/pub/mephoj
e-ISSN 2687-654X

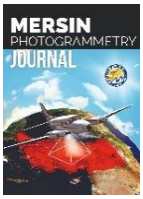

Investigation of geometric object and indoor mapping capacity of Apple iPhone 12 Pro LiDAR

Mehmet Akif Günen [*1], **İlker Erkan**[2], **Şener Aliyazıcıoğlu** [2], **Cavit Kumaş**[2]

[1]*Gümüşhane University, Department of Geomatics Engineering, Türkiye*
[2]*Gümüşhane University, Department of Mining Engineering, Türkiye*

Keywords
iPhone 12 Pro
Point Cloud
LiDAR
Mapping

Research Article
DOI: 10.53093/mephoj.1354998

Received:04.09.2023
Revised: 04.10.2023
Accepted:09.10.2023
Published:17.10.2023

Abstract

LiDAR (light detection and ranging) sensors use laser beams to calculate distances in the surroundings. These sensors can be applied to a wide range of tasks, and they are frequently helpful in tasks like building 3D maps, navigating airplanes, robots, conducting mining operations, and automated driving. High-resolution distance measurements are taken by LiDAR sensors, but they also gather environmental data. This information aids in locating, identifying, and quantifying things and their surroundings. The iPhone 12 Pro, which Apple released in 2020, was evaluated for accuracy with various geometric shapes and its capacity to recognize indoor environments. Free of charge 3D Scanner and the Clirio Scan application were employed in this situation. However, it was found that the root mean square error and mean error in indoor mapping were ±1.41 cm and -0.56 cm in 3D Scanner and ±3.94 cm and -0.60 cm in the Clirio Scan application, respectively, despite the findings obtained showing low accuracy in scanning small geometric objects due to the scanning difficulty. Clirio does not reject the null hypothesis in the t-test that was conducted. The accuracy of the LiDAR sensor in indoor mapping has been shown to be more promising than that of small items. In order to evaluate the reliability and reusability of the indoor mapping application according to reference measurements, intraclass correlation test was performed and the results were determined to be reliable.

1. Introduction

Terrestrial laser scanning, aerial laser scanning, structured light, structure-from-motion, and multi-view stereo are photogrammetric data acquisition approaches that will help various fields [1-4]. Rapid breakthroughs in image and signal processing techniques, as well as technological microchip advancements, have enabled the production of low-cost and minimum sensors. These methods have advantages and weaknesses, and new generation technologies are expected to make data collecting faster and more flexible. It is also critical to conduct accurate research on newly created technology. Close range remote sensing technologies such as Light Detection and Ranging (LiDAR) are creating greater opportunities than ever for architectural surveying [5], forensic [6], restoration [7], archaeological documentation [8], underground mining operations [9], mining and post mining operations [10-12], game character modeling, analysis and interpretation [13]. LiDAR technology is now widely employed in geomatic applications due to its speed, practicability, and precision. Data capture for LiDAR typically uses the time-of-flight (ToF) and phase difference methods. This technology, particularly when combined with the Inertial Measurement Units (IMU) system, has cleared the path for its application in a variety of disciplines [14]. This allows for the rapid creation of 3D point clouds and models. Involving a larger number of non-expert users in the process assures that the augmented reality application and documentation process of the created models is widely disseminated throughout the community, highlighting the need of investigating LiDAR/photogrammetric systems. Development of micro-dimensions of sensors and electro-mechanical components lead to support these systems with high computational power. This digital advancement has been aided by different technology advances, resulting in a broader use for the 3D documentation process [14-18].

Although LiDAR technology has long been utilized in terrestrial laser scanning, it is not always practicable to retrieve, preserve, and transport these instruments, and operating them requires expertise. The widespread use of electronics products has reduced the cost to the

* **Corresponding Author**
*(akif@erciyes.edu.tr) ORCID ID 0000-0001-5164-375X
(ilkererkan@gumushane.edu.tr) ORCID ID 0000-0001-7326-6297
(s.aliyazicioglu@gumushane.edu.tr) ORCID ID 0000-0002-5177-8221
(ckumas@gumushane.edu.tr) ORCID ID 0000-0002-4221-3034

Cite this article
Günen, M. A., Erkan, İ., Aliyazıcıoğlu, Ş., & Kumaş, C. (2023). Investigation of geometric object and indoor mapping capacity of Apple iPhone 12 Pro LiDAR. Mersin Photogrammetry Journal, 5(2), 82-89

consumer overall and increased the speed of portable devices like smartphones and tablets, leading to continued advancements in computing power, overall performance, advancements in computer vision algorithms, and general data processing optimizations. In order for the end customer to be able to reverse engineer the product design, the manufacturer competes by delivering high quality products customized to meet their needs. The infrared and RGB sensor of the RGB-D sensors, for instance, are used in a variety of applications, including indoor mapping, 3D mapping and localization, path planning, body tracking, health applications, and Human Pose, despite the fact that they were originally introduced to improve player performance and the sense of realism [1, 19, 20]. The path for the digitization of actual items has been prepared thanks to the LiDAR and TrueDepth technologies integrated into Apple's new devices released in 2020. Being less dependent on the energy source (like heavy batteries) and easily handling related to LiDAR, it is apparent that these devices will be mentioned more for scientific purposes in the upcoming years. Although Apple's LiDAR was mainly created for augmented reality applications, it is important to look into its use in other reverse engineering applications. Using the ToF concept, Apple's LiDAR sensor produces a modulated light signal and detects the time difference with the returning wave, in other word the amount of time it takes for the signal to return in order to measure an object [21-23].

This study was conducted to determine the potential use of LiDAR in the iPhone 12 Pro series as a 3D scanner. The scanning ability of small geometric objects as well as the possibilities for indoor scanning were examined in this context. The measured distances from point clouds obtained with "3D Scanner App" and "Clirio Scan" applications on the Apple Store were compared to the actual value obtained in this scope, and the utility of the LiDAR sensor in geomatic applications was explored using reliability tests.

2. Material and Method

Two different applications from Apple Store were used to obtain point clouds of small items with distinct geometric properties and indoor point clouds encompassing bigger regions with a LiDAR sensor. The actual measurements of the targeted objects were measured five times with a steel tape measure and averaged. Figure 1 presents the sensors of the iPhone 12 Pro used in the fulfillment of this study. The general specifications of the iPhone 12 Pro are as follows: Wide camera: 12 MP, f/1.6, 26 mm, telephoto camera :12 MP, f/2.0, 52 mm and ultrawide camera:12 MP, f/2.4, 13 mm, 120˚ [24]. It is stated that its ToF LiDAR scans a maximum range of 5 m. Although the main purpose of iPhone LiDAR is to develop digital photo capture, especially in low light focusing, most of software (i.e., Polycam, Heges, EveryPoint, RTAB-MAP, Scaniverse, Clirio Scan, 3D Scanner App, and Pix4DCatch) produces textured 3D scans with the help of Apple ARkit [25]. In addition, since the TrueDepth sensor of iPhone 12 Pro (Figure 1) detects in the infrared region, which located on the front of the phone, it generates data in dark environments, but it is not the subject of this study. Because of their quick guided acquisition, simple user interface, and reasonably short processing periods that allowed results, the 3D Scanner App and Clirio Scan applications were selected for this study. Although the software works with GPS/GNSS incorporated in outdoor field work, it is turned off in inside work since GPS impacts the accuracy of the data collected. Small item photogrammetric digitization presents a significant challenge in general. Therefore, sphere and cylinder-shaped geometric objects were scanned. Interior mapping of the Gümüşhane University Engineering Faculty (Gümüşhane, Türkiye) corridor was made after examining Apple's new LiDAR, in order to evaluate the system's effectiveness in a bigger region.

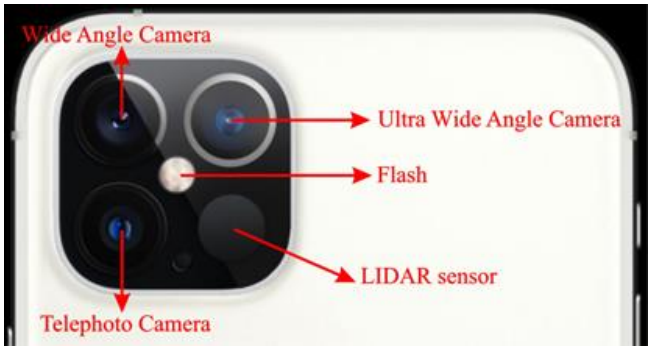

Figure 1. Sensors of iPhone 12 Pro.

First, point clouds were produced by scanning the spherical and cylindrical objects shown in Figure 2-3. The spherical object is a desk-mounted educational model of the world globe. The cylindrical item is a laboratory-scale steel grinding tube (Ball Mill Chamber/Grinding Chamber) used in mining engineering laboratory tests. The outside of a model of the world globe was used for spherical shapes, while the interior of the grinding tube (Ball Mill Chamber/Grinding Chamber) was used for cylindric shapes. The dimensions of the objects are specified at Table 1. When the figures are examined, it is seen that the applications capture different number of point data even though data is taken from different tracking array at the same time. After the point cloud is produced, its transformations to the mesh model are provided. Then, the data was filtered using Taubin's algorithm [26]. The Taubin filter was used because it is a successful method that provides a type of low-pass and high-pass filtering on 3D point clouds or surfaces. By performing the filtering process, noise removal is ensured from the data, so that the inappropriate fit of the models to be fitted to small objects and the measurement process from noisy points in the interior are prevented. The model parameters obtained by fitting the best model to the geometric features were compared with their actual measurements. For indoor mapping, real measurements of 20 different objects were taken from the created point cloud. Matlab 2021a software was used for model fit to geometric shapes, MeshLab for point cloud filtering and measurements of object edges and SPSS 18 software for statistical research. All applications are using MSI delta 15 laptop with AMD Ryzen 9 9500 HX processor, RX6700 graphics card and 32 GB RAM.

(a) (b) (c)

Figure 2. Sphere object a) RGB image, and point cloud of b) Clirio Scan, c) 3D Scanner App applications.

(a) (b) (c)

Figure 3. Cylinder object a) RGB image, and point cloud of b) Clirio Scan, c) 3D Scanner application.

3. Results and Discussion

In the application, firstly, objects with spherical and cylindrical shapes were scanned using Clirio Scan and 3D Scanner App applications. Examining the objects presented in point clouds Figure 2 and Figure 3, it is seen that the objects scanned with Clirio Scan have a higher number of points but contain more noise. The best fit model results fitted to the obtained point clouds are presented in Table 1 and their visual representations from different perspectives are presented in Figures 4-5.

The actual area of the modeled cylinder is 2,401.31 cm^2 and its volume is 1,810.12 cm^3. The area calculated with Clirio Scan is 2,416.25 cm^2 and the volume is 1,838.4 cm^3, and the area calculated with the 3D Scanner is 2,382.56 cm^2 and the volume is 1,843.79 cm^3. From this, it can be deduced that both Clirio Scan and 3D Scanner App detects the area with a difference of under 1% while Clirio Scan gives the nearest. When it comes to the volume of the cylinder the difference is increased and both applications detect the volume of the cylinder with a difference of between 1.5-1.9% while Clirio Scan is still gives the nearest.

The actual volume of the modeled sphere is 13,884.22 cm^3 and its surface area is 2,793.61 cm^2. The volume calculated with Clirio Scan is 10,374.85 cm^3 surface area is 2,300.41 cm^2, the volume calculated with 3D Scanner App is 11,273.79 cm^3 surface area is 2,431.44 cm^2. It can be seen once more that the point cloud created by the 3D Scanner App provides values that are closer.

Table 1. Best fit model and actual measurement results.

Application Name	Model	
	Cylinder Actual Height: 29.7 cm Actual Radius: 9.7 cm	Sphere Actual Radius:14.91
Clirio Scan	Height: 30.51 cm Radius: 9.59 cm	Radius:13.53
3D Scanner App	Height:31.69 cm Radius:9.26 cm	Radius:13.91

The procedure of indoor mapping was carried out after the identification of small geometric objects. Figure 6 shows the locations of the assets measured in the scanned corridor, and Table 2 lists the numerical results of the associated measurements. Measurements were taken in this context for the nameplate, the corridor width, the corridor length, the column length, the poster length, and different tables.

Figure 7 shows the information on the differences between the lengths estimated with MeshLab software over the point clouds created by the applications and the steel tape measure accepted as the actual value. Since the

scanning is happening quickly, it can be claimed that the greatest size disparities between the two applications typically occur in the direction of camera movement. Because moving quickly can lead to the data being misalignment.

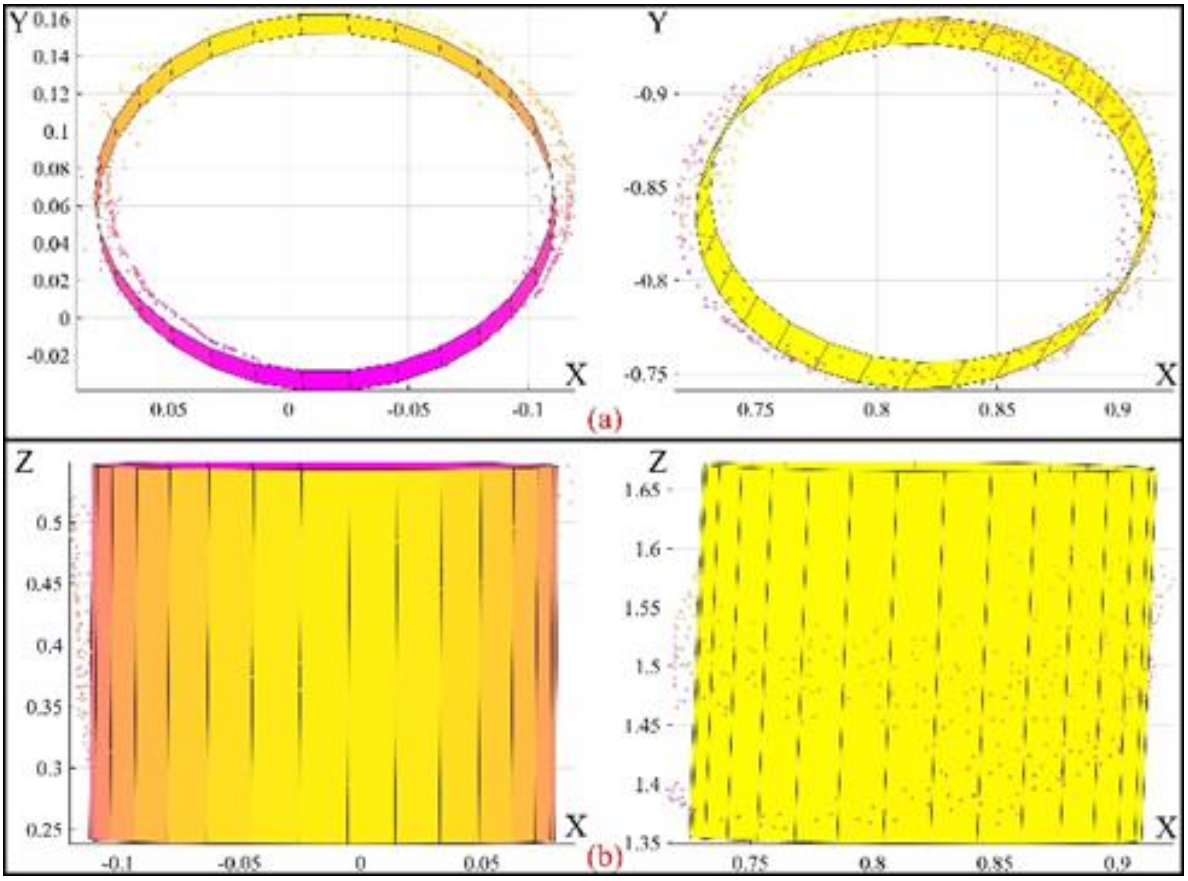

Figure 4. Cylinder fitted to a) 3d Scanner App data b) Clirio Scan data from different viewpoints.

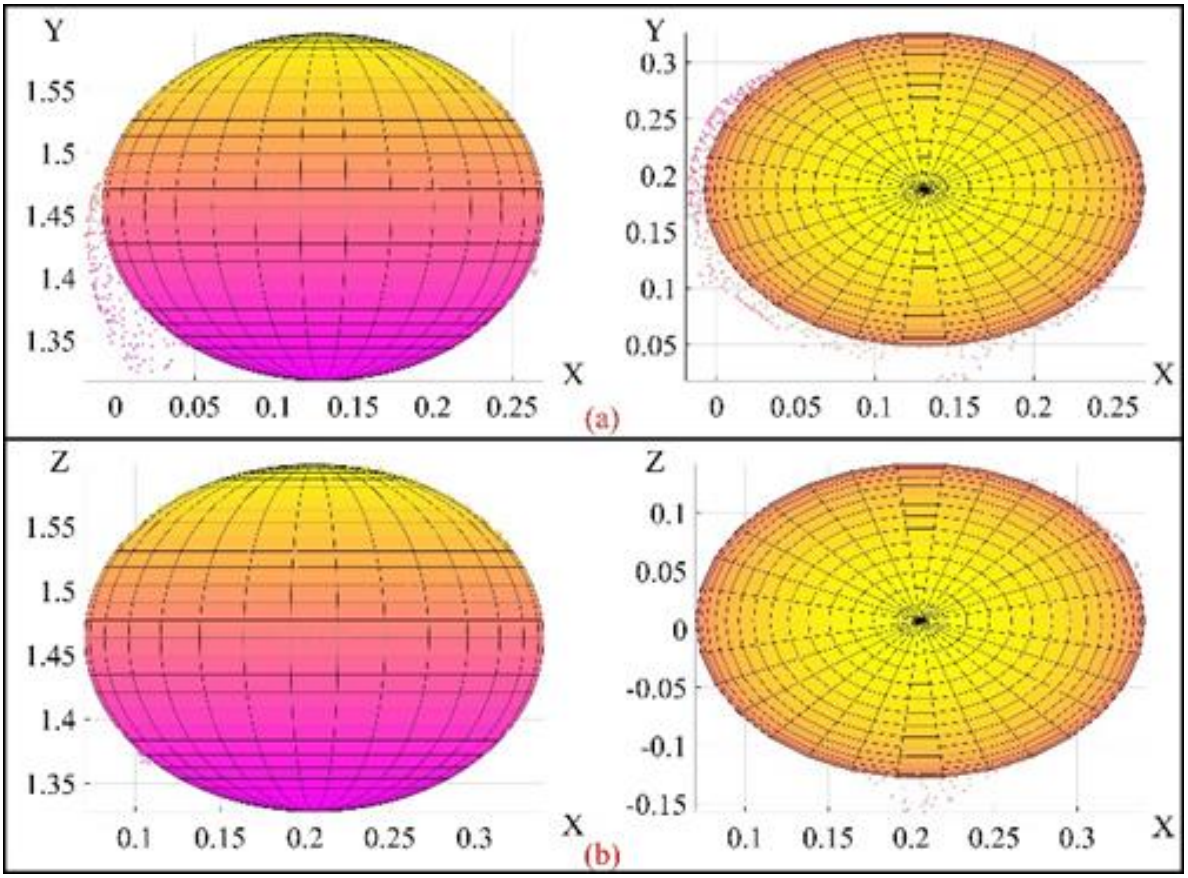

Figure 5. Sphere fitted to a) 3D Scanner App data b) Clirio Scan data from different viewpoints.

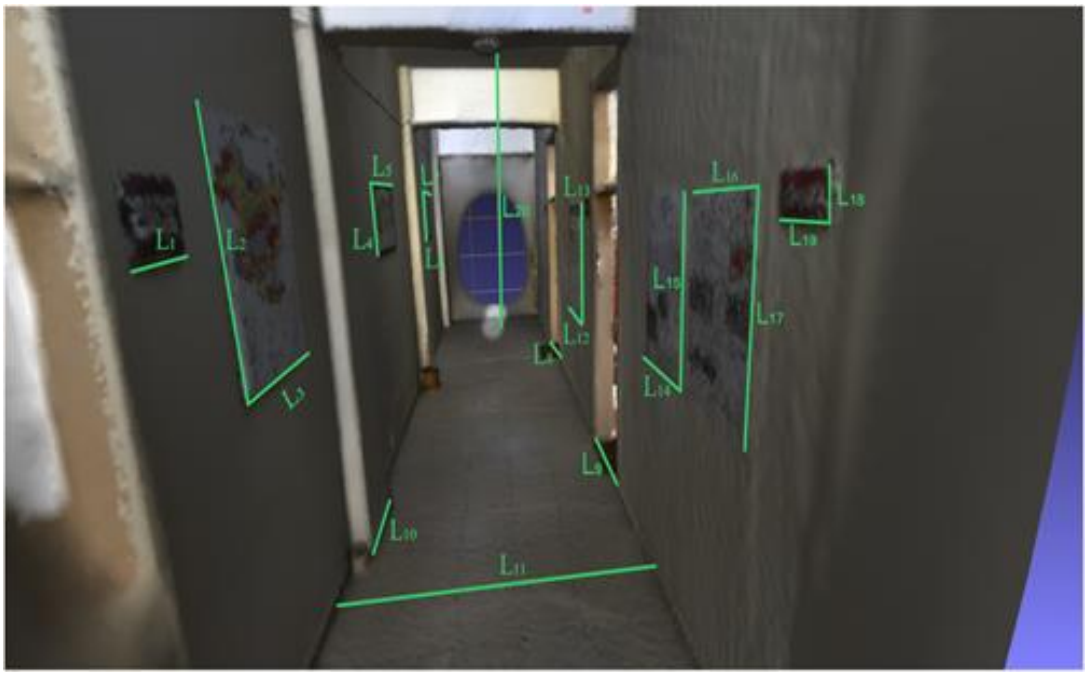

Figure 6. Display of the measured objects on the mesh model.

Table 2. Actual and application-generated point cloud measurements.

#Lenghts	Actual value (cm)	3D Scanner value (cm)	Clirio Scan value (cm)
L_1	25.3	25.43	25.67
L_2	95.4	97.21	93.62
L_3	66.0	66.02	66.78
L_4	52.5	52.35	52.89
L_5	92.5	93.89	95.38
L_6	62.4	61.01	62.65
L_7	84.3	84.59	85.47
L_8	80.6	81.56	77.85
L_9	80.7	81.05	82.60
L_{10}	56.3	59.82	59.66
L_{11}	217.5	217.86	217.76
L_{12}	91.0	90.65	94.79
L_{13}	121.5	122.43	121.10
L_{14}	59.5	60.66	64.65
L_{15}	84.7	86.78	83.31
L_{16}	59.5	60.38	59.30
L_{17}	84.7	85.17	83.28
L_{18}	12.0	12.24	12.74
L_{19}	25.3	24.59	24.40
L_{20}	330.02	329.31	329.73

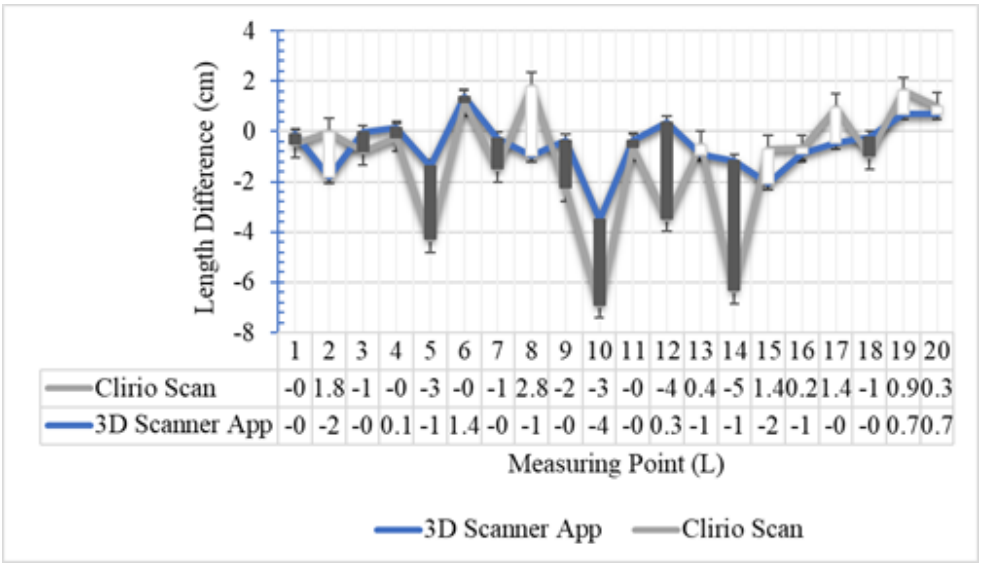

Figure 7. Differences in length between estimated and actual values.

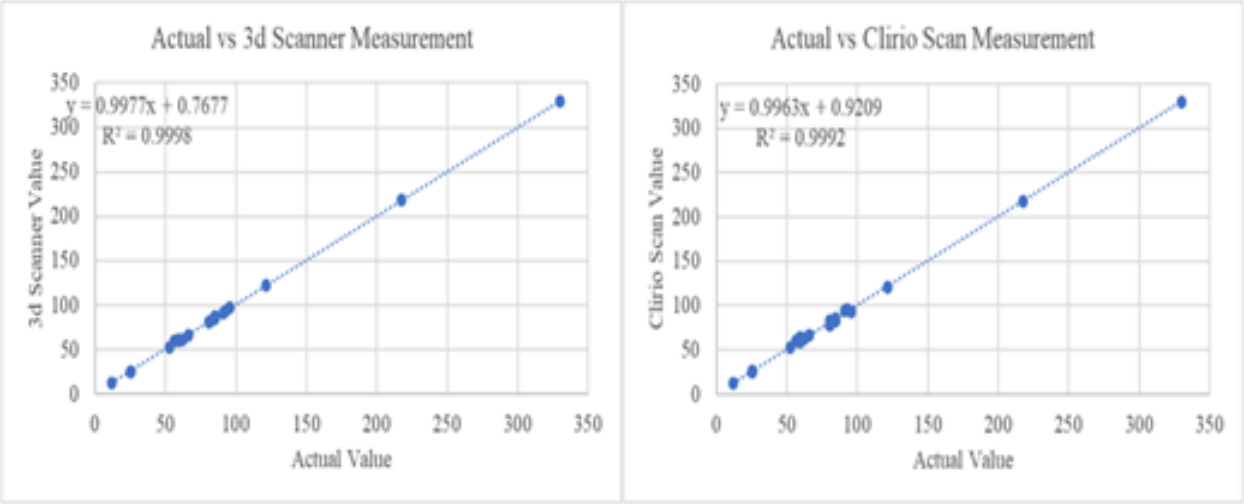

Figure 8. Linear trend model of actual measurements vs 3D Scanner App, and actual measurements vs Clirio Scan application.

When the information is examined, it is seen that the biggest difference occurs in the L_{14} length in the point cloud produced by the Clirio Scan software, with 5.15 cm, and the lowest difference occurs in the L_1 length by the 3D Scanner App application. Linear trend model of actual measurements vs Clirio Scan and actual measurements vs 3D Scanner App application values are given in Figure 8.

In statistical analysis processes, regression analysis is one of the most popular techniques. There are multiple dependent variables that have an impact on the dependent variable. The established model's performance was assessed using the R^2. The lower the total square of the residuals, in R^2, which measures the regression's goodness of fit, the better the fit. R^2 is always between 0 and 1, and the closer it is to 1 in general, the more variability the model can explain. The data obtained from the relevant applications are related to the actual values since the R^2 value obtained from the applications in the performed study is greater than 99%.

To determine the data's statistical significance for indoor mapping, the paired sample t-test was used. The pairwise difference between actual data and software-generated data vectors is compared to test the null hypothesis that it has a mean of zero. The null hypothesis is not rejected by the data from Clirio Scan (p=0.198), but it is by the results from the 3D Scanner App (p=0.034). Small values of p raise questions about the reliability of the null hypothesis since they increase the probability of observing a test statistic. Apple only describes the 5 m range of the LiDAR sensor used in its products; no other feature descriptions are provided. This restricts the application's use to regions larger than 5 m^2 and to big areas. Application has a limitation because of this. Though it has a restricted capacity, the program strives to provide the best performance it can and gets better with each passing day. It receives upgrades almost weekly. The major issue with the software is misalignment because it doesn't provide accurate trajectory tracking and doesn't react quickly. A different issue from these is the development of data gaps as a result of starting and continuing from various starting locations. It takes knowledge to collect data because of this. Although these black box applications provide filtered data while exporting the data, the noise levels of the data obtained by using the Taubin's filter are further lowered to fit the most suitable geometric models and make the length measurement more precise.

The intraclass correlation coefficient (widely used for reliability index), which has a value between 0 and 1, is a descriptive statistic that can be employed when quantitative measurements are taken on units grouped in groups. It expresses correlations inside a data class rather than correlations between two independent data classes.

4. Conclusion

The accuracy of the Apple iPhone 12 Pro's LiDAR scanner was investigated in this study. Real measurements were compared with scans of various geometric shapes and interior mapping. The scanning of small geometric objects is fairly challenging, but the results are very encouraging as a result of the findings. Especially on cylinder shaped model Clirio Scan gives the closest values while 3D Scanner App is a little less accurate. The values detected for spherical model showed that the 3D Scanner App detected the model relatively accurate. Since the detected values for both applications are in range of 13-25% difference 3D Scanner App detected the sphere more accurate than Clirio Scan. In terms of indoor mapping, it is highly effective. The sensor's limited capacity to scan over a short distance, however, is a significant drawback. The accuracy of the point cloud the software produces is crucial, according to the statistical tests done. It can be said that 3D Scanner App application produces better results than Clirio Scan. In future studies, accuracy analysis will be carried out by including different software and working on larger areas.

Author contributions

Mehmet Akif Günen: Writing, Investigation, Implementation, **İlker Erkan:** Conceptualization, Validation, Writing, **Şener Aliyazıcıoğlu:** Reviewing, Ideating, Writing, **Cavit Kumaş** Ideating, Language checking, Editing the manuscript

Conflicts of interest

The authors declare no conflicts of interest.

References

1. Günen, M. A., & Beşdok, E. (2021). Comparison of point cloud filtering methods with data acquired by photogrammetric method and RGB-D sensors. International Journal of Engineering and Geosciences, 6(3), 125-135. https://doi.org/10.26833/ijeg.731129
2. Guo, B., Zhang, Y., Gao, J., Li, C., & Hu, Y. (2022, September). SGLBP: Subgraph-based local binary patterns for feature extraction on point clouds. Computer Graphics Forum, 41(6), 51-66. https://doi.org/10.1111/cgf.14500
3. Seyfeli, S., & OK, A. (2022). Classification of mobile laser scanning data with geometric features and cylindrical neighborhood. Baltic Journal of Modern Computing, 10(2), 209-223. https://doi.org/10.22364/bjmc.2022.10.2.08
4. Silva, M. F., Green, A., Morales, J., Meyerhofer, P., Yang, Y., Figueiredo, E., ... & Mascareñas, D. (2022). 3D structural vibration identification from dynamic point clouds. Mechanical Systems and Signal Processing, 166, 108352. https://doi.org/10.1016/j.ymssp.2021.108352
5. Nex, F., & Rinaudo, F. (2009). New integration approach of photogrammetric and LIDAR techniques for architectural surveys. The International Archives of the Photogrammetry, Remote Sensing and Spatial Information Sciences, 38(3), 12-17
6. Bahirat, K., & Prabhakaran, B. (2017). A study on lidar data forensics. IEEE International Conference on Multimedia and Expo (ICME), 679-684. https://doi.org/10.1109/ICME.2017.8019395
7. Almeida, D. R. A. D., Stark, S. C., Chazdon, R., Nelson, B. W., César, R. G., Meli, P., ... & Brancalion, P. H. S. (2019). The effectiveness of lidar remote sensing for monitoring forest cover attributes and landscape restoration. Forest Ecology and Management, 438, 34-43. https://doi.org/10.1016/j.foreco.2019.02.002
8. Lozić, E., & Štular, B. (2021). Documentation of archaeology-specific workflow for airborne LiDAR data processing. Geosciences, 11(1), 26. https://doi.org/10.3390/geosciences11010026
9. Leottau, D. L., Vallejos, P., & del Solar, J. R. (2018). LIDAR-based displacement estimation in mining applications. 6th International Congress on Automation in Mining. 1-9
10. Froese, C. R., & Mei, S. (2008). Mapping and monitoring coal mine subsidence using LiDAR and InSAR. GeoEdmonton, 8, 1127-1133.
11. Kekeç, B., Bilim, N., Karakaya, E., & Ghiloufi, D. (2021). Applications of terrestrial laser scanning (TLS) in mining: A review. Türkiye Lidar Dergisi, 3(1), 31-38. https://doi.org/10.51946/melid.927270
12. Murray, X., Apan, A., Deo, R., & Maraseni, T. (2022). Rapid assessment of mine rehabilitation areas with airborne LiDAR and deep learning: bauxite strip mining in Queensland, Australia. Geocarto International, 37(26), 11223-11252. https://doi.org/10.1080/10106049.2022.2048902
13. Günen, M. A., Çoruh, L., & Beşdok, E. (2017). Oyun dünyasında model ve doku üretiminde fotogrametri kullanımı. Geomatik, 2(2), 86-93. https://doi.org/10.29128/geomatik.318319
14. Horaud, R., Hansard, M., Evangelidis, G., & Ménier, C. (2016). An overview of depth cameras and range scanners based on time-of-flight technologies. Machine vision and applications, 27(7), 1005-1020. https://doi.org/10.1007/s00138-016-0784-4
15. Zhang, P., He, H., Wang, Y., Liu, Y., Lin, H., Guo, L., & Yang, W. (2022). 3D urban buildings extraction based on airborne lidar and photogrammetric point cloud fusion according to U-Net deep learning model segmentation. IEEE Access, 10, 20889-20897. https://doi.org/10.1109/ACCESS.2022.3152744
16. Zeybek, M., & Ediz, D. (2022). Detection of road distress with mobile phone LiDAR sensors. Advanced Lidar, 2(2), 48-53.
17. Karkinli, A. E. (2023). Detection of object boundary from point cloud by using multi-population based differential evolution algorithm. Neural Computing and Applications, 35(7), 5193-5206. https://doi.org/10.1007/s00521-022-07969-w
18. Aliyazıcıoğlu, Ş., Öztürk, K. F., & Günen, M. A. (2023). Analysis of Gümüşhane-Trabzon highway slope static and dynamic behavior using point cloud data. Advanced Lidar, 3(1), 70-75.
19. Günen, M. A., Kesikoğlu, A., Karkinli, A. E., & Beşdok, E. (2017). RGB-D sensörler ile iç mekan haritalaması. International Artificial Intelligence and Data Processing Symposium (IDAP), 1-6. https://doi.org/10.1109/IDAP.2017.8090220
20. Kadkhodamohammadi, A., Gangi, A., de Mathelin, M., & Padoy, N. (2017). A multi-view RGB-D approach for human pose estimation in operating rooms. IEEE winter conference on applications of computer vision (WACV), 363-372. https://doi.org/10.1109/WACV.2017.47
21. Vogt, M., Rips, A., & Emmelmann, C. (2021). Comparison of iPad Pro®'s LiDAR and TrueDepth capabilities with an industrial 3D scanning solution. Technologies, 9(2), 25. https://doi.org/10.3390/technologies9020025
22. Teppati Losè, L., Spreafico, A., Chiabrando, F., & Giulio Tonolo, F. (2022). Apple LiDAR Sensor for 3D Surveying: Tests and Results in the Cultural Heritage Domain. Remote Sensing, 14(17), 4157. https://doi.org/10.3390/rs14174157
23. Kuçak, R. A., Erol, S., & Alkan, R. M. (2023). iPad Pro LiDAR sensörünün profesyonel bir yersel lazer tarayıcı ile karşılaştırmalı performans analizi. Geomatik, 8(1), 35-41.

https://doi.org/10.29128/geomatik.1105048
24. https://support.apple.com/kb/SP831?locale=en_US
25. https://developer.apple.com/augmented-reality/arkit/
26. Taubin, G. (1995). A signal processing approach to fair surface design. in Proceedings of the 22nd annual conference on Computer graphics and interactive techniques. 351-358